

Submitted to *The Astrophysical Journal*, December 1996

## Inferring the Spatial and Energy Distribution of Gamma Ray Burst Sources. II. Isotropic Models

Thomas J. Loredo and Ira M. Wasserman

Center for Radiophysics and Space Research, Cornell University, Ithaca, NY 14853-6801

### ABSTRACT

We use Bayesian methods to analyze the distribution of gamma ray burst intensities reported in the *Third BATSE Catalog* (3B catalog) of gamma ray bursts, presuming the distribution of burst sources (“bursters”) is isotropic. We study both phenomenological and cosmological source distribution models, using Bayes’s theorem both to infer unknown parameters in the models, and to compare rival models. We analyze the distribution of the time-averaged peak photon number flux,  $\Phi$ , measured on both 64 ms and 1024 ms time scales, performing the analysis of data based on each time scale independently. Several of our findings differ from those of previous analyses that modeled burst detection less completely. In particular, we find that the width of the intrinsic luminosity function for bursters is unconstrained, and the luminosity function of the actually observed bursts can be extremely broad, in contrast to the findings of all previous studies. Useful constraints probably require observation of bursts significantly fainter than those visible to BATSE. We also find that the 3B peak flux data do not usefully constrain the redshifts of burst sources; useful constraints require the analysis of data beyond that in the 3B catalog (such as burst time histories), or data from brighter bursts than have been seen by BATSE (such as those observed by the *Pioneer Venus Orbiter*). In addition, we find that an accurate understanding of the peak flux distributions reported in the 3B almost certainly requires consideration of data on the temporal and spectral properties of bursts beyond that reported in the 3B catalog, and more sophisticated modeling than has so far been attempted.

We first analyze purely phenomenological power law and broken power law models for the distribution of observed peak fluxes. We find that the 64 ms data is adequately fit by a single power law, but that the 1024 ms data significantly favor models with a sharp, steep break near the highest observed fluxes. At fluxes below the break, the distribution of 1024 ms fluxes is flatter than that of 64 ms fluxes. Neither data set is consistent with the power law distribution expected from a homogeneous, Euclidean distribution of sources. Next we analyze three simple cosmological models for burst sources: standard candles with constant burst rate per comoving volume; a distribution of standard candle sources with comoving burst rate proportional to a power law in  $(1+z)$ , and a bounded power-law burster luminosity function with constant comoving

burst rate but variable power-law index and luminosity bounds. We find that the 3B data can usefully constrain the luminosity of a standard candle cosmological population of bursts if there is no density evolution. But the 3B data allow strong density evolution and arbitrarily broad luminosity functions; consequently, they do not usefully constrain the redshifts or luminosities of cosmological burst sources. We elucidate the properties of the models responsible for these results.

For sufficiently flexible models, the inferred values for parameters describing the shapes of the distributions of 64 ms and 1024 ms peak fluxes formally differ at the 68%–95% level. Because the measurements on these two timescales are not independent, it is difficult to ascertain the true significance of this discrepancy; since many bursts are common to both data sets, it is likely its significance is larger than these formal values indicate. In addition, the inferred amplitude (in bursts per year) of the distribution of 64 ms peak fluxes is about twice that of 1024 ms peak fluxes. These results strongly suggest that a complete understanding of the measured peak flux distributions requires simultaneous modeling and analysis of temporal properties of bursts. We study models that attempt to reconcile the two data sets by accounting for “peak dilution,” the underestimation of the peak intensity that results from using data accumulated over a timescale exceeding the peak duration. A phenomenological model strongly correlating peak duration with peak flux is moderately successful at reconciling the data. A model that correlates peak duration with peak flux due to cosmological time dilation and relativistic beaming is less successful, but remains of interest in that it is a simple physical model illustrating how one can jointly model and analyze temporal and spectral properties of bursts with peak flux data. A more rigorous accounting for the differences between the 64 ms and 1024 ms data requires analysis of temporal and spectral information about bursts beyond that available in the 3B catalog.

*Subject headings:* Gamma rays: bursts — Methods: data analysis — Methods: statistical

## 1. Introduction

In the absence of direct measurement of the distances to burst sources (“bursters”), or association of bursts with well-localized counterparts, we must infer the spatial and energy distribution of bursters from the observed distribution of burst strengths and directions. The complexity of the burst data makes this task considerably more difficult than it might at first appear because we must account for several subtle biases and selection effects. So far, analyses of burst data have relied on largely ad hoc choices of statistics designed to circumvent some of these effects. But differing choices of statistic or analysis method by different investigators have led to

some controversy over the implications of the burst data.

Of particular relevance to this work are the varying conclusions of numerous previous studies of isotropic models for the burst source distribution. On a purely phenomenological level, investigators differ over whether the logarithmic slope of the distribution of burst intensities exhibits a significant change in slope (cf. Loredo and Wasserman 1993; Wijers and Lubin 1993; Petrosian, Azzam, and Efron 1994). In the context of cosmological models, investigators have reached a variety of inconsistent conclusions about possible characteristics of the burst source distribution, including the value and uncertainty for the luminosity of standard candle sources (cf. Dermer 1992; Loredo and Wasserman 1993), and the ability of the data to constrain the width of the luminosity function of bursters (cf. Loredo and Wasserman 1993; Horack, Emslie, and Meegan 1994; and Cohen and Piran 1995) or the redshift of the faintest bursters (cf. Loredo and Wasserman 1993; Emslie and Horack 1994; Cohen and Piran 1995). These differences result largely from methodological differences among the published studies. Without a vastly larger dataset, only careful attention to methodological issues can identify the correct inferences.

In the first paper of this series (Loredo and Wasserman 1995; hereafter LW95), we described the Bayesian methodology for inferring the spatial and energy distribution of burst sources. Instead of constructing a customized statistic in an attempt to circumvent the various biases and selection effects that might enter inferences, we start from simple models (based on the Poisson distribution) for burst occurrence and detection, and directly calculate the probability for the observed data: the likelihood function. The likelihood function describes how well a model can account for the *joint differential distribution* of observed burst strengths and directions, and accounts for biases and selection effects by construction, rather than trying to circumvent them by a clever choice of statistic. Indeed, from the Bayesian point of view, there is no freedom of choice regarding what statistic to use and how to use it; the data enter Bayes's theorem in the likelihood function, and the rules of probability theory dictate both how to calculate the likelihood function and how to manipulate it to make inferences. This methodology offers several advantages over rival methods: (1) it does not destroy information by binning or averaging the data (as do, say,  $\chi^2$ ,  $\langle V/V_{\max} \rangle$ , and analyses of flux or angular moments); (2) it straightforwardly handles uncertainties in the measured quantities; (3) it analyzes the strength and direction information jointly; (4) it uses information available about nondetections; and (5) it automatically identifies and accounts for biases and selection effects, given a precise description of the experiment.

In this work we use the Bayesian methodology to make inferences about isotropic models for the distribution of burst sites, using data from the *Third BATSE Catalog* (Fishman et al. 1996, hereafter the 3B catalog; the 3B catalog inherits some properties of the First BATSE (1B) catalog described in Fishman et al. 1994). A companion paper (Loredo and Wasserman 1996) uses the same methodology to make inferences about anisotropic models, including comparisons of isotropic and anisotropic models.

In the next section, we briefly review the Bayesian methodology and the form of the likelihood

function for burst data. The 3B catalog does not provide all of the information required for a rigorous analysis, so we are forced to approximate some of the quantities required for calculating the likelihood. In § 3 we describe the approximations necessary to calculate the likelihood function based on the data available in the 3B catalog. Consistency requires that data for some bursts be omitted from the analysis when the approximations fail for those bursts, so we carefully discuss selection of the analyzable data. The most serious data cut arises from inaccuracy of the approximation used to calculate the detection efficiency reported in the 1B catalog for bursts with low fluxes. We describe extensive simulations we performed to quantify the inaccuracy of the approximation, and find that a significant fraction of bursts must be omitted from the analysis to avoid seriously corrupting the inferences drawn. Previous analyses of the BATSE data have not worried about inaccuracies introduced by improperly including dim bursts; this may account for some of the differences between our conclusions and those reached in other analyses.

We carry out our analysis in § 3 and throughout the remainder of the paper using data based on peak photon number flux measurements taken on both 64 ms and 1024 ms time scales. We analyze these data separately; they are not independent, but their dependence is too complicated to quantify with the data tabulated in the 3B catalog alone. An important conclusion of our analyses is that inferences drawn from these two data sets differ substantially, although the formal significance of the discrepancy cannot be determined without more information about the bursts comprising the catalog. We make an effort to understand and quantify this discrepancy in the final sections of this paper. Although we cannot conclusively identify the reason for the discrepancy, we suggest that it is a result of burst light curves having peak durations that are often significantly shorter than 1024 ms (and possibly shorter than 64 ms) and that may be correlated with burst intensity. The resulting errors in peak flux estimates distort the peak flux distribution; the distortion differs for the two data sets, and can potentially account for their significantly different shapes.

We begin, however, with models that do not attempt to account for any effects the different time scales of the data sets may have on the shape of the observed distribution of burst intensities. For brevity, we deem such models “simple” models. In § 4 we present results of analyses of simple phenomenological models for the differential burst rate (the burst rate per unit peak flux,  $\Phi$ ). These models help us ascertain what features must be present in the burst rate without committing us to a particular physical explanation for these features. They indicate that the distribution of 64 ms peak fluxes is adequately fit by a single power law whose logarithmic slope is very significantly different from the  $-2.5$  value associated with the differential rate for an unbounded homogeneous population of sources. There is no significant evidence for steepening of the distribution with intensity, contrary to the suggestions of such steepening we found in the 1B catalog (Loredo and Wasserman 1993). In contrast, the 1024 ms peak flux data prefer models with a broken power law distribution, and the low flux part of the distribution is significantly shallower than the distribution of 64 ms peak fluxes. In § 5 we present results of analyses of three simple cosmological models for the burst source distribution. The simplest model presumes that

all burst sources have the same intrinsic luminosity (they are “standard candles”), and that the burst rate per unit comoving volume is constant with redshift,  $z$ . Next, we consider standard candle sources with a burst rate density that varies as a power of  $(1 + z)$ . Finally, we consider models with power-law luminosity functions and constant comoving burst rate density. We find that our ignorance of the additional parameters in models with density evolution or a luminosity function greatly weakens our ability to learn about the spatial distribution and luminosity of the sources of bursts. As with the simple phenomenological models, these models reveal systematic discrepancies between the 64 ms and 1024 ms data.

In § 6 we discuss how properties of burst light curves might lead to time scale-dependent distortions of the observed flux distribution qualitatively capable of reconciling the two data sets. That such effects might prove crucial for making inferences from burst peak flux data was already anticipated in LW95; other authors have also previously remarked on the importance of these effects for understanding the flux distribution of bursts (Lamb, Graziani, and Smith 1993; Petrosian, Lee, and Azzam 1994). Following a general discussion, we analyze a more complicated phenomenological model than those of earlier sections that takes into account the different measuring time scales of the data sets. It is only moderately successful at reconciling the data sets, but remains of interest as an example of how one can explicitly account for time scale dependent effects in models.

In § 7 we analyze a final physical model that draws together several of the lines of thought developed in the preceding sections. In this model, burst sources are standard candles and standard clocks in their rest frames, but undergo relativistic motion with respect to locally comoving observers. An isotropic distribution of beaming angles with respect to the line of sight results in an effective luminosity function that is a power law if the rest frame emission spectrum is a power law. In the absence of time scale effects, this model is thus identical to the cosmological model with a power law luminosity function considered in § 5, except that the power law index is a function of the burst spectral index, rather than a free parameter. Beaming also results in bursts having observed peak durations that are a function of luminosity, allowing us to model time scale effects; cosmological redshift additionally correlates duration and peak flux. Thus besides being a model of intrinsic physical interest, this model indicates how both the temporal and spectral properties of bursts can influence the flux distribution in a manner that can be straightforwardly modeled.

The final section summarizes our findings and their implications. Two technical appendices describe the details of our cosmological models.

## 2. Review of Methodology

## 2.1. The Differential Burst Rate

In order to assess candidate hypotheses about burst sources with Bayesian methods using observed burst directions and strengths, the hypotheses must specify the *differential burst rate*: the rate of bursts per unit time per unit peak flux per unit steradian. We denote it by  $dR/d\Phi d\mathbf{n}$ , where  $\mathbf{n}$  denotes a direction on the sky, and  $\Phi$  denotes the time-averaged peak photon number flux between 60 and 300 keV (the nominal trigger range for the 3B catalog), averaged over the trigger time scale  $\delta t$  (64, 256, or 1024 ms for BATSE). The differential burst rate could vary in time, but in this work we consider only rates that are time-independent.

Phenomenological models specify  $dR/d\Phi d\mathbf{n}$  directly as an ad hoc parameterized function of flux and direction. For physical hypotheses about the sites of bursts, the differential rate is derived from more fundamental rates such as the burst rate per unit volume in space, and the burst luminosity function. For example, let  $\Lambda$  denote the peak photon number luminosity of a burst source in the spectral range used for flux measurements, and let  $\dot{n}(\mathbf{r}, \Lambda)$  denote the *burst rate density*, the number of bursts occurring per unit time, volume, and peak luminosity at position  $\mathbf{r}$  with peak luminosity  $\Lambda$ . We presume here that the emission is isotropic. For models with a small enough length scale that spacetime curvature can be ignored, we can calculate the differential burst rate according to

$$\frac{dR}{d\Phi d\mathbf{n}} = \int dr r^2 \int d\Lambda \dot{n}(\mathbf{r}, \Lambda) \delta[\Phi - \Phi_{\text{obs}}(\mathbf{r}, \Lambda)], \quad (1)$$

where  $r$  is a radial coordinate and  $\Phi_{\text{obs}}(\mathbf{r}, \Lambda)$  specifies the peak flux observed at Earth due to a source at position  $\mathbf{r}$  and luminosity  $\Lambda$ . The observed flux follows from the inverse-square law:

$$\Phi_{\text{obs}}(\mathbf{r}, \Lambda) = \frac{\Lambda}{4\pi r^2}. \quad (2)$$

Later in this work we employ a similar integral expression for cosmological models, generalizing the volume element, burst rate density, and observed flux function to account for the effects of spacetime curvature.

## 2.2. Bayes's Theorem

We compare alternative hypotheses for the differential burst rate by calculating their probabilities with Bayes's theorem. The nature of the resulting calculations depends on the type of hypothesis being considered. In practice, we distinguish between two kinds of hypotheses. In *parameter estimation* we calculate probabilities for hypotheses about the values of parameters in a particular differential rate model. In *model comparison* we calculate probabilities for competing parameterized models, presuming that one of the models being considered is true. We now briefly describe these two types of calculations in turn. Gregory and Loredo (1992) proved a somewhat more extensive review and further references.

The goal of Bayesian parameter estimation is to calculate probabilities for hypotheses about parameter values (e.g., for statements like “the burst source luminosity is between  $a$  and  $b$ ”). The probability for any hypothesis about parameter values can be calculated from the posterior probability *density* for the parameters. Denoting the information specifying the model by  $M$ , the parameters by  $\mathcal{P}$ , and the data by  $D$ , Bayes’s theorem for the posterior density is,

$$p(\mathcal{P} \mid D, M) = p(\mathcal{P} \mid M) \frac{p(D \mid \mathcal{P}, M)}{p(D \mid M)}. \quad (3)$$

The first factor is the prior density for the parameters. The numerator in the ratio is called the sampling probability for the data when its functional dependence on  $D$  is of primary interest, or the likelihood for the parameters when its functional dependence on the parameters is of primary interest, as it is here. The term in the denominator does not depend on  $\mathcal{P}$ , and plays the role of a normalization constant. It can be calculated simply by integrating the product of the prior and the likelihood over  $\mathcal{P}$ .

Since the dependence of the likelihood on  $\mathcal{P}$  is of central concern in parameter estimation, we suppress its dependence on  $D$  and  $M$ , and denote the likelihood function by  $\mathcal{L}(\mathcal{P})$ . We discuss this important function further below. For the prior density we simply use a constant function with respect to either the parameter, or its logarithm for the case of scale parameters. To indicate which of these two priors we use, we adopt the convention of plotting the posterior with logarithmic parameter axes for those parameters with a log-constant prior, and with linear axes for those parameters with a constant prior. All of our priors and posteriors are normalized over the ranges displayed in the figures.

As long as the prior density does not vary strongly over the width of the likelihood function, the details of the prior do not significantly affect parameter estimates. We note below those cases where our results are sensitive to the form of the prior; such behavior simply indicates that the data are uninformative with respect to the hypotheses under consideration.

In Bayesian model comparison we presume that one of a specified class of models is true, and calculate the probabilities for the various models in order to determine which model is best supported by the data. A model can have undetermined parameters, in which case we seek the probability for the model as a whole, taking into account parameter uncertainty. If we denote the models by the symbols  $M_i$ , and let the proposition  $I$  specify the set of models being considered, then Bayes’s theorem for the probability for model  $M_i$  takes a form very similar to equation (3):

$$p(M_i \mid D, I) = p(M_i \mid I) \frac{p(D \mid M_i)}{p(D \mid I)}. \quad (4)$$

Here  $p(M_i \mid I)$  is the prior probability for model  $M_i$ . The term in the denominator, which is independent of  $M_i$ , is simply a normalization constant. The term in the numerator is the global likelihood for  $M_i$ , or the prior predictive probability for the data presuming  $M_i$  is the correct model. Formally, we should write it as  $p(D \mid M_i, I)$ ; but the  $I$  proposition is redundant here (it asserts that one of the models being considered must be true; but  $M_i$  asserts that a particular

model is the true one). As written, it is clear that the global likelihood is simply the normalization constant one would calculate for parameter estimation with model  $M_i$  (i.e., the denominator in equation (3)). Although this quantity is of little intrinsic interest for parameter estimation, it is the key quantity for model comparison, playing the same role here as the likelihood function does for parameter estimation. This is why we call it the global likelihood for the model.

In practice, it is easier to work with ratios of model probabilities than with the probabilities themselves, since in the ratio the normalization constant,  $p(D | I)$ , cancels and thus need not be calculated. Also, if additional models are later added to the calculation, the probabilities for the originally considered models will change, but the ratios of these probabilities to each other will not; this is a further convenience of probability ratios, which are called *odds*. The odds in favor of  $M_i$  over  $M_j$  is

$$O_{ij} = \frac{p(M_i | I)}{p(M_j | I)} \frac{p(D | M_i)}{p(D | M_j)}, \quad (5)$$

where the first factor is the prior odds, and the second factor is the ratio of global likelihoods, also called the *Bayes factor*. The prior odds expresses how prior information (perhaps subjective) distinguishes between the models; the Bayes factor compares how the models predict the data. If we assign equal prior probabilities for the models (as we do throughout this work), the odds is given by the data-dependent Bayes factor. Interestingly, even when one uses equal prior probabilities, the odds can significantly favor a simpler model over a more complicated one (which may include the simpler one as a special case). Bayesian model comparison implements an automatic and objective “Ockham’s razor” that penalizes models for having excessively large parameter spaces, and in this way guards against unjustified preference for complicated models.

As noted above, we can calculate the global likelihood for a model simply by integrating the product of the prior and likelihood for the model’s parameters. If we denote the parameters for model  $i$  by  $\mathcal{P}_i$ , then

$$p(D | M_i) = \int d\mathcal{P}_i p(\mathcal{P}_i | M_i) \mathcal{L}(\mathcal{P}_i). \quad (6)$$

This equation reveals that the global likelihood for a model is the *average* likelihood for the model’s parameters, the averaging weight being simply the prior density for the parameters. The Bayes factor is thus a ratio of average likelihoods. In contrast, frequentist model comparison is based on ratios of *maximum* likelihoods. It is the averaging that takes place in global likelihood calculations that is responsible for the Ockham’s razor effect in Bayesian model comparison. A model with a larger parameter space than a simpler alternative has a smaller prior density in the vicinity of the likelihood peak, since its prior density is spread over a larger parameter space. Its global likelihood will be larger than that of its alternative only if the likelihood is large enough to make up for this smaller prior.

A consequence of this behavior is that the value of the global likelihood for a model depends much more sensitively on the prior for its parameters—and in particular, on the width of the prior—than do parameter estimates. Here we use constant priors; useful model comparison

calculations require that we specify finite prior ranges for any parameters not common to all models being considered. The global likelihood is then roughly inversely proportional to the prior range that we have explored. All of the Bayes factors quoted here are ratios of global likelihoods calculated with priors normalized over the ranges displayed in plots of posterior distributions.

### 2.3. The Likelihood Function

In traditional frequentist statistical methods, it is up to the user to specify the function of data to be used to draw inferences. Typical choices include various moments of the data, counts of data sorted into bins, some measure of misfit (such as  $\chi^2$  or a Kolmogorov-Smirnov statistic), or some statistic based on the likelihood function. In contrast, Bayesian methods offer the user no freedom of choice: the data enter Bayesian inferences through the entire likelihood function. In LW95 we gave a detailed derivation of the form of the likelihood function for GRB data such as that provided by BATSE. It can be written as

$$\mathcal{L}(\mathcal{P}) = \exp \left[ -T \int d\Phi \int d\mathbf{n} \bar{\eta}(\Phi, \mathbf{n}) \frac{dR}{d\Phi d\mathbf{n}} \right] \prod_i \int d\Phi \int d\mathbf{n} \mathcal{L}_i(\Phi, \mathbf{n}) \frac{dR}{d\Phi d\mathbf{n}}. \quad (7)$$

Here  $T$  is the duration of the observations;  $\bar{\eta}(\Phi, \mathbf{n})$  is the time-averaged detection efficiency for bursts of flux  $\Phi$  from direction  $\mathbf{n}$ ; and  $\mathcal{L}_i(\Phi, \mathbf{n})$  is the probability for seeing the data for burst  $i$ , presuming it comes from a burst with peak flux  $\Phi$  and direction  $\mathbf{n}$ . We call  $\mathcal{L}_i(\Phi, \mathbf{n})$  the individual burst likelihood function; it is the function one would use to infer the properties of a particular burst. LW95 derive expressions for  $\bar{\eta}(\Phi, \mathbf{n})$  and  $\mathcal{L}_i(\Phi, \mathbf{n})$  in terms of raw photon count data in the eight BATSE detectors.

### 2.4. Marginal Distribution for Shape Parameters

Most models for the differential burst rate have among their parameters an overall *scale factor*,  $A$ , such that we can write

$$\frac{dR}{d\Phi d\mathbf{n}} = A \rho(\Phi, \mathbf{n}; \mathcal{P}'), \quad (8)$$

where  $\mathcal{P}'$  denotes the remaining parameters, which we call *shape parameters*. The scale factor is typically some measure of the burst rate per unit volume, while the shape parameters define the geometry of the burst distribution and the physical parameters of individual burst sources (such as their characteristic luminosity). Many questions about burst sources refer only to shape parameters. Thus it is useful to eliminate the scale factor from the analysis.

An important advantage of Bayesian methods over their frequentist counterparts is that they allow straightforward inferences about an interesting subset of model parameters in a manner that fully accounts for the uncertainty in the neglected parameters. Such inferences are obtained by *marginalizing*: integrating the full joint posterior distribution with respect to the uninteresting

parameters. Marginalization of the amplitude parameter (using a log-constant prior) can be performed analytically. LW95 show that the resulting marginal likelihood for the shape parameters is

$$\mathcal{L}(\mathcal{P}') = \prod_i \frac{\int d\Phi \int d\mathbf{n} \mathcal{L}_i(\Phi, \mathbf{n}) \rho(\Phi, \mathbf{n})}{\int d\Phi \int d\mathbf{n} \bar{\eta}(\Phi, \mathbf{n}) \rho(\Phi, \mathbf{n})}. \quad (9)$$

As mentioned above, we use flat prior densities for shape parameters (or their logarithm) throughout this work; thus the posterior distribution for the shape parameters (or their logarithm) is simply the marginal likelihood, normalized with respect to its arguments.

## 2.5. Likelihood Functions for Isotropic Models

In this work we consider only isotropic differential rates, for which

$$\frac{dR}{d\Phi d\mathbf{n}} = \frac{1}{4\pi} \frac{dR}{d\Phi}, \quad (10)$$

where  $dR/d\Phi$  denotes the burst rate per unit flux from *all* directions. If the differential rate is derived from an isotropic physical model for the burst rate density, the counterpart to equation (1) is

$$\frac{dR}{d\Phi} = 4\pi \int dr r^2 \int d\Lambda \dot{n}(r, \Lambda) \delta[\Phi - \Phi_{\text{obs}}(r, \Lambda)], \quad (11)$$

where  $\dot{n}$  and  $\Phi_{\text{obs}}$  are now functions only of  $r$  and not additionally of direction.

The likelihood function can be simplified for isotropic models by performing the integrals over direction once for all. The full likelihood function becomes

$$\mathcal{L}(\Theta) = \exp\left[-T \int d\Phi \bar{\eta}'(\Phi) \frac{dR}{d\Phi}\right] \prod_i \int d\Phi \mathcal{L}_i(\Phi) \frac{dR}{d\Phi}, \quad (12)$$

where  $\bar{\eta}'(\Phi)$  is the direction and time averaged detection efficiency given by

$$\bar{\eta}'(\Phi) = \frac{1}{4\pi} \int d\mathbf{n} \bar{\eta}(\Phi, \mathbf{n}), \quad (13)$$

and  $\mathcal{L}_i(\Phi) = \int d\mathbf{n} \mathcal{L}_i(\Phi, \mathbf{n})$ . This is the likelihood function used below when the amplitude parameter is of interest.

Similarly, writing  $dR/d\Phi = A\rho(\Phi)$ , the marginal likelihood for the shape parameters becomes

$$\mathcal{L}(\mathcal{P}) = \prod_i \frac{\int d\Phi \mathcal{L}_i(\Phi) \rho(\Phi)}{\int d\Phi \bar{\eta}'(\Phi) \rho(\Phi)}. \quad (14)$$

This is the likelihood function used below when only the shape parameters are of interest.

### 3. Approximations

As noted above, LW95 derive expressions for  $\bar{\eta}(\Phi, \mathbf{n})$  and  $\mathcal{L}_i(\Phi, \mathbf{n})$  in terms of raw photon count data in the eight BATSE detectors. However, these functions are not directly reported in the 3B catalog, so we must approximate them using the reported information. The approximations in turn require us to omit from our analyses data for which the approximation would be poor.

#### 3.1. Individual Burst Likelihood Functions

The  $\mathcal{L}_i(\Phi, \mathbf{n})$  functions could be well approximated by functions proportional to  $\exp[-\chi^2(\Phi, \mathbf{n})/2]$  for each burst, where  $\chi^2(\Phi, \mathbf{n})$  is the familiar goodness-of-fit measure, given as a function of peak flux and direction. The 3B catalog does not provide  $\chi^2$  functions for each burst, but instead provides simple summaries of the behavior of  $\chi^2$  near the best-fit  $\Phi$  and  $\mathbf{n}$  consisting of best-fit values and simple measures of the widths of independent confidence regions for  $\Phi$  and  $\mathbf{n}$ . We thus approximate  $\mathcal{L}_i(\Phi, \mathbf{n})$  as a product of a Gaussian about the best-fit  $\Phi$  value (with width given by the reported standard deviation), and a Fisher distribution (a spherical generalization of the Gaussian) about the best-fit  $\mathbf{n}$  with a width derived from the reported direction errors. Thus we write

$$\mathcal{L}_i(\Phi, \mathbf{n}) \propto \exp\left[-\frac{(\Phi - \Phi_i)^2}{2\sigma_i^2}\right] \Theta(\Phi) e^{\kappa_i \mu}. \quad (15)$$

The first factor is the Gaussian distribution for the flux uncertainty, with  $\Phi_i$  the best-fit flux for burst  $i$  and  $\sigma_i$  the standard deviation for the peak flux; both quantities are reported in the 3B catalog (one set for each of the three trigger time scales). The Heaviside function,  $\Theta(\Phi)$ , merely restricts the Gaussian to positive flux values. A more rigorous likelihood might truncate more smoothly, but the best-fit fluxes of the 3B bursts are all sufficiently positive that this truncation occurs at least a few standard deviations away from  $\Phi_i$  and thus has little effect on the results.

The last exponential factor is the Fisher distribution describing the direction uncertainties. Although it is irrelevant for the analysis of isotropic models, it is important for analyses of anisotropic models that we will present in subsequent papers, so we discuss it here. It is azimuthally symmetric about the burst direction; we have written it in terms of spherical coordinates with the polar axis aligned with the best-fit burst direction, so that  $\mu = \cos \theta$ , with  $\theta$  the polar angle. If we work in Galactic coordinates, so that  $\mathbf{n} = (l, b)$  with  $l$  the Galactic longitude and  $b$  the Galactic latitude, then

$$\mu = \sin b \sin b_i + \cos b \cos b_i \sin(l - l_i), \quad (16)$$

where the best-fit Galactic longitude and latitude for the burst are  $l_i$  and  $b_i$ . The concentration parameter,  $\kappa_i$ , specifies the width of the Fisher distribution. The 3B catalog reports the angular size,  $\delta\theta_i$ , of a 68% confidence circle for each burst. The corresponding value of  $\kappa_i$  is that which makes the 3B confidence circle contain 68% of the probability according to the Fisher distribution.

This value can be found by solving the following nonlinear equation for  $\kappa_i$ :

$$\frac{\kappa_i}{2 \sinh \kappa_i} \int_{\cos \delta\theta_i}^1 d\mu e^{\kappa_i \mu} = 0.68. \quad (17)$$

For small values of  $\delta\theta_i$  (corresponding to large values of  $\kappa_i$ ), this gives  $\kappa_i \approx 2.3/(\delta\theta_i)^2$ ; we use the exact (numerical) solution in our analysis. Also, the value of  $\delta\theta_i$  we use combines the statistical uncertainty,  $\delta\theta_{i,\text{stat}}$ , reported in the 3B tables with the systematic uncertainty,  $\delta\theta_{\text{sys}}$ , estimated by the BATSE team to be  $1.6^\circ$ . We combine these uncertainties in quadrature, so that

$$\delta\theta_i = \left[ (\delta\theta_{i,\text{stat}})^2 + (\delta\theta_{\text{sys}})^2 \right]^{1/2}, \quad (18)$$

as recommended in the 3B catalog. We note that Graziani (1995) has found evidence both that the average size of the systematic error may be underestimated, and that there are significant correlations between the size of the systematic error and the size of the statistical error, although the limited calibration data available prohibits careful measurement of such correlations over the entire dynamic range of bursts. As we discuss further in the companion paper, these findings appear to have negligible import for the analysis of models with large scale anisotropy, such as those we analyze in this series of papers. However, they may prove quite crucial in analyzing models with small scale structure (such as models with repeating burst sites).

As already noted, equation (15) is an approximation to the actual individual event likelihood function. The principal weakness of this approximation is probably omission of correlations between the three arguments of the event likelihood (peak flux and two angles). As noted in LW95, the correlations between the flux and either angle variable are probably not strong because of compensating correlations in the likelihood factors for detectors on opposite sides of the spacecraft; Pendleton et al. (1992) reach a similar conclusion empirically. But correlations between inferred values of the two angles needed to specify the burst direction can be fairly strong; they are exhibited by noncircular contours in the  $\chi^2$  maps for the burst directions. A superior approximation would take into account ellipticity in the contours (e.g., by replacing the Fisher distribution with a Kent distribution). Accounting for such correlations is probably crucial for assessing hypotheses with small angular scales, such as models invoking repeating burst sites or angular correlations between burst sites. But the axisymmetric approximation we use should be entirely adequate for the analysis of models with only large-scale angular structure, and in any case has no effect on analyses of isotropic models such as those reported here.

Another possibly important weakness is that the behavior of the true likelihood away from its peak may be non-Gaussian in  $\Phi$  or non-Fisher in  $\mathbf{n}$ . For example, the true likelihood may decrease less rapidly than do these exponential distributions. This possible shortcoming is noted in the 3B catalog, but no information is provided (such as the sizes of error circles or ellipses at confidence levels greater than 68%) that would allow us to quantitatively assess the accuracy of our approximation in this regard.

### 3.2. Detection Efficiency

Approximating the detection efficiency is problematical because several important elements of a proper efficiency calculation were omitted from the 3B catalog calculations. Rather than report  $\bar{\eta}(\Phi, \mathbf{n})$  as a joint, three-dimensional function of  $\Phi$  and  $\mathbf{n}$ , the 3B catalog instead reports two simple functions indicating the detection sensitivity as a function of flux and of declination. Fortunately, the correlations between  $\Phi$  and  $\mathbf{n}$ , and the dependence on right ascension, are expected to be quite weak at all but the lowest fluxes.

More seriously, the 3B calculations ignore Poisson fluctuations in the count rate and the contribution to the count rate from atmospheric scattering of gamma rays, which increases the effective areas of the eight BATSE detectors. Both of these effects are important for properly calculating the efficiency for detecting weak bursts.

We have performed extensive simulations of an idealized BATSE instrument to determine when the neglected terms become important. The simulated instrument consisted of eight detectors arranged in the same octagonal geometry as the eight BATSE detectors. The simulated orbit was circular and equatorial, at a fixed altitude of 400 km. During the course of the simulated observations, the satellite spent equal time in each of 15 different pointings (the first 15 pointings of BATSE’s observing plan). Each detector had an area equal to the nominal area of a BATSE detector (1500 cm<sup>2</sup>), and a purely geometric angular response function in the outward hemisphere (i.e., proportional to the cosine of the angle between the burst direction and the outward normal). In addition, an atmospheric scattering component was included by isotropically scattering half of the gamma rays incident at each point on Earth in the outward hemisphere of that point (the other half we presume to be absorbed). Each detector had a background rate equal to the nominal background rate in a BATSE detector (2255 ct s<sup>-1</sup>), and a trigger threshold set at a number of counts 5.5 standard deviations above that expected from the background in the trigger interval  $\delta t$  (the nominal BATSE trigger criterion).

We simulated burst observations by picking a burst direction from an isotropic distribution, and by picking a burst peak flux from a smooth broken power law distribution that had a differential slope of 1.5 below a peak flux of 7 ct cm<sup>-2</sup> s<sup>-1</sup> and 2.5 (the slope expected from a homogeneous isotropic burst site distribution) above that flux. This purely phenomenological flux distribution is similar to that expected from a variety of physical models, and is discussed further below. Once a burst was chosen, we calculated the expected counts in the eight detectors (presuming a constant peak flux throughout  $\delta t$ ) and chose actual values for the detected counts from Poisson distributions that took into account the background rate. The burst was detected only if the counts equaled or exceeded the threshold value in two or more detectors. For detected bursts, we calculated exact individual event likelihood functions as described in LW95, and derived from them summaries corresponding to those published in the 3B catalog.

We simulated 10 sets of 400 bursts using a 64 ms trigger time scale (each set thus had a number of bursts comparable to the number of 3B bursts with sufficient information to perform

a Bayesian analysis). For each set, we calculated the likelihood for the smooth broken power law model with its parameters fixed at the true values. Then we maximized the likelihood by allowing the break flux and the slope below the break to vary, and calculated the logarithm of the ratio of the maximum and true likelihoods,  $\Delta L$  (this corresponds to the analysis we perform in § 4, below). We performed this calculation using the actual detection efficiency, calculated as specified in LW95, and also using an approximate detection efficiency that ignores Poisson fluctuations and atmospheric scattering, as does the efficiency reported in the 3B catalog. We denote these values  $\Delta L_{\text{true}}$ , and  $\Delta L_{\text{approx}}$ , respectively. A comparison of the  $\Delta L$  values from analyses based on the true and approximate efficiency indicates how accurately the likelihood function based on the approximate efficiency is; by using the ratio, we concentrate on the shape of the likelihood function, since its overall normalization is irrelevant.

Figure 1 shows the the true and approximate average efficiencies when the simulated detector is operated with a 64 ms trigger time scale. The dotted curve shows the approximate result, ignoring counting uncertainties and atmospheric scattering (corresponding to the procedure used in the 3B catalog). The dashed curve incorporates counting uncertainties; they broaden the region over which the efficiency falls, allowing the efficiency to be nonzero at all positive fluxes (although it is very small at fluxes near zero). The solid curve is the true efficiency, incorporating both counting uncertainties and atmospheric scattering. Atmospheric scattering shifts the low-flux cutoff to smaller values.

Figure 2a shows the  $\Delta L$  values found for each of the 10 simulated data sets, displayed as a scatterplot showing the approximate  $\Delta L$  versus the true  $\Delta L$ . To set a useful scale to this plot, note that an approximate 68% credible region for a single parameter is bounded by a likelihood contour with a log likelihood one less than the maximum. We thus need  $\Delta L$  to be accurate to within an additive error  $\ll 1$  if our inferences are to be accurate. It is clear from Figure 2a that the approximate efficiency seriously corrupts inferences, leading to  $\Delta L_{\text{approx}}$  values unacceptably different from the true values.

Figure 1 reveals that counting uncertainties and atmospheric scattering affect the detection efficiency most strongly at low fluxes. We therefore studied how well the approximation performed when bursts dimmer than a specified cutoff flux were omitted from the analysis and the efficiency function was truncated at that flux. Such truncation of the data and efficiency is not completely self-consistent, since  $\bar{\eta}'(\Phi)$  is the probability for detecting a burst whose *true* peak flux is  $\Phi$ , but we can only truncate the data based on the *estimated* peak flux values. We hoped that the flux uncertainties would be small enough that the inconsistency would not corrupt the analysis. That this hope is realizable is made clear in Figures 2b and 2c. These Figures show  $\Delta L$  scatterplots when the data and efficiency are truncated at increasing values of  $\Phi$ . Once the threshold flux reaches  $1.5 \text{ cm}^{-2} \text{ s}^{-1}$ , analyses using the approximate 64 ms efficiency accurately duplicate the results of analyses using the true efficiency. Similar calculations based on a 1024 ms trigger time scale indicate that the 1024 ms efficiency and data must be truncated at  $\Phi = 0.4 \text{ cm}^{-2} \text{ s}^{-1}$ .

In LW95 we noted that the detection efficiency is also a function of the burst spectrum and peak duration. The efficiency reported in the 3B catalog was calculated for a single burst spectrum (a power law falling with photon energy  $\epsilon$  like  $\epsilon^{-1.5}$ ); the catalog reports that the efficiency changes significantly at low fluxes if one steepens the spectrum to  $\propto \epsilon^{-2.5}$ , a spectrum not atypical of some bursts (as we note in § 5). No effort was made to quantify the dependence on peak duration. Without further information, we cannot ascertain the effect of these omissions on our results. Hopefully, these effects are minor for bursts with fluxes above our cutoff values.

### 3.3. Data Selection

Having settled on approximations for the  $\mathcal{L}_i$  and  $\bar{\eta}'$  functions, we can analyze only those data for which the approximations are acceptable. Here we summarize all of the resulting selections, some of which were mentioned above.

First, although the 3B catalog contains information about 1122 bursts, many of the bursts triggered the BATSE instrument on only one or two of the three trigger time scales. Only 453 of these bursts triggered the instrument on the 64 ms time scale; 557 bursts triggered the instrument on the 1024 ms time scale. We can hope to model selection effects only for these subsets of the full catalog.

A complication in BATSE’s triggering criterion results in a further cut. Once a burst triggers BATSE, it takes roughly 90 minutes to transmit the burst data to Earth. During this readout period, further triggering is disabled on the 256 and 1024 ms time scales, and the threshold for 64 ms triggers is increased to the peak value seen in the detected burst. The reported efficiency does not take into account BATSE’s change in threshold upon detection of a burst, and so does not accurately describe BATSE’s 64 ms detection efficiency for the readout period. Thus all data for bursts detected during such periods (even if the previous trigger was later identified as a solar flare or some other non-GRB event) must be omitted from the analysis. In the parlance of the 3B catalog, these are bursts that “overwrote” a previous trigger.

For a few bursts observed during the second year of operation of the BATSE instrument, data gaps caused by failure of the on-board tape recorder resulted in these bursts having insufficient data for estimating a peak flux or a reliable direction uncertainty. Similar limitations may also have arisen for particularly weak bursts. In principle, what little information that is available could be used to specify broad individual event likelihood functions for these bursts (for example, we may know that the peak flux for a particular burst is above some value, and could construct an event likelihood function that reflects this constraint). In practice, the 3B catalog reports no useful information about the individual event likelihood functions for these bursts, so they must be omitted from the analysis. After omitting overwrites and bursts without sufficient direction or flux information, 407 bursts remain available on the 64 ms time scale, and 554 on the 1024 ms time scale.

Finally, as already noted, the approximation used to calculate the detection efficiency reported in the 3B catalog fails at low flux values, so we must truncate the efficiency below some critical flux and omit bursts with best-fit fluxes below that value from the analysis. The critical flux values are different for data based on different trigger time scales and are identified above. Unfortunately, this requires that we omit nearly a third of the remaining 64 ms bursts, and about 16% of the remaining 1024 ms bursts.

As a result of these cuts, the portion of the 3B catalog suitable for a consistent statistical analysis contains 279 bursts triggered on the 64 ms time scale and 463 bursts triggered on the 1024 ms time scale. Data from each time scale must be analyzed separately, and the results of such analyses are not independent. We present here only the results of analyses of the 64 ms and 1024 ms data (i.e., we present no results based on the intermediate 256 ms time scale). We will find that analyses of these two data sets often lead to different conclusions about the shape of the burst distribution, indicating that modeling the temporal properties of bursts is probably important for fully understanding the distribution of burst strengths and directions; we describe preliminary modeling along these lines below. In several cases we have additionally studied the 256 ms data, and found that its implications are always intermediate between the 64 ms and 1024 ms data (for example, if a power law index inferred from the 64 ms data is larger than that inferred from the 1024 ms data, then that inferred from the 256 ms data lies between the two). This may be further evidence that the trends we find are real; but this is difficult to ascertain because of the lack of independence of the data sets and the limited information provided about each burst in the 3B catalog.

We emphasize that our data selection is based simply on internal consistency among elements of the published catalog. The resulting subsets of data are thus the usable subsets for *any* analysis of the peak flux data, not just for our Bayesian analyses.

Finally, we note that although the number of bursts in the 1024 ms subset is much larger than that in the 64 ms subset, the number of bursts in the 1024 ms subset with estimated peak fluxes above  $1.5 \text{ cm}^{-2} \text{ s}^{-1}$  (the cutoff for 64 ms data) is only 156, far below the number in the 64 ms data set (279). The published detection efficiencies for both timescales are nearly identical above  $1.5 \text{ cm}^{-2} \text{ s}^{-1}$ . It must then be the case that data taken with different triggering time scales represent significantly different samplings of the intrinsic peak flux distribution. Lamb, Graziani, and Smith (1993) have previously pointed out that a particular burst can have very different 64 ms and 1024 ms peak intensities; Mao, Narayan, and Piran (1993) have made similar observations. As a result, bursts spanning a certain range of peak intensities in the 64 ms data may span a very different range in the 1024 ms data. We will see below that this “shuffling” of peak intensities distorts the shape of the observed intensity distribution, so that inferences based on data from different timescales can differ significantly. All previous analyses of burst distribution models have used data from only one timescale (usually 1024 ms), and have thus overlooked this effect.

#### 4. Simple Phenomenological Models

We begin by analyzing two phenomenological models to get a sense of what information is in the data, independent of a particular physical model for the burst distribution. These models simply specify a parameterized functional form for  $dR/d\Phi$  directly, rather than deriving the differential rate from an hypothesized physical burst distribution. The forms we explore involve power laws. Despite being purely phenomenological, they have the potential to offer some insight into the physical burst distribution, because power-law differential distributions arise naturally from consideration of simple physical models.

As an example, consider the differential flux distribution resulting from sources that are standard candles distributed uniformly throughout an infinite Euclidean space. The rate of bursts from within a radius  $r$  grows like the volume, so that the cumulative rate from bursts closer than  $r$  obeys  $R(< r) \propto r^3$ ; thus the differential rate per unit radius follows  $dR/dr \propto r^2$ . We can change variables from  $r$  to flux by noting that  $\Phi \propto 1/r^2$ , which also implies that  $dr/d\Phi \propto \Phi^{-3/2}$ . Thus the differential rate obeys  $dR/d\Phi \propto \Phi^{-5/2}$ , and the cumulative rate obeys the familiar 3/2 law, with  $R(> \Phi) \propto \Phi^{-3/2}$ . Inferences about the power-law index therefore can be used to quantify acceptance or rejection of a homogeneous distribution.

More generally, suppose that the rate of bursts from within  $r$  grows like  $r^a$ , so that

$$\frac{dR}{dr} \propto r^{a-1}. \quad (19)$$

The homogeneous Euclidean case just described corresponds to  $a = 3$ . For burst sources distributed throughout a thin disk,  $a = 2$ , and for burst sources distributed throughout an isotropic  $1/r^2$  halo,  $a = 1$ . For a cosmological population of bursters it proves convenient to replace the radial coordinate  $r$  with the redshift  $z$  ( $r \propto z$  when  $z \ll 1$ ), writing  $dR/dz \propto z^{a-1}$ . If the cosmological population has a comoving burst rate density varying with  $z$  like  $(1+z)^{-\beta}$ , then  $a = 3$  (the Euclidean value) for bursts at small redshift (i.e., the brightest bursts); but for sources at large  $z$  we show in Appendix A that  $a = -(\frac{3}{2} + \beta)$ . From these examples it is clear that if we could infer  $a$ , we could potentially make important inferences about the geometry of the burst distribution.

Similarly, generalize the flux-distance relation so that

$$\Phi(r) \propto r^{-b}. \quad (20)$$

For bursts in Euclidean space,  $b = 2$ . For cosmological burst sources emitting  $\gamma$  rays of energy  $E$  with a power-law photon number spectrum proportional to  $E^{-\alpha}$ , the flux-distance relation has this same form for bright bursts originating from sources at low redshift. For sources at large redshift, it again is most convenient to switch from  $r$  to  $z$ , writing  $\Phi \propto z^{-b}$ . In this case we find in Appendix A that  $b = \alpha$ . If we could infer  $b$ , we could potentially identify a uniquely cosmological aspect to the burst data.

We can calculate the differential burst rate implied by these generalized laws by using equation (20) to change variables from  $r$  to  $\Phi$  in equation (19). The result is a differential rate that obeys

$$\frac{dR}{d\Phi} \propto \Phi^{-\left(\frac{a}{b}+1\right)}, \quad (21)$$

with the corresponding cumulative rate obeying  $R(> \Phi) \propto \Phi^{-a/b}$ . It is important to note that these power laws depend only on the ratio,  $a/b$ . Information about the radial behavior of the burst rate and the flux-distance relation are inextricably combined in the power-law slope of the differential burst rate. This simple result presages an unfortunate conclusion of our analyses below: that the flux distribution provides little constraint on cosmological scenarios for bursters once one considers source distributions more complicated than standard candles with a constant comoving burst rate (for which  $\beta = 0$  so that the behavior of  $a$  is fixed a priori).

The cosmological scenario distinguishes itself among the possibilities just discussed in that its power-law exponents change with  $\Phi$ . They take on the simple Euclidean values at large  $\Phi$  (corresponding to sources at redshifts  $z \ll 1$ ), but change to other values for the dimmest bursts. This change indicates the presence of characteristic distance and luminosity scales in the burst distribution. Quite generally, if the logarithmic slope of the differential rate changes in the vicinity of a characteristic flux  $\Phi_b$ , we can write

$$\Phi_b = \frac{\Lambda_c}{4\pi r_c^2}, \quad (22)$$

where  $\Lambda_c$  is a characteristic luminosity, and  $r_c$  is a characteristic distance. Detection of a break in the logarithmic slope thus has the potential of revealing information about scales for both the spatial and luminosity distribution. In cosmological models, the Hubble distance,  $c/H_0$  (with  $c$  the speed of light and  $H_0$  equal to Hubble's constant) provides a fixed characteristic length scale, so detection of a break allows measurement of the characteristic luminosity of cosmological bursters.

The Euclidean examples discussed above presume unbounded distributions, and thus have constant power law indices. If the burster distribution is bounded and bursters are standard candles, the differential rate will be bounded as well, falling to zero at the flux value associated with a burst viewed from the farthest boundary. But if bursters have a distribution of luminosities, information about that distribution can be extracted from the shape of the differential rate. As an illustrative example, consider the case of an isotropic distribution of sources with a power law luminosity function, so that

$$\dot{n}(\mathbf{r}, \Lambda) = \dot{n}(r)f(\Lambda), \quad (23)$$

where  $f(\Lambda)$  is a normalized power law with lower limit  $\Lambda_l$  and upper limit  $\Lambda_u$ , proportional to  $\Lambda^{-p}$ . If  $\dot{n}(r) \propto r^{a-3}$  (as assumed in eqn. (19)) inside  $r_c$ , but vanishes beyond  $r_c$ , then using equation (1) it is straightforward to show that

$$\frac{dR}{d\Phi} \propto \begin{cases} \Phi^{-p}, & \text{for } \Phi_l < \Phi < \Phi_b, \\ \Phi^{\frac{a}{2}+1}, & \text{for } \Phi > \Phi_b, \\ 0, & \text{for } \Phi < \Phi_l; \end{cases} \quad (24)$$

where  $\Phi_b = \Lambda_u/4\pi r_c^2$  and  $\Phi_l = \Lambda_l/4\pi r_c^2$ . Thus, when the luminosity function is a power law, the differential rate below the break directly mimics the luminosity function, potentially allowing us to infer its logarithmic slope. As shown by Wasserman (1992), similar behavior arises for cosmological bursters with a power-law luminosity function, except that the break is smoothed,  $c/H_0$  playing the role of  $r_c$  (see also Mészáros and Mészáros 1995).

To summarize, the logarithmic slope of the flux distribution contains information about the geometry of the burster distribution and the flux-distance relationship, folded together. A break in the distribution contains information about characteristic distance and luminosity scales in the burster distribution. Finally, the shape of the flux distribution below the break contains information about the luminosity function; for power-law luminosity functions, the differential flux distribution directly mimics the luminosity function. With this as motivation, we now turn to the analysis of phenomenological power law models for the 3B data.

#### 4.1. Power-Law Models

First, we consider a simple power-law model,  $M_1$ , with  $dR/d\Phi = A\Phi^{-\gamma}$ . This model has one shape parameter, the power-law index,  $\gamma$ . Figure 3 shows the log posterior as a function of  $\gamma$  using the 64 ms data (solid curve) and the 1024 ms data (dashed curve). The curves are very nearly parabolic, corresponding to nearly Gaussian posteriors. For the 64 ms data,  $\gamma = 2.1 \pm 0.12$ ; for the 1024 ms data,  $\gamma = 1.9 \pm 0.1$  (here and elsewhere we provide the mode and 95% credible region as parameter summaries); these best-fit parameter values appear in Table 1. The index corresponding to an isotropic distribution ( $\gamma = 2.5$ ) is outside even the “ $5\sigma$ ” range for both data sets.

The difference between the best-fit  $\gamma$  values indicates that the distribution of 64 ms fluxes falls off more quickly than does that of 1024 ms peak fluxes. Superficially, the discrepancy between the inferred slopes for the data sets appears only marginally significant, since the curves in Figure 3 overlap just inside their “ $2\sigma$ ” boundaries. However, these data sets are not independent since many bursts are common to both, so the difference is likely to be more significant than simple consideration of the sizes of credible regions for  $\gamma$  would imply. We will find that inferences based on these data sets differ for every model we investigate. This indicates that it is probably necessary to consider the temporal behavior of bursts explicitly in modeling and analysis of the flux distribution, a possibility we discussed in some detail in LW95. We discuss this further in § 6, and defer most discussion of the differences between the data sets to that section.

Figure 4a provides a graphical portrayal of how the best-fit power law model compares with the 64 ms data. Plotted are the normalized effective cumulative rate distribution,

$$F(> \Phi) = \frac{\int_{\Phi}^{\infty} d\Phi' \eta(\Phi') \frac{dR}{d\Phi'}}{\int_0^{\infty} d\Phi' \eta(\Phi') \frac{dR}{d\Phi'}}, \quad (25)$$

as a smooth curve, and a cumulative histogram of estimated burst fluxes,  $\Phi_i$ . The dotted curve,

associated with the right vertical axis, shows the negative logarithmic slope of  $F(> \Phi)$  as a function of  $\Phi$ . Figure 4b is a similar plot based on the 1024 ms data. In LW95 we discuss using such curves to graphically indicate the goodness of fit of a model; we emphasize that our analysis is not based on comparison of the cumulative histograms shown here.

## 4.2. Smooth Broken Power-Law Models

It is apparent from Figure 4b that a single power law does not describe the entire 1024 ms flux distribution very well; the distribution of bright bursts seems to fall off more rapidly with  $\Phi$  than does that of dim bursts. (Similar behavior is apparent in Figure 4a, but it is less decisive.) Also, *Pioneer Venus Orbiter* (PVO) burst observations imply that at bright fluxes ( $\Phi > 20\text{--}50 \text{ cm}^{-2} \text{ s}^{-1}$ ),  $dR/d\Phi \propto \Phi^{-2.5}$  for fluxes measured on a 256 ms time scale (Fenimore et al. 1992). Accordingly, we investigate a smooth broken power law model,  $M_2$ , with

$$\frac{dR}{d\Phi} = A \frac{(\Phi/\Phi_b)^{-\gamma_1}}{1 + (\Phi/\Phi_b)^{\gamma_2 - \gamma_1}}, \quad (26)$$

with  $\gamma_2 \equiv 2.5$  (thus fixing the logarithmic slope at large fluxes to that expected from a homogeneous source distribution). This model has two shape parameters, the logarithmic slope at low flux  $\gamma_1$ , and the break flux  $\Phi_b$ .

Figure 5a shows joint credible regions for  $\Phi_b$  and  $\gamma_1$ , based on the 64 ms data. The best-fit parameter values are listed in Table 1, as are three quantities useful for comparing this model to others we have studied: (1) the ratio,  $R_{21}$ , of the maximum likelihood for this model and that for the single power law model; (2) the asymptotic significance level,  $p(> R_{21})$ , associated with this likelihood ratio; and (3) the Bayes factor,  $B_{21}$  in favor of this model over the single power law model. (The significance level is the approximate long-run probability that one would falsely reject the simpler model if one were to reject it when the likelihood ratio is at least as large as that observed. Small values indicate high confidence in the complicated model. Asymptotically,  $-2 \log(R_{ij})$  is distributed as  $\chi^2_\nu$ , where  $\nu$  is the number of additional parameters in the more complicated model.) The Bayes factor indicates that the simpler single power law model is favored. The credible region is unbounded at large values of  $\Phi_b$  (the single power law model is the  $\Phi_b \rightarrow \infty$  limit of this model). Figure 6a shows the best-fit model; very little curvature is apparent. No 3B bursts have 64 ms peak fluxes above  $200 \text{ cm}^{-2} \text{ s}^{-1}$ , where the best-fit value of  $\Phi_b$  lies. Thus the location and unboundedness of the credible region indicate that these data do not provide significant evidence for a break in the logarithmic slope. This is further borne out by the maximum likelihood values: the maximum likelihood for the smooth broken power law model is only 1.3 times larger than that for the single power law model, not enough to justify its greater complexity. We conclude that there is no significant large-scale structure in the 64 ms flux distribution. Of course, these models may not be able to detect significant small scale structure (“bumps and wiggles”) in the distribution; but we do not know of any a priori reasons for such structure, and thus have not attempted to model and detect it.

Figure 5b shows joint credible regions for  $\Phi_b$  and  $\gamma_1$  for the 1024 ms data. The best-fit parameter values, likelihood ratio, and Bayes factor appear in Table 1. The 68% credible region is bounded at large values of  $\Phi_b$ , and the Bayes factor in favor of this model over the single power law model is 20, indicating a significant preference for the smooth broken power law model. But the 95% credible region extends to  $\Phi_b$  values well above  $1000 \text{ cm}^{-2} \text{ s}^{-1}$ . We interpret this as implying that the data require curvature in  $\log R$  vs.  $\log \Phi$ , but not necessarily a sharp break. The allowed values of  $\gamma_1$  are systematically smaller than the best-fit  $\gamma$  for a single power law, revealing that the 1024 ms data favor even more flattening at low  $\Phi$  than is implied by fits of single power law models. Figure 6b shows the best-fit model, illustrating how allowing curvature improves the fit, particularly at large flux values.

As a final simple phenomenological model,  $M_3$ , we considered the smooth broken power law model, but we allowed the upper power law index to vary. However, we changed parameters from the power law slope,  $\gamma_2$ , to the angle,  $\theta = \arctan(\gamma_2)$ , and we used a uniform prior from  $\theta = 1.1$  (corresponding to  $\gamma_2 \approx 2$ ) to  $\theta = 1.5$  (an  $85^\circ$  angle, corresponding to  $\gamma_2 \approx 15$ ). We introduced this reparameterization to facilitate exploring steep power laws for which a small change in angle results in a large change in power law index. Our uniform prior for  $\theta$  corresponds to a bounded Cauchy distribution prior for  $\gamma_2$ . This change has little effect on parameter estimates. However, it probably leads to a larger Bayes factor in favor of this model than would result from use of a flat prior on  $\gamma_2$ , simply because the size of the  $\theta$  parameter space is smaller.

Table 1 presents the best-fit parameter values and model comparison statistics for  $M_3$  (the  $\gamma_2$  value corresponding to the best-fit  $\theta$  is quoted to facilitate comparison with other models). There is a mild preference for this model over a single power law model for the 64 ms data (the Bayes factor is 4.7). There is a more significant, although not decisive, preference for this model for the 1024 ms data. Furthermore, the best-fit value of  $\theta$  is 1.5, the highest value we considered. The 1024 ms data fall off significantly more quickly at large fluxes than is expected for a  $\gamma = -2.5$  powerlaw, and the cutoff is quite sharp. We discuss some possible effects that could give rise to such an apparent cutoff in the 1024 ms data, but not in the 64 ms data, in § 6.

Finally, we note that our ability to detect changes in the logarithmic slope of the 1024 ms data are not simply due to the 1024 ms data set being larger and extending to lower fluxes than the 64 ms data set. If we raise the threshold for the 1024 ms detection efficiency from 0.4 to  $1.5 \text{ cm}^{-2} \text{ s}^{-1}$ , only 156 bursts remain in the data set (much less than the 279 in the 64 ms data set). Yet evidence for structure remains. Although we have not performed a full Bayesian analysis, the the maximum likelihood ratio in favor of  $M_2$  is 6.4, corresponding to 5% significance (only suggestive evidence for a break to  $\gamma_2 = 2.5$ ); and the maximum likelihood ratio in favor of  $M_3$  is 138, corresponding to 0.7% significance (strong evidence for a cutoff, with  $\Phi_b = 45 \text{ cm}^{-2} \text{ s}^{-1}$  and  $\theta = 1.5$ ).

## 5. Simple Cosmological Models

We now consider simple cosmological models. To calculate  $dR/d\Phi$  from a cosmological source distribution, we must adapt equation (1) to a cosmological setting, and then integrate over direction to calculate  $dR/d\Phi$ . We provide a detailed derivation of the cosmological counterpart to equation (1) in Appendix A. The result can be written

$$\frac{dR}{d\Phi d\mathbf{n}} = \int dV(z, \mathbf{n}) \int d\Lambda (1+z)^2 \dot{n}_c(z, \Lambda) \delta[\Phi - \Phi_{\text{obs}}(z, \Lambda, \mathcal{S})]. \quad (27)$$

This equation differs from equation (11) in three respects. First, the Euclidean volume element,  $r^2 dr d\mathbf{n}$ , has been replaced by a differential whose functional dependence accounts for spacetime curvature; additionally, we choose to parameterize it in terms of redshift and direction, the redshift here playing the role of a radial coordinate. Second,  $\dot{n}(\mathbf{r}, \Lambda)$  has been replaced with  $(1+z)^2 \dot{n}_c(z, \Lambda)$ . The  $\dot{n}_c(z, \Lambda)$  function is the burst rate density per unit  $\Lambda$  per comoving volume element for bursts at a redshift of  $z$  with a maximum photon emission rate of  $\Lambda$  (hereafter the “(peak) photon number luminosity”). The  $(1+z)$  factors arise from accounting for the redshift of the burst rate per unit time, and the difference between proper volume and comoving volume. Finally, the observed flux of a burst from a source with luminosity  $\Lambda$  at redshift  $z$ ,  $\Phi_{\text{obs}}(z, \Lambda, \mathcal{S})$ , differs from its Euclidean counterpart. It is given by

$$\Phi_{\text{obs}}(z, \Lambda, \mathcal{S}) = \frac{\Lambda}{4\pi(1+z)d^2(z)} K_0(z, \mathcal{S}), \quad (28)$$

where  $d(z)$  is the proper distance (at the current epoch) to a redshift of  $z$ , and  $K_0(z, \mathcal{S})$  is a spectral correction function (similar to the optical “ $K$ -correction”) that depends on the shape of the burst spectrum through the spectral shape parameters,  $\mathcal{S}$ .

We provide a detailed derivation of equations (27) and (28) in Appendix A. Here we remark only on the features of these equations necessary for understanding the inferences we will make, and in particular on the parameters one must specify to allow calculation of equation (27).

The volume element,  $dV(z, \mathbf{n})$ , depends on the cosmology adopted. We study cosmologies with zero cosmological constant, for which  $dV(z, \mathbf{n})$  is specified by the Hubble constant,  $H_0 = 100h \text{ km s}^{-1} \text{ Mpc}^{-1}$ , and the density in terms of the critical density,  $\Omega_0$  (or alternatively the deceleration parameter,  $q_0 = \Omega_0/2$ ).

To calculate the spectral correction factor  $K_0(z, \mathcal{S})$ , we must specify the shapes of burst spectra. We presume that all bursts have a common spectral shape: a power law proportional to  $E^{-\alpha}$ . The spectral parameters,  $\mathcal{S}$ , are then the power law index  $\alpha$ , and the lower and upper limits of the burst spectrum in the rest frame of the source. The photon number luminosity,  $\Lambda$ , is the *total* luminosity across the entire spectrum (i.e., not just that in the trigger range, since the trigger range corresponds to different rest frame energy ranges for sources at different  $z$ ). In this study, we simply fix  $\alpha = 1.5$  and fix the lower and upper limits of the spectrum at 50 keV and 100 MeV; we henceforth drop the  $\mathcal{S}$  argument from  $K_0(z)$ . We chose the energy range values so

that the redshifted lower limit is always at or below the lower limit of the trigger range, and the upper limit is never redshifted into the trigger range (since no bursts have sharp breaks or cutoffs observed in this range); our results are not sensitive to these limits. This constant value of  $\alpha$  is the same assumed for the calculation of the detection efficiency in the 3B catalog. In fact, although the median spectral index for 3B bursts is  $\alpha \approx 1.5$ , the distribution of spectral indices is quite broad. Figure 9 shows a histogram of approximate spectral indices in the nominal trigger range of 50 – 300 keV, derived from the ratios of reported burst *fluences* just below and above this range (i.e., subtracting one from the fluence spectral index, since it is for the energy spectrum rather than the number spectrum). Although this is not a distribution of peak flux spectral indices (no spectral information is tabulated for peak fluxes in the 3B catalog), it does imply that bursts exhibit a wide variety of spectral slopes. We have performed analyses using several values of  $\alpha$  and verified that our conclusions are not excessively sensitive to our choice of  $\alpha$  (best-fit parameters for  $\alpha = 1$ , for example, lie inside the 68% credible region based on  $\alpha = 1.5$ ). A more rigorous analysis would use measured values of  $\alpha$  for each burst, but our analysis gives us some confidence that the simplification of treating  $\alpha$  as a constant does not significantly corrupt our findings. More worrisome is the spectral dependence of the efficiency, about which little information is available. But hopefully this dependence is weak above the fluxes where we have truncated the efficiency for our analysis. LW95 discusses incorporation of spectral information into a Bayesian analysis in some detail.

We derive the detailed forms of  $dV(z, \mathbf{n})$  and  $K_0(z, \mathcal{S})$  in Appendix A. Once these forms are specified, the isotropy of cosmological models makes integration over  $d\mathbf{n}$  trivial, and the presence of the  $\delta$ -function in equation (27) permits us to perform one of the remaining two integrals (over  $z$  and  $\Lambda$ ) analytically. For standard candle models, for which  $\dot{n}_c$  contains a  $\delta$ -function in  $\Lambda$ , both integrals are analytic. More details about computational methods appear in Appendix A.

The models we investigate differ with respect to the choice of functional form for the comoving burst rate density,  $\dot{n}_c(z, \Lambda)$ . We always use the total burst rate per comoving volume at  $z = 0$ , denoted by  $\dot{n}_0$ , as the amplitude parameter. The shape parameters of the models are the parameters defining the  $z$  and  $\Lambda$  dependence of  $\dot{n}_c$ , and  $\Omega_0$ . Hubble’s constant appears as a scale factor in the inferred luminosity and in the amplitude parameter. Since its value is highly uncertain, we can only infer  $h^{-3}\dot{n}_0$ , and the product of luminosity and  $h^2$ . For simplicity, we adopt  $h = 1$  below.

### 5.1. Homogeneous Standard Candle Models

First we consider a standard candle model,  $M_4$ , with a comoving burst rate that is independent of redshift;

$$\dot{n}_c(z, \Lambda) = \dot{n}_0 \delta(\Lambda - \Lambda_c). \tag{29}$$

The shape parameters for this model are  $\Omega_0$  and the standard candle luminosity  $\Lambda_c$ . The luminosity is most conveniently written in terms of a dimensionless photon number luminosity,  $\nu_c$ , according to

$$\Lambda_c = \nu_c \frac{4\pi c^2}{H_0^2 K_0(0)} \Phi_{\text{fid}}, \quad (30)$$

where  $\Phi_{\text{fid}}$  is a fiducial value of the observed flux, which we set equal to  $1 \text{ cm}^{-2}\text{s}^{-1}$  (near the triggering threshold for BATSE). For  $H_0 = 100 \text{ km s}^{-1} \text{ Mpc}^{-1}$  and the spectral parameters given above,  $\nu_c = 1$  implies  $\Lambda_c = 2.2 \times 10^{57} \text{ s}^{-1}$ . Since our assumed spectrum has a mean rest frame photon energy of 2.2 MeV, this corresponds to an energy luminosity of  $L_c = 7.5 \times 10^{51} \text{ erg s}^{-1}$ . The inferred values of  $\Lambda_c$  and  $L_c$  depend more sensitively on our spectral assumptions than does the inferred value of  $\nu_c$ , since the latter is defined with respect to the part of the spectrum in the trigger passband while the former involve integrals over the entire spectrum.

For a flat universe ( $\Omega_0 = 1$ ), Figure 10 shows the marginal posteriors for the photon luminosity resulting from consideration of the 64 ms (solid curve) and 1024 ms (dashed curve) data. Properties of the best-fit models appear in Tabel 2. For the 64 ms data, the best-fit value is  $\nu_c = 0.37$ , with  $\nu_c = 0.1$  to 1 at the 95% level; the best-fit model has a likelihood 4.5 times *smaller* than that of the single power law model. For the 1024 ms data, the best-fit value is  $\nu_c = 0.44$ , with  $\nu_c = 0.2$  to 0.8 at the 95% level; the maximum likelihood is 7.2 times larger than that of the single power law model (only a fraction of the improvement offered by the smooth broken power law model). Figure 11 shows the shape of the flux distributions of the best-fit models.

Figure 12 shows contours of the joint posterior for  $\dot{n}_0$  and  $\nu_c$ . The upper contours are from analysis of the 64 ms data; the lower are from analysis of the 1024 ms data. The inferred burst rate density and luminosity are very strongly correlated in the sense one would expect: the burst rate density must be higher for models with less luminous (i.e., closer) bursts. But the inferred rate falls more slowly with luminosity than the  $\dot{n} \propto \nu_c^{-3/2}$  behavior one would expect in Euclidean space due to cosmological effects. Figure 12 also makes it clear that the two data sets imply significantly different burst rates. Since their implied luminosities are similar, this is due simply to the fact observed in § 3.3: the 1024 ms catalog has far fewer bursts in the flux range where it overlaps the 64 ms catalog.

In Appendix A we describe how to calculate the redshift distribution of burst sources once the parameters of a model are fully specified. Figure 13 shows the burster redshift distributions for the best-fit models. The solid curves show the intrinsic distribution of sources (top curve for 64 ms, bottom for 1024 ms). The dashed curves, corresponding to the right vertical axis, show the observable redshift distribution (the cutoffs at large  $z$  are due to the rapidly vanishing efficiency for detecting weak bursts). The best-fit parameter values from both data sets imply typical burst redshifts  $z \approx 1$ , although the typical redshifts of *observed* 1024 ms bursts is about twice that of 64 ms bursts.

The calculations just discussed presumed  $\Omega_0 = 1$ . Allowing  $\Omega_0$  to vary, however, broadens the allowed range of  $\nu_c$ , as shown by the joint posterior for  $\nu_c$  and  $\Omega_0$ , based on the 64 ms data,

shown in Figure 14a. Figure 14b shows that similar results arise from analysis of the 1024 ms data. Although in principle we could hope to infer the cosmological parameter  $\Omega_0$  from the burst data, these Figures show that this hope is forlorn; the posterior is very broad, spanning the range  $\Omega_0 \approx 0.1$  to 2 (i.e., the range we would have considered reasonable a priori). In practice, the data are thus too sparse to usefully constrain  $\Omega_0$ . This being the case, and since the inferred value of  $\nu_c$  is not strongly correlated with  $\Omega_0$  (the contours are nearly vertical), we concentrate on flat cosmologies ( $\Omega_0 = 1$ ) in the remainder of this paper. Allowing  $\Omega_0$  to vary will somewhat broaden posteriors based on  $\Omega_0 = 1$ .

## 5.2. Standard Candle Models With Density Evolution

Next we consider a standard candle model with power-law density evolution,  $M_5$ , for which

$$\dot{n}_c(z, \Lambda) = \dot{n}_0 (1+z)^{-\beta} \delta(\Lambda - \Lambda_c). \quad (31)$$

The shape parameters are now  $\Omega_0$ ,  $\Lambda_c$ , and  $\beta$ . As before, we replace  $\Lambda_c$  with the dimensionless luminosity  $\nu_c$ . The homogeneous model studied above corresponds to  $\beta = 0$ .

For a flat universe, Figure 15 shows joint credible regions for  $\beta$  and  $\nu_c$  for each data set; the best-fit values are listed in Tabel 2. Note that the 95% credible regions include  $\beta = 0$  models for both data sets. These are the homogeneous standard candle models considered above (model  $M_4$ ). This implies that models with density evolution are not significantly more probable than homogeneous models. This is also borne out by model comparison calculations, as revealed by the Bayes factors and likelihood ratios listed for this model in Tabel 2, none of which significantly favor models with density evolution over homogeneous models. Figure 16 shows the cumulative flux distributions of the best-fit models.

Although allowing density evolution does not significantly improve the fit to the data, it greatly weakens the ability of the data to constrain the burst luminosity: the allowed range of  $\nu_c$  now spans over four decades.

We can easily understand the shape of the credible regions plotted in Figure 15 by analysis of the behavior of  $dR/d\Phi$ . Large values of  $\beta$  are associated with small values of  $\nu_c$  because when  $\beta$  is large, most burst sources are nearby (with  $z \lesssim \beta^{-1}$ ) and therefore must have small luminosities to be able to account for the observed bursts. This part of parameter space has low probability because the observable bursts are close enough that they may be considered to be a homogeneous Euclidean population for which  $dR/d\Phi \propto \Phi^{-5/2}$ , which we know is ruled out from our analysis of power law models. On the other hand, negative values of  $\beta$  are paired with large values of  $\nu_c$  because for these  $\beta$  values, most sources are at large redshifts and thus must be highly luminous in order to be observed. In Appendix B, we show that in this regime,  $dR/d\Phi \propto \Phi^{2\beta/3}$  (for an  $E^{-3/2}$  burst spectrum). Since we know that the logarithmic slope of the flux distribution is  $\approx -2$ , such models can fit only if  $\beta \approx -3$ . This is just where the ridge of high probability is located in Figure

15.

Figure 17 shows contours of the joint posterior density for  $\dot{n}_0$  and  $\nu_c$ , conditional on  $\beta = -2.5$ , to illustrate the behavior of the posterior for the burst rate density in the vicinity of the most probable value of  $\beta$ . We emphasize that this figure is *conditional* on  $\beta = -2.5$  and is not the marginal distribution for  $\dot{n}_0$  and  $\nu_c$ , which one could calculate by averaging many such conditional distributions (with different values of  $\beta$ ). In particular, the best-fit  $(\nu_c, \dot{n}_0)$  points do not lie in the contours because the conditional density varies strongly with  $\beta$ . However, the conditional density better illustrates the discrepancy between inferences based on the two data sets. As with homogeneous standard candle models, the two data sets imply significantly different burst rate densities, and there is a strong correlation between inferred values of the burst rate density and luminosity. But compared to the homogeneous case, allowing for density evolution significantly increases our uncertainty about the burst rate density, so that even for the 1024 ms data, the 95% credible region spans nearly two orders of magnitude in  $\dot{n}_0$  (it is presumably larger for the marginal distribution).

The large uncertainty in burster luminosity implied by models with density evolution leads to a large uncertainty in burster redshifts. Figure 18 shows the burster redshift distribution for some representative models that lie in the 95% credible regions for  $\beta$  and  $\nu_c$  for both data sets (with parameter values corresponding to the dots in Figure 15). For positive values of  $\beta$ , the observed bursts have typical redshifts  $\lesssim 0.5$ ; but for negative values of  $\beta$ , the observed bursts could extend to redshifts of 30.

Models with large burst source luminosities and redshifts are allowed only because the data are insufficient to constrain the logarithmic slope of distribution of bright bursts to the  $-5/2$  value expected for bursts originating from redshifts  $\lesssim 1$ . Including data from the burst detector on the Pioneer Venus Orbiter (PVO) is likely to strengthen the constraint, since the flux distribution of PVO bursts is consistent with  $dR/d\Phi \propto \Phi^{-5/2}$ . A preliminary joint analysis of BATSE and PVO data by Fenimore and Bloom (1996a, b) indicates that the PVO data imply that the dimmest observed bursts must have redshifts  $z < 6$ . Cohen and Piran (1995) supplemented the BATSE data with a set of burst fluxes comparable in size to those observed by PVO, and drawn randomly from a  $\Phi^{-5/2}$  distribution. Their calculation seems to verify that such data can improve constraints on the redshifts of the dimmest bursts, but their analysis is only illustrative, since it presumes that the entire PVO catalog samples the  $\Phi^{-5/2}$  part of the flux distribution.

We expect that allowing  $\Omega_0$  to vary would further weaken the constraints on the burster luminosity, although we have not explored the resulting higher dimensioned parameter space. We do not expect introduction of  $\Omega_0$  to affect the allowed luminosity range as drastically as does introduction of  $\beta$ .

### 5.3. Models With Power-Law Luminosity Functions

Finally, we consider a model with no density evolution, but with a power-law photon number luminosity function. For this model,  $M_6$ , we set

$$\dot{n}_c(z, \Lambda) = \dot{n}_0 A \Lambda^{-p} \quad (32)$$

over a finite range,  $\Lambda_l$  to  $\Lambda_u$ . The parameter  $A$  is a normalization constant for the  $\Lambda$  power law whose value is fixed by the other parameters. The shape parameters for  $M_5$  are thus  $\Omega_0$ ,  $p$ ,  $\Lambda_u$ , and the dynamic range,  $\rho = \Lambda_u/\Lambda_l$ . As shown by Wasserman (1992), the luminosity function allows the distribution to flatten from a power law with index 5/2 at large  $\Phi$  to one with index  $p$  at low  $\Phi$ , improving the fit in much the same manner as the smooth broken power law model  $M_2$  (see also Mészáros and Mészáros 1995). Solar flares, which have similar temporal properties to bursts, have power law distributions of peak intensity and fluence (Dennis 1985); such power law distributions are general features of phenomena that involve energy transfer via a cascade over a broad range of spatiotemporal scales (Bak, Tant, and Wiesenfeld 1988; Press 1978; Lu and Hamilton 1991). In addition, relativistic beaming can produce power law luminosity functions with a finite dynamic range, as we discuss in § 7. Thus power law distributions are natural and obvious candidates for burst source luminosity functions.

As with the previous model, we analyze only the flat,  $\Omega_0 = 1$  case; this leaves three shape parameters. In Figure 19 we show the profile posteriors for  $\rho$  based on each data set, that is, the posteriors maximized with respect to  $\Lambda_u$  and  $p$  as a function of  $\rho$ . These curves can be considered to be approximate marginal distributions for  $\rho$ . We have normalized them so that values of unity correspond to likelihoods equal to the maximum likelihood found for homogeneous standard candle models. If  $\rho$  is smaller than the dynamic range of the data ( $\sim 10^2$ ), the luminosity function has negligible width, and these models resemble homogeneous standard candle models and thus have profile posteriors equal to unity with this normalization. As  $\rho$  increases, the profile posterior increases indicating that a broad luminosity function improves the fit. Once  $\rho$  significantly exceeds the dynamic range of the data, the profile posterior varies very weakly with  $\rho$ . This indicates that the data cannot constrain the width of a power law luminosity function. Accordingly, we simply fix  $\rho$  at a large value ( $10^4$ ) to explore this model, rather than incur the computational and graphical burden of keeping this unconstrained parameter in the parameter space. We discuss the absence of a constraint on the luminosity function width further below.

With  $\Omega_0$  and  $\rho$  fixed, two shape parameters remain,  $p$  and  $\Lambda_u$ . As with standard candle models, we write  $\Lambda_u$  in terms of a dimensionless parameter,  $\nu_u$ , so that

$$\Lambda_u = \nu_u \frac{4\pi c^2}{H_0^2 K_0(0)} \Phi_{\text{fid}}. \quad (33)$$

Figure 20 shows contours of the joint posteriors for  $p$  and  $\nu_u$ , and Figure 21 shows the best-fit models. The best-fit parameter values appear in Table 2, with the Bayes factors and likelihood ratios for the models. For the 64 ms data, the best-fit point is at  $p = 2.0$ ,  $\nu_u = 23.6$ ; but  $\nu_u$  is

largely unconstrained over a dynamic range of the order of  $\rho$  (here equal to  $10^4$ ). Although the best-fit power law index and upper luminosity limit are notably different for the 1024 ms data, they, too, imply a broad posterior distribution that has significant overlap with that based on 64 ms data.

The peculiar shape of the contours is easy to understand. For large negative values of  $p$ , the luminosity function is highly concentrated in the vicinity of  $\Lambda_u$ , and the model thus has the likelihood of a homogeneous standard candle model with  $\nu_c = \nu_u$ , independent of the value of  $p$ . Thus the contours become vertical at a value of  $\nu_u$  near the credible range of  $\nu_c$  found earlier for homogeneous standard candle models. Similarly, for large positive values of  $p$ , the luminosity function is highly concentrated in the vicinity of  $\Lambda_l = \Lambda_u/\rho$ , leading to a likelihood equal to that of a homogeneous standard candle model with  $\nu_c = \nu_u/\rho$ . Thus the contours become vertical at  $\nu_u$  values that are a factor of  $\rho$  times the credible range of  $\nu_c$  values found for homogeneous standard candle models. In between these limiting regimes, there is a nearly horizontal ridge of high probability for models with  $p$  nearly equal to the value of the low flux power law index,  $\gamma_1$ , of the phenomenological smooth broken power law model. This is because, as noted in § 4, when there is a spatial scale (here  $c/H_0$ ) and a power-law luminosity function (with  $1 < p < 5/2$ ), the flux distribution will have the same logarithmic slope as the luminosity function below some flux value.

For both data sets, the 95% contours fail to close at the large  $\nu_u$ , large positive  $p$  end, or at the small  $\nu_u$ , large negative  $p$  end. This indicates that this model does not greatly improve upon the standard candle model. This is also clear from Figure 19, where it is apparent that the likelihood for power law models is at most nine times that of standard candle models. This modest increase in likelihood is insufficient to justify the larger parameter space of these models. Indeed, the model comparison results in Table 2 indicate no significant preference for models with power law luminosity functions over homogeneous standard candle models.

Figure 22 shows contours of the joint posterior density for  $\dot{n}_0$  and  $\nu_u$ , conditional on  $p = 1.9$ , to illustrate the behavior of the posterior for the burst rate density near the most probable value of  $p$ . As was true with models incorporating density evolution (see Figure 17), the additional degree of freedom associated with the luminosity function significantly increases our uncertainty about the burst rate density; the 95% credible region again spans orders of magnitude. As with the previously studied cosmological models, the two data sets imply significantly different burst rate densities.

Figure 23 shows burster redshift distributions for some representative models in the 95% credible regions. Although the inferred luminosity of the brightest bursters varies strongly across the credible regions, the redshift distributions do not vary as strongly; the observed bursters always have redshifts of a few tenths, and the characteristic redshift of the intrinsic distribution is of order a few. We elucidate the reasons for this behavior below.

### 5.3.1. Width of the Luminosity Function

A number of earlier investigations claim that the BATSE data constrain the width of the luminosity function to be relatively narrow, with most studies finding that the dynamic range must be  $\lesssim 10$  (Horack, Emslie, and Meegan 1994; Cohen and Piran 1995; Woods and Loeb 1995; Ulmer and Wijers 1995; Ulmer, Wijers, and Fenimore 1995), and a recent study finding instead that it is constrained to  $\lesssim 10^3$  (Hakkila et al. 1996). This is a surprising result in light of the wide diversity evident in other burst characteristics (e.g., burst durations span several orders of magnitude). If true, this would be an important conclusion, potentially offering important constraints on physical scenarios for bursts. For example, the high luminosities required in scenarios that place burst sources at cosmological distances makes it likely that the emitting material is accelerated to relativistic velocities. Due to relativistic beaming, an isotropically emitting “blob” with a particular rest frame luminosity will have an apparent luminosity that varies strongly with the angle between the observer and the velocity vector. Thus even if sources were standard candles in their own rest frame, the distribution of observing angles gives rise to an apparent luminosity function. We show in § 7 that the resulting luminosity function is a bounded power law spanning a range of luminosities differing by a factor of  $\approx (2\gamma)^{2\alpha+4}$ , where  $\gamma$  is the Lorentz factor and  $\alpha$  is the spectral index (typically  $1.5 \pm 1$ ). In this scenario, even with very modest Lorentz factors, one thus expects the luminosity function to have a large dynamic range ( $> 10^4$  for  $\gamma = 2$ ). Evidence that the luminosity function is narrow would thus place strong constraints on relativistic motion in such a scenario.

Our results differ from those of previous studies, instead demonstrating that the BATSE 3B data cannot constrain the width of power-law luminosity functions. This important difference requires explanation. Before examining some specific ways that our work improves on previous studies, we offer some further calculations that clarify why broad luminosity functions are compatible with the 3B data.

One might worry that our broad luminosity functions are *effectively* narrow, because the best-fit models have luminosity functions that fall fairly quickly with luminosity. Although they extend to large luminosities, the bright bursts are rare and perhaps can be considered to be effectively absent from observations spanning only four years. To address this, we explored the power law luminosity function model with  $p = 0$ , so the luminosity function becomes a flat “top hat” function. Figure 24 shows the profile likelihood function for the dynamic range spanned by the “top hat;” for each value of  $\rho$ , we maximized the likelihood with respect to  $\nu_u$  to get the plotted function. The profile likelihoods based on both the 64 ms and 1024 ms data are nearly flat, showing that even the width of a *flat* luminosity function cannot be constrained.

Figure 25 elucidates the reason the data cannot constrain the width of the luminosity function. Shown are the differential burst rates for models with “top hat” luminosity functions with three different dynamic ranges:  $\rho = 1$  (standard candles), 2, and  $10^4$ , with  $\nu_c$  and  $\dot{n}_0$  set at their best-fit values based on the 1024 ms data. We have plotted the rates over a much broader range of flux

values than that spanned by the data. In all three cases, the best-fit value of  $\nu_u$  is of order unity. This implies that the break from  $dR/d\Phi \propto \Phi^{-2.5}$  to  $dR/d\Phi \propto \Phi^{-p}$  will take place in the vicinity of  $\Phi = 1 \text{ s}^{-1} \text{ cm}^{-2}$ , as is evident in the figure. The extent of the luminosity function affects the behavior of the rate below this value; but the useful data extend only to  $\Phi \approx 0.4 \text{ s}^{-1} \text{ cm}^{-2}$ . There is simply no data in the region where rates from populations with different values of  $\rho$  distinguish themselves.

As already noted, our conclusion that the data cannot constrain the width of the luminosity function for cosmological burst sources differs strongly from the findings of earlier studies. In § 10 of paper I we discussed a variety of ways that our methodology improves on that of earlier studies. Some of these improvements are especially apparent in the analysis of the width of the burster luminosity function; we elaborate on them here.

An important and general advantage of Bayesian methods over more traditional frequentist methods is the objectivity of the Bayesian approach. Ironically, Bayesian methods have the reputation of being subjective because of the presence of explicit prior probabilities in Bayesian calculations. Although in some problems objective priors exist from analyses of previous measurements, in cases where we start from “ignorance,” the need for a prior does impart subjectivity to the final result. It is tempting to adopt some simple form for an “ignorance prior,” such as a flat prior, but subjectivity arises because adopting a flat prior in a problem with a parameter  $\theta$  does not produce the same results as adopting a flat prior in the same problem, reparameterized with  $\theta' = \theta^2$ , say. But in practice, if the data provide significant new information about a phenomenon, the choice of prior has a negligible effect on one’s final inferences. Indeed, if the final results change significantly due to a small change of the prior (or of the parameterization), one has quantitatively demonstrated that the data are not informative—surely a useful capability. Further, traditional frequentist methods are not free of the subjectivity that arises from the choice of parameterization of a problem. For example, an unbiased estimator for  $\theta$  will not in general be an unbiased estimator for  $\theta' = \theta^2$ .

More importantly, Bayesian methods are far *more* objective than their frequentist counterparts in terms of specifying how the data should affect inferences. Bayes’s theorem uniquely identifies the likelihood function as the relevant function of the data, and the rules of probability theory dictate uniquely and mechanically how to manipulate it to make inferences. In frequentist statistics there is considerable freedom in choosing the statistic one will use to address a particular problem; in complicated problems different analysts studying the same model are likely to make different choices and can reach significantly different conclusions as a result. Even when the likelihood function is used (e.g., in maximum likelihood parameter estimation), considerable freedom remains regarding how to use it to make inferences (particularly if there are nuisance parameters present). Bayesian and frequentist analyses using likelihoods can produce different results, as we discussed at length in § 9 of paper I.

This point of contrast between Bayesian and frequentist approaches is evident in analyses

of the BATSE data. A variety of statistics have been used to study the same or similar models. For example, studies of isotropic models have used various estimates and summaries of the  $V/V_{\max}$  distribution,  $\chi^2$  fitting of binned flux data, the Kolmogorov-Smirnov statistic, and various moments of the observed intensity distribution. Besides the possibility of differing studies reaching different conclusions, difficulties also arise if one examines several statistics in the course of a study, choosing one as being “best” a posteriori. Such difficulties arise in assessing the work of Horack, Emslie, and Meegan (1994), one of the several studies claiming that the BATSE data require a luminosity function with a dynamic range less than 10. Their study used relationships among various integral moments of the best-fit peak fluxes to constrain the luminosity function. They examined many such relationships before choosing one that provided a strong constraint, but their calculation of the significance of their result did not account for the number of statistics they examined. Such an accounting will weaken their constraint; possibly seriously. In any case, as we noted in LW95, the Pitman-Koopman theorem (Jeffreys 1961) guarantees that if there is a set of averages or moments of the data that contain all the information relevant to assessing the considered hypothesis, then the likelihood will depend only on those averages, and they can be identified by examining its functional form. No set of such averages appears in our likelihood function, so any calculation considering only a few ad hoc moments of the data is discarding relevant information that the likelihood function takes into account.

A further advantage of our methodology is that it straightforwardly accounts for the uncertainty in the measured parameters of bursts (e.g., their peak flux and direction). This is a stumbling block for frequentist studies because such parameters are technically “nuisance parameters,” and there is no satisfactory method for handling nuisance parameters in frequentist statistics. In the Bayesian approach, one simply uses Bayes’s theorem to move them to the left of the conditional, and then integrates them out of the problem. In analyses of isotropic models, the relevant uncertainties are the peak flux uncertainties. No previous study has rigorously accounted for them. The study of Horack, Emslie, and Meegan (1994) attempted to account for them in an ad hoc manner, but they performed no studies of simulated data to verify or calibrate their procedure. All other studies ignore the uncertainties, implicitly assuming that the best-fit peak flux is the true peak flux.

Most studies analyzing the peak flux data use the 1024 ms data, for which the peak flux uncertainty is relatively small—at most  $\sim 15\%$  for the dimmest bursts, compared to  $\sim 25\%$  for the 64 ms data. The 1024 ms peak flux uncertainties may be small enough to ignore (although we demonstrate below that the distribution of 1024 ms peak fluxes is likely to be less suitable for analysis than the 64 ms data for other reasons). However, two studies (Cohen and Piran 1995; Ulmer and Wijers 1995) instead analyzed the distribution of peak *count rates* (with units of  $\text{s}^{-1}$ ) rather than peak fluxes (with units of  $\text{s}^{-1} \text{cm}^{-2}$ ). The reported peak count rates are the peak rates in the second most brightly illuminated detector. To compare them with burst distribution models, one must convert from incident fluxes (the quantity one can predict with a burster distribution model) to count rates, taking into account the highly uncertain angle of incidence to

the second most brightly illuminated detector. The resulting uncertainty in the peak flux is *not* negligible; the uncertainty in angle imparts a  $\approx 16\%$  uncertainty to the fluxes of *all bursts*, to which must be added (in quadrature) the additional uncertainty due to counting statistics (which can be relatively large since the counts in only a single detector are used). But this uncertainty was ignored in both studies (both studies use equations that incorrectly equate peak count rates with peak fluxes, despite the dimensional inconsistency). In our earlier work (Loredo and Wasserman 1993) we discussed proper fitting of the 1B peak count rate data; our analysis found no constraint on the dynamic range of the luminosity function. More importantly, since the release of the 1B catalog in 1993 (Fishman et al. 1994), burst peak fluxes have been available for analysis. The peak flux estimates not only incorporate burst direction information; they also take into account the burst spectrum in the conversion from count rates to fluxes. They are thus far superior to the peak counts data provided prior to the 1B catalog, and are the basis of our analysis here.

A further advantage of the Bayesian approach is that it produces very straightforward inferences: one calculates directly the probabilities for the hypotheses under consideration. To constrain parameters, one simply plots contours of (possibly multidimensional) posterior distributions. When parameters are highly correlated, this is evident in plots of the joint distribution; and even when inferences are summarized for a subset of the parameters (via marginalization), all correlations are properly taken into account. Similarly, to compare models, one simply calculates ratios of the probabilities for competing models.

In the frequentist approach, one instead calculates values of the chosen statistic, and then takes a further step of converting these to probabilities, sometimes by appealing to a simple asymptotic limit, or often by using Monte Carlo simulations. A subtlety arises in that one must assume a particular model is true with a particular set of parameters in order to perform the probability calculation, but the resulting probability may be interpreted as applying to a region of parameter space (in calculating confidence regions), or to a space of models (in calculating significances of goodness-of-fit tests). This complicated and indirect line of reasoning has led to shortcomings in several studies of the BATSE data. For example, Woods and Loeb (1995) found their constraints on the width of a “log-normal” luminosity function (not of the standard lognormal form) by fixing the parameter specifying the most probable luminosity to its best-fit value, and varying only the width. For the power-law models we studied, this would correspond to fixing  $\nu_u$ , and varying only  $\rho$  (for a particular  $p$ ). This strongly and artificially constrains the dynamic range, because models with a large dynamic range are permitted only when we shift the bulk of the luminosity function to low fluxes, so that only the brightest bursts are visible from redshifts of order unity. This problem is evident in our approach because Bayes’s theorem gives us no alternative but to begin our calculation by studying the full joint posterior, which displays all correlations.

In addition, Woods and Loeb confused the roles of the probabilities that appear in goodness-of-fit tests with those that appear in calculating confidence regions: they used the significance level assigned by a goodness-of-fit test to define allowed parameter regions, when

instead a confidence interval should have been calculated. Several other investigators have made this same error, particularly in regard to analyses of anisotropic models. We thus discuss it in detail in Appendix A of Paper III. Such confusion cannot arise in the Bayesian approach because one is always explicitly calculating probabilities for the hypotheses of interest (statements about parameter values for credible region calculations; statements about models in model comparison calculations), rather than calculating probabilities for ensembles of data conditional on a single point hypothesis that may actually be representing an entire family of hypotheses of interest.

Finally, we went to great lengths in this work to ascertain how approximations adopted in the preparation of the 3B catalog affect one’s inferences, particularly in regard to the accuracy of the reported detection efficiency (see § 3). We found that a self-consistent analysis must omit a significant amount of low-flux data. Most other analyses of the peak flux data omitted even more low-flux bursts than we did, and thus are probably not affected by inaccuracies in the reported efficiency. An exception is the work of Hakkila et al. (1996) who analyze a combination of data from BATSE and PVO, studying the distribution of peak *energy* flux, rather than peak photon number flux. Unfortunately, they provide insufficient details to allow duplication of their analysis or elucidation of possible problems with their methods. In particular, it is not clear whether or how they took into account the detection efficiency. Their analysis includes bursts with 1024 ms peak photon fluxes down to  $0.42 \text{ cm}^{-2} \text{ s}^{-1}$ . The 3B efficiency is still varying significantly with peak flux at these low fluxes, and must be taken into account. But the 3B efficiency is available only as a function of peak photon number flux, and they offer no discussion of how it can be used to analyze the distribution of peak energy flux, and no analysis of how accurately this can be done given the approximations adopted in constructing the 3B catalog (for example, their cutoff in peak number flux almost certainly does not correspond to a simple cutoff in peak energy flux). Their study also exhibits some of the problems associated with choice of statistic and accounting for uncertainty: they analyzed a binned flux distribution but did not discuss how bin boundary selection affects their results ( $\approx 20\%$  of all bursts are in a single bin at low flux in their analysis), and their binning implicitly presumes that the fluxes are known without uncertainty. Of course, the most obvious difference between their analysis and that reported here is their inclusion of PVO data. But we do not believe PVO data play an important role in constraining the width of the luminosity function. PVO predominantly detected bright bursts, with fluxes well above the BATSE threshold; as shown in Figure 25, models with different luminosity function widths differ substantially only at *low* fluxes, near or below the BATSE threshold. It is possible that the BATSE data are capable of constraining the width of the peak energy luminosity function but not the peak photon number luminosity function; but this would require a strong correlation between spectral hardness and intensity. The differences between our findings are thus likely due to methodological differences.

### 5.3.2. Effective Luminosity Function

Our analysis so far has concerned the distribution of the luminosities of *all* burst sources (the *intrinsic* luminosity function). The distribution of the luminosities of the sources of *observed* bursts (the *effective* luminosity function) is in general different, and the difference between these functions has been confused in some analyses.

Ulmer and Wijers (1995) and Ulmer, Wijers, and Fenimore (1995) have correctly distinguished the intrinsic and effective luminosity functions. Unfortunately, the former study incorrectly analyzed the BATSE peak count rates, treating them as peak photon number fluxes as we discussed above. The latter study combined BATSE data from two timescales (256 ms and 1024 ms) with PVO data and found that 90% of observed bursts have peak luminosities within a range of 10. We show below that our results imply effective luminosity functions that can span a much larger range. The brief report of Ulmer, Wijers and Fenimore (1995) does not provide sufficient detail for us to ascertain the origin of our differing conclusions.

Other analyses recognize that the intrinsic and effective luminosity functions are different, but go on to presume that the luminosity function of observed sources is simply the 90% most probable part of the intrinsic luminosity function (Horack, Emslie, and Meegan 1994; Hakkila et al. 1996; Horack et al. 1996). These studies also conclude that the effective luminosity function must span a dynamic range  $< 10$ . Indeed, our best-fit *intrinsic* luminosity functions fall quickly enough with  $\Lambda$  that the 90% most probable portion spans a range  $\sim 10$ . However, the effective luminosity function has a different, flatter shape than does the intrinsic luminosity function, giving it a much larger 90% range.

In § 4 of Appendix A we derive the effective luminosity function for cosmological sources. But the most important differences between intrinsic and effective luminosity functions are apparent in the simpler Euclidean case we now discuss. Consider a population of sources with burst rate per unit volume  $\dot{n}(r)$  and intrinsic luminosity function  $f(\Lambda)$ . The effective burst rate per unit peak flux is found by multiplying equation (11) by the detection efficiency. The effective burst rate per unit luminosity is found simply by exchanging the roles of  $\Phi$  and  $\Lambda$ . The resulting integral over  $\Phi$  is analytic, giving

$$\frac{dR_{\text{eff}}}{d\Lambda} = f(\Lambda) \int_0^\infty dr 4\pi r^2 \dot{n}(r) \bar{\eta}' \left( \frac{\Lambda}{4\pi r^2} \right). \quad (34)$$

This is the effective luminosity function, up to a factor converting the normalized effective luminosity function into the effective burst rate calculated here. If all bursts are detectable, then  $\bar{\eta}' = 1$  and the integral over  $r$  is simply a constant equal to the total burst rate. In this case, the effective luminosity function has the same shape as the intrinsic luminosity function. But selection effects can cause the shapes to differ drastically in more realistic situations. For example, if bursts are detectable only if their peak flux exceeds a threshold value  $\Phi_{\text{th}}$ , then the integral over  $r$  above is truncated to  $r < (\Lambda/4\pi\Phi_{\text{th}})^{1/2}$ , and is no longer a constant; its functional form will depend on

the burst rate density. If  $\dot{n}(r) \propto r^\delta$ , then

$$\frac{dR_{\text{eff}}}{d\Phi\Lambda} \propto f(\Lambda)\Lambda^{\delta+3/2}. \quad (35)$$

It is apparent that even simple truncation can produce an effective luminosity function drastically different in shape from  $f(\Lambda)$ , with the tendency being toward increasing the probability for seeing luminous burst sources (if  $\delta > -3/2$ ).

Horack et al. (1996) recognized that the effective and intrinsic luminosity functions could differ in shape, but never actually calculated the effective luminosity function. They maintained that the difference was inconsequential because only burst rate densities that increased with  $r$  could make bright bursts appear significantly more probable than is implied by the best-fit  $\Lambda^{-2}$  intrinsic luminosity functions. However, their argument ignores the increase with  $r$  of the volume element. The probability for seeing luminous burst sources can be enhanced even for rate densities that fall with  $r$ , simply because the volume at large  $r$  is large enough that it is likely that rare, luminous bursts actually occur within the sample volume.

In Figure 26 we show the effective luminosity functions for the best-fit models for the 64 ms and 1024 ms data; also shown are the logarithmic slopes of the functions (these calculations use the full cosmological expression). The effective luminosity functions are significantly flatter than the intrinsic functions (which have logarithmic slopes  $\approx 2$ ). The dots indicate the luminosities bounding the 90% most probable luminosities. The 90% ranges span over three orders of magnitude. Figure 27 shows the effective luminosity function for the best-fit 1024 ms model, along with functions corresponding to two other models lying in the 68% credible region shown in Figure 20(b) that have luminosity upper limits  $\nu_u$  significantly smaller and larger than the best-fit value. Again, dots indicate the boundaries of regions containing the 90% most probable luminosities. It is clear that the shape of the effective luminosity function is not well-determined; the sign of its slope is not even determined. The sizes of the 90% regions are very large, spanning two to three orders of magnitude. Interestingly, although the three curves correspond to  $\nu_u$  values spanning a factor of 400, the upper limits of the 90% regions differ by only a factor of 3, and the 90% regions overlap substantially. Thus although widely disparate values the luminosity of the most luminous sources are allowed by the data, the luminosity of the most luminous *observed* sources is constrained to be of order  $\nu \sim 0.1$  to 1.

Note that the 90% ranges are larger than the ranges of best-fit peak fluxes in the data sets we have analyzed. Geometry is to blame for this somewhat counterintuitive result. Underluminous bursters are visible only nearby, in a volume small enough that few if any luminous bursts occur during the duration of the observations. But luminous bursters are visible through a much larger volume, large enough that a significant number occur at large distances (and hence at relatively low fluxes) during the observation time. In this way burst sources with very disparate luminosities are sampled from differing depths such that their observed fluxes span a range smaller than is spanned by the luminosities.

## 6. A Phenomenological Model With Duration Dependence

As we have seen time after time, inferences based on an analysis of the 64 ms data are somewhat different from those based on analysis of the 1024 ms data. The complicated nature of the dependence of these data sets on one another makes it difficult if not impossible to assess the significance of the discrepancy quantitatively, and also to determine the extent to which the discrepancy is merely a consequence of the different sizes of the data sets. Nevertheless, even the simplest phenomenological models we have studied indicate that there are important systematic differences between the data sets. This conclusion is supported by the fact, alluded to above, that analyses of the 256 ms data always lead to inferences intermediate to those found with the 64 ms and 1024 ms data.

This leads us to conclude that explicit consideration of the temporal behavior of bursts is necessary for understanding the flux distribution, a possibility we discussed at some length in LW95. This finding is somewhat ironic in view of the fact that the the gamma ray burst community moved from quantifying burst intensity with fluences to peak energy fluxes and finally to peak photon number fluxes in an effort to avoid the effects of differing burst light curves and spectra on the shape of the intensity distribution. But as we emphasized in LW95, use of peak photon number flux may weaken, but cannot eliminate, the effects of differing burst light curves and spectra on the shape of the distribution of measured fluxes.

To see how the temporal properties of bursts can affect the observed flux distributions, consider a “top hat” model for burst light curves that presumes the burst emission maintains its peak value over some time scale,  $\tau$ , and is significantly smaller for times outside of the peak. Denote the actual peak flux by  $\Phi_a$ . If  $\tau$  is longer than the trigger time scale  $\delta t$ , a somewhat subtle *peak counts bias* results in overestimation of  $\Phi_a$ , if one does not carefully account for the peak duration. This is because one is taking several independent samples of counts during the peak, and is thus likely to identify an upward fluctuation in the counts as the peak. We analyzed this bias in detail in LW95, and pointed out that since its size depends nonlinearly on  $\Phi_a$ , it can distort the shape of the observed flux distribution. Interestingly, the peak counts bias causes the the observed distribution to steepen as  $\delta t$  is decreased (provided  $\delta t < \tau$ ). Thus it is possible that some of the steepening of the 64 ms peak flux distribution relative to the 1024 ms distribution (at low flux values) is due to this effect. Lamb, Graziani, and Smith (1993) discuss the effects of peak counts bias on burst classification.

On the other hand, if  $\tau < \delta t$ , *peak dilution* results. If one does not account for the fact that the peak is narrower than the measuring interval,  $\Phi_a$  can be underestimated by a factor as small as  $\tau/\delta t$ . If peak duration is not correlated with peak flux, this dilution simply shifts the entire flux distribution downward without altering its shape (but possibly broadening it if there is a distribution of peak durations). But if peak duration and peak flux are correlated, peak dilution can easily distort the shape of the observed flux distribution. Some of the effects of peak

dilution have been previously discussed by Lamb, Graziani, and Smith (1993), Mao, Narayan and Piran (1993), and Petrosian, Lee, and Azzam (1994). The fact that the observed 64 ms peak flux distribution extends to about  $150 \text{ cm}^{-2} \text{ s}^{-1}$ , but the 1024 ms peak flux distribution extends only to about  $40 \text{ cm}^{-2} \text{ s}^{-1}$  could be taken as evidence that peak dilution is important in the 1024 ms data.

In LW95 we indicated some ways in which effects like peak counts bias and peak dilution could be incorporated into an analysis of the burst peak flux and direction data. We additionally discussed incorporation of spectral information. The 3B catalog provides extremely limited information about the temporal and spectral properties of bursts, and thus severely limits the possibilities for an analysis more sophisticated than that described in the previous sections. In this and the following section, we analyze two simple models that illustrate how temporal and spectral information can play a role even in an analysis of peak flux data alone. Neither model is completely successful at explaining the patterns we have uncovered in the data; but they remain useful as illustrations of the principles described in LW95. Underlying both models is the “top hat” light curve model just discussed. Although it is a highly limited caricature of the shape of actual burst light curves, it has the virtue of simplicity, and it can be analyzed approximately using only the limited information available in the 3B catalog. As part of the approximation, we neglect peak counts bias (as we have tacitly done throughout this work; no raw count data is available in the catalog), and consider only the effects of peak dilution.

We begin with a purely phenomenological model that presumes that bursts have an intrinsic time scale  $\tau$  that is a deterministic function of the actual peak flux of the bursts, which we denote by  $\Phi_a$  to distinguish it from the measured value,  $\Phi$ . That is, we take the  $\tau$  distribution to be a  $\delta$ -function whose location is a function of  $\Phi_a$ . If we let  $\tau(\Phi_a)$  denote the duration of a burst with actual flux  $\Phi_a$ , then the  $\delta t$ -averaged peak flux is

$$\Phi_{\text{eff}}(\Phi_a) = \begin{cases} \Phi_a, & \text{for } \tau(\Phi_a) \geq \delta t, \\ \Phi_a \frac{\tau(\Phi_a)}{\delta t}, & \text{for } \tau(\Phi_a) < \delta t. \end{cases} \quad (36)$$

Once  $\tau(\Phi_a)$  is specified, the observable burst flux distribution can be calculated from the actual flux distribution  $dR/d\Phi_a$  according to

$$\frac{dR}{d\Phi} = \int d\Phi_a \frac{dR}{d\Phi_a} \delta[\Phi - \Phi_{\text{eff}}(\Phi_a)]. \quad (37)$$

For our phenomenological model, we use a power law form for  $\tau(\Phi_a)$ , writing

$$\tau(\Phi_a) = \tau_0 \left( \frac{\Phi_a}{\Phi_0} \right)^{-\sigma}, \quad (38)$$

where  $\tau_0$  is the peak duration for bursts with some fiducial actual peak flux  $\Phi_0$ , and  $\sigma$  is the power law index. If  $\sigma > 0$ , bright bursts have shorter peaks than dim ones; if  $\sigma < 0$ , dim bursts have shorter peaks than bright ones. For  $\sigma > 0$ , this model can qualitatively mimic the behavior

of a simple physical model: a homogeneous standard candle distribution of bursters that are also “standard clocks.” For such a model, dim bursts must originate from larger redshifts than bright ones, and will therefore have longer observed durations. This is the same qualitative behavior as our  $\sigma > 0$  models.

To complete specification of the model, we let the actual peak flux distribution be a power law, writing

$$\frac{dR}{d\Phi_a} = A \left( \frac{\Phi_a}{\Phi_0} \right)^{-\gamma_1}. \quad (39)$$

We can now use equation (37) to calculate the observable flux distribution. For  $0 < \sigma < 1$ , the result can be written as

$$\frac{dR}{d\Phi} = A' \times \begin{cases} \left( \frac{\Phi}{\Phi_\tau} \right)^{-\gamma_1}, & \text{for } \Phi \leq \Phi_\tau, \\ \frac{1}{1-\sigma} \left( \frac{\Phi}{\Phi_\tau} \right)^{-\gamma_2}, & \text{for } \Phi > \Phi_\tau; \end{cases} \quad (40)$$

where  $\gamma_2 = (\gamma_1 - \sigma)/(1 - \sigma)$ , and  $\Phi_\tau$  is the flux where  $\tau(\Phi_a) = \delta t$ ,

$$\Phi_\tau = \Phi_0 \left( \frac{\tau_0}{\delta t} \right)^{1/\sigma}. \quad (41)$$

The observable flux distribution is thus a broken power law with a discontinuity at  $\Phi_\tau$ , where the power law index changes from its low flux value of  $\gamma_1$  (the index for the underlying actual distribution) to its high flux value of  $\gamma_2$ . The cumulative distribution is continuous.

Note that  $\Phi_\tau$  is a decreasing function of  $\delta t$  as long as  $\sigma > 0$ . In our study of smooth broken power law models above, we found that the break flux inferred from the 1024 ms data is lower than that inferred from the 64 ms data, so the positive  $\sigma$  regime is the regime of interest. Note also that

$$\gamma_2 - \gamma_1 = \frac{(\gamma_1 - 1)\sigma}{1 - \sigma}, \quad (42)$$

so that  $\gamma_2 > \gamma_1$  as long as  $\gamma_1 > 1$  and  $\sigma < 1$ . From our earlier analyses, we know  $\gamma_1 \approx 2$ ; thus for this model the flux distribution will steepen at large fluxes. This is the behavior exhibited by the data and expected for observational and theoretical reasons (the PVO data for bright bursts has a differential distribution like that expected from a homogeneous Euclidean distribution,  $\propto \Phi^{-2.5}$ ). When  $\sigma > 1$ , the distribution flattens rather than steepens if  $\gamma_1 > 0$ . Thus the  $0 < \sigma < 1$  regime described above is the only regime of interest.

This discontinuous broken power law model has three shape parameters:  $\gamma_1$ ,  $\sigma$ , and  $\tau_0$  ( $\Phi_0$  is an arbitrary fiducial flux that we set equal to  $1 \text{ cm}^{-2} \text{ s}^{-1}$ ). If the differences between the 64 ms and 1024 ms data are due to simple duration effects of the kind built into this model, then parameter estimates from each data set should agree, even though the shapes of the flux distributions in the two data sets differ. For example, Figure 28 shows the differential flux distribution for a representative choice of  $\gamma_1$ ,  $\sigma$ , and  $\tau_0$ , plotted for both time scales, illustrating that the differing values of  $\delta t$  lead to different break locations.

Table 3 lists the best-fit parameter values and model comparison statistics for this model ( $M_7$ ). For the 64 ms data, the best-fit model has a burst peak duration of  $\tau_0 = 0.16$  s, and fits the data substantially better than a single power law model without any duration dependence ( $M_1$ ), although not so much better that it justifies the additional parameters of this model. In contrast, for the 1024 ms data, the timescale is 40 s, and the improvement of the fit is substantial enough to favor this model over  $M_1$ , although not decisively.

Note that of all the models studied in this work, this simple model has by far the highest likelihood. Figure 29 displays the cumulative flux distributions for the best-fit models, elucidating the reason for their large likelihood. Comparing with Figure 8, we find that this model accounts for the data in much the same way as our broken power law model ( $M_3$ ); but it does so presuming an intrinsically *unbroken* power law distribution of burst fluxes, the apparent break resulting entirely from peak dilution. The curvature and cutoff at large fluxes in the 1024 ms model arise because the best-fit model has a strong correlation between  $\Phi_a$  and peak duration, the peak duration being inversely proportional to  $\Phi_a$ . Thus although  $\tau_0 = 40$  s, the predicted peak duration for the brightest bursts is significantly smaller than 1 s, so the observed 1024 ms peak flux seriously underestimates the actual peak flux for bright bursts.

As a test of this feature of this model, we have examined the publicly available raw OSSE light curves of the five brightest bursts in the 1024 ms data set (Matz 1996). These bursts all have peak 1024 ms fluxes between 20 and 30 ct s<sup>-1</sup> cm<sup>-2</sup>, and span the brief range where the observed flux distribution suddenly cuts off (see the corresponding region of the cumulative histogram in Figure 29b). For one of these bursts, the BATSE and OSSE detectors triggered on a faint precursor, and the main component of the burst lies beyond the 60 s segment in the public OSSE catalog. In Figure 30 we display the light curves for the remaining four bursts; the insets magnify the region of the peak, and include “root- $n$ ” error bars to help distinguish the boundaries of the peak from mere statistical fluctuations. Also shown are the BATSE  $T_{50}$  and  $T_{90}$  burst duration measures. For all of these bursts, the peaks are less than 0.5 s in duration; for three of them the peaks are shorter than 0.1 s. Although we have not performed any rigorous peak fitting, it is clear that the true peak intensity is larger than a 1024 ms average by factors that could easily be much larger than one. The peak durations show no obvious correlation with the  $T_{50}$  and  $T_{90}$  measures of the total burst duration, preventing any simple rescaling of the peak intensity using the timescales reported in the 3B catalog. The underestimation of peak intensity evident for these bursts is consistent with our simple model, although we have not determined whether the data indicate that the true peak duration is correlated with burst intensity. A rigorous analysis of this type requires BATSE light curve and background data that is not part of the 3B catalog. A number of investigators have undertaken analyses of this data in an effort to detect such a correlation (which is expected for cosmological models), but they reach conflicting conclusions (cf. Mitrofanov 1996, Fenimore 1996, and Norris and Nemiroff 1996).

Our motivation for considering this model was not only to attempt to explain the cutoff in the distribution of 1024 ms fluxes, but also to attempt to reconcile the 64 ms and 1024 ms

distributions. The best-fit parameter values for the two data sets are clearly inconsistent with each other, and in that sense this model fails to reconcile them. The inconsistency is not as great as it may appear, however. Figure 31 shows contours of the joint posterior distribution for  $\tau_0$  and  $\sigma$ , conditional on the best-fit values of the underlying flux distribution power law index,  $\gamma_1$ . The 68% (dashed) and 95% (solid) contours are shown. They are highly structured, the structure resulting from the discontinuity in the differential rate for this model (which causes the likelihood to vary greatly as the break point passes through the best-fit flux value for an observed burst). The 1024 ms data constrain  $\tau_0$  to have large values. But the 64 ms data does not strongly constrain  $\tau_0$ ; small values are preferred, but the profile posterior is relatively flat, and large values are thus not strongly ruled out. Despite the disparity between the best-fit parameter values, the 95% credible regions thus have significant regions of parameter space in common.

We conclude that although this model is not entirely successful in explaining the discrepancy between the two data sets, it does indicate that duration effects can strongly distort the observed flux distribution (especially on the 1024 ms time scale) in a manner that can account for the salient features of the data, and that it is likely that duration effects *must* be taken into account in order to understand the shapes of the observed flux distributions.

## 7. Cosmological Models With Beamed Sources

The final model we discuss here is a physical model that combines aspects of many of the models previously discussed. It is a cosmological model with a power-law luminosity function, but it also incorporates temporal and spectral information about bursts. It is of intrinsic physical interest, but it also serves to illustrate how the many characteristics of bursts—not just their peak fluxes and directions, but also their temporal and spectral characteristics—can influence an analysis of the distribution of peak fluxes from bursts.

We consider a homogeneous distribution of burst sources in a flat ( $\Omega_0 = 1$ ) cosmology. We presume the sources are standard candles and clocks *in their rest frame*, but that all the sources are in relativistic motion with common speed  $v \sim c$  (relative to the rest frame of the cosmic background radiation). We also presume that they emit gamma rays isotropically in their rest frame with a common power-law spectrum. As a consequence of their relativistic motion, these sources will appear to be highly beamed to observers at or near rest with respect to the cosmic rest frame. Thus, even though the sources are standard candles intrinsically, sources at a common redshift will have a *distribution* of apparent luminosities, depending on whether they happen to be beamed toward or away from an observer. The shape and width of the luminosity distribution depends both on the source speed and on spectral index. In addition, the sources will appear to have a distribution of peak durations due to the relativistic Doppler shift and cosmological redshift. Since the peak duration affects the measurement of the peak flux, relativistic beaming can make the flux distribution take on different shapes when measured using different integration time scales.

There are two ways we could proceed to calculate the flux distribution from this model. We could generalize equation (27), introducing the beam direction (with respect to the line of sight) as an additional integration variable. The comoving burst rate formally gains the beam direction as an argument (although the distribution of beam directions is presumed isotropic). The  $\Phi_{\text{obs}}$  function also gains this argument, and is complicated by it. The standard candle assumption introduces a  $\delta$ -function in  $\Lambda$  that trivially eliminates one integration dimension, leaving integrations over beam direction and redshift. Of course,  $\Phi_{\text{obs}}$  must additionally be modified to take into account duration effects.

We here adopt an alternative approach that builds upon our existing intuition about models with luminosity functions; it also leads to somewhat simpler numerical calculations. We use equation (27), but with  $\Lambda$  taken to denote the peak *apparent* luminosity along the null ray to Earth, that is, the luminosity one would infer presuming the flux reaching Earth is from an isotropically emitting source. The distribution of beam directions results in an easily calculated distribution of apparent luminosities. With this interpretation of  $\Lambda$ , the only modification of  $\Phi_{\text{obs}}$  required is that needed to account for duration effects. We denote the apparent luminosity by  $\Lambda_{\text{app}}$  to emphasize that it is different from the actual (rest-frame) luminosity of the burst sources.

In Appendix B we carry out a straightforward exercise in relativistic kinematics that shows that the apparent luminosity distribution for a population of beamed sources is a bounded power law,

$$f(\Lambda_{\text{app}}) \propto \begin{cases} \left(\frac{\Lambda_{\text{app}}}{\Lambda_0}\right)^{-p}, & \text{for } \Lambda_l < \Lambda_{\text{app}} < \Lambda_u; \\ 0, & \text{otherwise.} \end{cases} \quad (43)$$

The power law index is related to the spectral index of the sources according to

$$p = \frac{3 + \alpha}{2 + \alpha}; \quad (44)$$

and the lower and upper bounds of the distribution are related to the rest-frame luminosity,  $\Lambda_0$ , according to

$$\Lambda_l = \Lambda_0 \mathcal{D}_b^{-(\alpha+2)}, \quad (45)$$

$$\Lambda_u = \Lambda_0 \mathcal{D}_b^{\alpha+2}. \quad (46)$$

In these equations  $\mathcal{D}_b$  is the relativistic Doppler factor along the beam direction. In terms of the beam velocity parameter,  $\beta = v/c$ , and  $\gamma \equiv 1/\sqrt{1-\beta^2}$ ,

$$\mathcal{D}_b = \frac{1}{\gamma(1-\beta)}. \quad (47)$$

From equation (46), the dynamic range of the power law is  $\mathcal{D}_b^{2\alpha+4}$ , or  $\mathcal{D}_b^7$  for  $\alpha = 1.5$ . For  $\beta \approx 1$ ,  $\mathcal{D}_b \approx 2\gamma$ . Thus for beaming with even moderate values of  $\gamma$ , a very broad luminosity function results.

Since the luminosity function is a power law, in the absence of duration effects this model is identical to the cosmological model with power law luminosity function considered above, with

two exceptions. First, the power law range is parameterized in terms of the physical parameters  $\Lambda_0$  and  $\mathcal{D}_b$ , rather than by its upper limit and dynamic range. More importantly, the power law index is determined by the burst spectrum, and thus is not a free parameter to be inferred separately from the shape of the peak flux distribution. Some of these features of a population of beamed sources have been invoked in analyses of active galaxies (Urry and Shafer 1984, Urry and Padovani 1991). Krolik and Pier (1991) noted other benefits of beaming for modeling burst sources, and Yi (1993, 1994) performed a rough statistical analysis of early BATSE data using models with beamed sources.

Since the sources are standard candles and clocks all moving with the same speed, the observed duration of any particular source is a deterministic function of  $\Lambda_{\text{app}}$ . Put another way,  $\Lambda_{\text{app}}$  is a measure of the beam direction, and thus can be used to specify the Doppler shift. In Appendix B we show that the observed peak duration of a beamed source with apparent luminosity  $\Lambda_{\text{app}}$  at redshift  $z$  is

$$\tau(\Lambda_{\text{app}}, z) = \tau_0(1+z) \left( \frac{\Lambda_{\text{app}}}{\Lambda_0} \right)^{1-p}, \quad (48)$$

where  $\tau_0$  is the peak duration in the source’s rest frame.

With the apparent luminosity and duration of beamed sources specified, we can now specify a model based on a population of such sources. We will calculate the differential burst rate using equation (27), but with  $\Lambda$  replaced by the apparent luminosity  $\Lambda_{\text{app}}$ , and with  $\Phi_{\text{obs}}(z, \Lambda, \mathcal{S})$  generalized to be a function of  $\Lambda_{\text{app}}$  and to take into account durations effects. We take the comoving burst rate density to be constant with redshift, so that  $\dot{n}_c(z, \Lambda) = \dot{n}_0 f(\Lambda_{\text{app}})$ . The observed flux function is

$$\Phi_{\text{obs}}(z, \Lambda_{\text{app}}, \mathcal{S}) = \begin{cases} \frac{\Lambda_{\text{app}}}{4\pi(1+z)d^2(z)} K_0(z, \mathcal{S}), & \text{if } \tau(\Lambda_{\text{app}}, z) \geq \delta t, \\ \frac{\Lambda_{\text{app}}}{4\pi d^2(z)} K_0(z, \mathcal{S}) \left( \frac{\Lambda_{\text{app}}}{\Lambda_0} \right)^{1-p} \frac{\tau(\Lambda_{\text{app}})}{\delta t}, & \text{if } \tau(\Lambda_{\text{app}}, z) < \delta t. \end{cases} \quad (49)$$

The shape parameters of this model are  $\Lambda_0$ ,  $\mathcal{D}_b$  (determined by  $v$ ), and  $\tau_0$ . As noted above, the power law index  $p$  is a function of the spectral index of bursts,  $\alpha$ . We could consider this to be a free parameter (since it influences the shape of the observed flux distribution), but instead we simply take  $\alpha = 1.5$ , the value we adopted for the cosmological models discussed above (and the value adopted by the BATSE team for their detection efficiency calculations). If spectral indices were available for each burst, we could use that information. In fact, this model predicts that the flux distributions of bursts with different  $\alpha$  will have different slopes at low  $\Phi$ , so that including such information in the analysis could strengthen or weaken our preference for this model. But such information is not available in the 3B catalog.

Evaluating the integral in equation (27) for these beamed models is significantly more complicated than for the cosmological models considered earlier. The  $\Phi_{\text{obs}}(z, \Lambda_{\text{app}}, \mathcal{S})$  function has two cases, depending in a nontrivial way on  $\Phi$ ,  $\Lambda_{\text{app}}$ , and  $z$ . Breaking the integral into a sum of integrals separating each case as a function of  $\Phi$  is tedious but straightforward. The resulting

differential rate resembles that of the power-law luminosity function models of § 5.3, except that there is a “kink” where the logarithmic slope of the rate changes from  $p$  at low fluxes to 2.5 at large fluxes. At fluxes below the break, the rate is somewhat elevated due to bursts with actual peak fluxes larger than the break flux but with brief peaks being displaced to below the break. The location and shape of the kink depends on  $\delta t$ , so that the same underlying distribution of true peak fluxes will produce observed distributions with differing shape for data obtained with different trigger time scales.

To study this model, which we denote by  $M_8$ , we fixed the line-of-sight Doppler factor to  $\mathcal{D}_b = 4$ . As just noted, this parameter specifies the dynamic range of the apparent luminosity function, much as does the  $\rho$  parameter for our simple cosmological model with a luminosity function ( $M_6$ ). Recall that  $\rho$  is essentially unconstrained by the data (see Figure 19); the same holds true for  $\mathcal{D}_b$ . Taking  $\mathcal{D}_b = 4$  results in an apparent luminosity function with a dynamic range  $\approx 1.6 \times 10^4$ , about equal to the  $\rho = 10^4$  value we adopted in our analysis of  $M_6$ . We have verified that varying  $\mathcal{D}_b$  does not greatly affect inferences of the remaining shape parameters,  $\Lambda_0$  and  $\tau_0$ . As with our earlier cosmological models, we parameterize the luminosity with a dimensionless parameter,  $\nu_0$ , defined by

$$\Lambda_0 = \nu_0 \frac{4\pi c^2}{H_0^2 F(0)} \Phi_{\text{fid}}. \quad (50)$$

Table 3 lists the best-fit parameters and model comparison statistics for this model. The Bayes factors indicate ambivalence between this model and a simple standard candle model ( $M_4$ ). The best-fit parameter values based on the 64 ms and 1024 ms data are discrepant. Figure 32 shows contours of the joint posterior for  $\nu_0$  and  $\tau_0$ . The posterior is bimodal. For  $\tau_0 > \delta t$ , there is an uncorrelated ridge in the posterior. In this part of parameter space, there is no peak dilution, so the models correspond to simple cosmological models with a power law luminosity function of fixed slope ( $p \approx 1.3$ ). This ridge thus corresponds to a  $p = 1.3$  “slice” of the posterior plotted in Figure 20 (with the  $\nu_u = 1$  corresponding to  $\nu_0 = 1/128$ ). For  $\tau_0 < \delta t$ , peak dilution leads to a strong correlation between the inferred luminosity and duration.

Not surprisingly, the best-fit 64 ms model lies in the “simple” part of parameter space (recall that this data is well-modelled by a single power law), and the best-fit 1024 ms model lies in the part of parameter space where duration effects are important. Figure 33 shows the cumulative flux distributions for the best-fit models, and shows that the duration effects increase the slope of the best-fit 1024 ms flux distribution at large fluxes. But this model is not capable of producing as drastic a change in slope as is the phenomenological model ( $M_7$ ), and so is not as strongly favored.

Despite the disparate best-fit parameter values, the credible regions calculated from the two data sets have significant overlap for rest frame durations  $\tau_0 \gtrsim 2$  s. Unfortunately, this is in the “simple” region of parameter space, corresponding to the overlapping parts of the credible regions for the luminosity function model plotted in Figure 20. Thus the duration effects incorporated in this beamed “top hat” model do not account for the differing shapes of the 64 ms and 1024 ms flux distributions. The model remains of interest, however, both as an interesting physical model

for burst sources, and as an illustration of how both duration and spectral information can be incorporated into analyses of the flux distribution.

## 8. Summary and Discussion

We have analyzed the 64 ms and 1024 ms peak flux data in the 3B catalog using the Bayesian method described in detail by Loredó and Wasserman (1995). The method identifies several shortcomings of the summaries of the data comprising the 3B catalog that prevent consistent analyses of the entire catalog. In particular, counting uncertainties and atmospheric scattering were omitted from the calculation of the detection efficiencies reported in the 3B catalog, requiring that the dimmest 38% of the 64 ms bursts, and the dimmest 16% of 1024 ms bursts, be omitted from any analysis of the peak flux distribution.

We have used the resulting self-consistent data sets to analyze a variety of phenomenological and physical (cosmological) models for burst sources that presume burst sites are distributed isotropically. A companion paper presents analyses of anisotropic models that associate some or all bursts with an extended Galactic halo.

### 8.1. Simple Phenomenological Models

Our analysis of phenomenological models based on power laws and broken power laws verifies that neither the 64 ms nor the 1024 ms data is consistent with a homogeneous (Euclidean) distribution of sources, for which the differential burst rate obeys  $dR/d\Phi \propto \Phi^{-5/2}$ . There is no significant evidence for a break in the logarithmic slope of the distribution of 64 ms peak fluxes, but there is moderately significant evidence for such a break to the homogeneous  $\gamma = 2.5$  slope in the 1024 ms data, and stronger evidence for a steep cutoff in the distribution of bursts with  $\Phi_{1024} \gtrsim 40 \text{ cm}^{-2} \text{ s}^{-1}$ . Also, the power law indices that best describe the low flux portion of each data set differ with at least moderate significance, the low-flux distribution of 1024 ms peak fluxes being somewhat flatter than those favored for the 64 ms peak fluxes. The different inferred shapes of the two data sets are not simply due to their different sizes and dynamic ranges. This argues that a full understanding of the shape of the observed peak flux distribution requires explicit consideration of the temporal structure of burst light curves. A simplified analysis (summarized below) indicates that the structure in the 1024 ms flux distribution is an artifact of its longer measurement time scale, so that the shape of the 64 ms flux distribution is more representative of the shape of the distribution of instantaneous peak fluxes.

Several physical models for the distribution of burst sources in space and luminosity predict flux distributions that are well approximated by power laws and broken power laws, as noted in § 4. Quite generically, information about characteristic length and luminosity scales in such models is revealed by a change in the logarithmic slope of the flux distribution from a relatively

flat differential distribution for dim bursts to a steeper  $\Phi^{-5/2}$  distribution for bright bursts. That there is no evidence for such a change in the 64 ms data, and only moderate evidence for a change to a  $\Phi^{-5/2}$  power law in the 1024 ms data, presaged the conclusions we found in our analyses of physical models: the data are unable to constrain properties of cosmological populations of burst sources.

## 8.2. Simple Cosmological Models

We analyzed three simple cosmological models in an effort to determine whether the 3B data could detect or rule out evolution of the burst rate density with redshift, and whether the data could constrain the width of the burster luminosity function. The data are unable to discriminate among homogeneous standard candle models and models with strong density evolution or broad luminosity functions. As a consequence, the luminosity of burst sources is uncertain over many orders of magnitude, and the typical redshifts of observed bursts can be as small as a few tenths or  $\gtrsim 20$ . The upper limit could almost certainly be reduced by considering PVO data, since it depends on locating the flux where the flux distribution steepens to  $dR/d\Phi \propto \Phi^{-5/2}$ . A stronger constraint may arise from the absence of large time dilation in burst lightcurves, although the wide variety of temporal behavior exhibited by bursts severely complicates the modeling and detection of such time dilation (see, e.g., Mitrofanov 1996, Fenimore 1996, and Norris and Nemiroff 1996, who reach conflicting conclusions regarding the presence of “time stretching” in BATSE data). A lower limit on the redshift of observed sources may be sought more effectively from the absence of anisotropy in the distribution of burst directions (as would appear if many bursts were visible from within the local supercluster, for example) than from the flux distribution (see, e.g., Quashnock 1996). Since such anisotropy should correlate with burst intensity, our Bayesian methodology is an ideal tool for rigorously studying it.

Even in the absence of strong density evolution (in which case the observed bursts have typical redshifts of a few tenths), the width of the luminosity function for burst sources is unconstrained and could span several orders of magnitude. Unfortunately, we find that the uncertainty in the luminosity of the brightest burst sources is comparable in size to the range of the luminosity function, and thus is largely unconstrained by the BATSE data. The addition of PVO data is unlikely to strengthen this constraint, because models with luminosity functions of very different widths distinguish themselves at low fluxes rather than at large fluxes. Without a vastly larger data set, the best hope for constraining the width of the luminosity function of cosmological burst sources is to obtain data on the distribution of bursts with fluxes well below the threshold of the BATSE detectors.

### 8.3. Consideration of Temporal and Spectral Properties of Bursts

Analyses with sufficiently flexible models reveal systematic differences between the shapes of the distributions of 64 ms and 1024 ms peak fluxes. Parameters inferred from the two data sets differ with moderate significance presuming they are independent. But since the two data sets are not independent (well over half of the 1024 ms bursts triggered on the 64 ms timescale) one would expect close agreement between the inferred values; the discrepancy between the inferences is thus probably very significant. In addition, the normalizations of the two distributions are extremely different, the number of 1024 ms bursts with fluxes above  $1.5 \text{ cm}^{-2} \text{ s}^{-1}$  (the cutoff for 64 ms bursts) being only 56% of the number of 64 ms bursts. In LW95 we argued that explicit consideration of the temporal properties of bursts would be necessary for understanding the distribution of measured burst fluxes. The disparity between the 64 ms and 1024 ms data supports this claim.

We therefore attempted to model the data in a manner that crudely accounts for “peak dilution”: the underestimation of peak flux that occurs when estimating peak flux with data from a time interval longer than the peak duration. If peak duration is correlated with peak flux, peak dilution can result in an observed peak flux distribution that is different in shape from the underlying actual peak flux distribution. Unfortunately, the 3B catalog contains no direct information about the peak durations of bursts. Thus we have been able to perform only illustrative calculations that show how explicit consideration of temporal properties of bursts might enter an analysis of the flux distribution. Should peak duration measurements become available, more reliable and definitive analyses will be possible.

We analyzed a purely phenomenological model in which bright bursts were presumed to have shorter peak durations than dim bursts (the qualitative behavior expected in cosmological models). Thus bright bursts have their peak fluxes systematically underestimated when long measuring time scales are used, steepening the flux distribution at bright fluxes. This model is moderately successful in reconciling the shapes of the two data sets, and in particular is capable of producing a cutoff in the distribution of observed peak fluxes, as is seen in the 1024 ms data. Additionally, we analyzed a physical model in which a cosmological population of relativistically beamed sources that are standard candles and clocks produces an apparent distribution of sources with a broad luminosity function and distribution of peak durations, due to the distribution of the angle between the source velocity and the line of sight. Besides correlating burst duration and peak flux, this model also correlates the burst spectrum with peak flux and duration. However, it does not successfully account for the differences between the two data sets. Nevertheless, it is of intrinsic physical interest, and further, it is the simplest model illustrating how the spectral and temporal properties of bursts can enter the analysis of the flux distribution.

We thus conclude that the BATSE peak flux data cannot usefully constrain cosmological models for burst sources. Useful constraints from peak fluxes alone will result only from

consideration of data about the infrequent bright bursts that BATSE has not yet seen (to constrain the redshifts of the most distant observed sources), and about bursts dimmer than BATSE is capable of seeing (to constrain the width of the luminosity function). Joint analyses of temporal and spectral properties of bursts with their peak fluxes may well provide more useful constraints on cosmological models. The Bayesian methodology adopted here is the ideal tool for such a joint analysis.

This work was supported in part by NASA grants NAG 5-1758, NAG 5-2762, NAG 5-3097, and NAG 5-3427; and by NSF grants AST91-19475 and AST-93-15375.

## A. Derivation and Properties of the Cosmological Burst Rate

We present here a detailed derivation of the expressions referred to in the text for calculating the differential burst rate from cosmological models (eqn. (27) and the various functions that appear in that equation). Much of our treatment follows that of Weinberg (1972); the most important differences between our analysis and his result from our interest in sources detected by measurements of peak photon flux, rather than energy flux or fluence, and from our interest in inferring a rate density rather than a number density. We also derive here expressions for the distribution of observable sources with redshift and luminosity, and we find expressions for the logarithmic slope of the differential rate in various regimes. We use these latter expressions in the main text to motivate our study of power laws and to explain the shape of some of our posterior distributions.

Our task is to generalize equation (1) to a cosmological setting. This involves finding an expression for the volume element in terms of convenient coordinates for events in spacetime, and taking into account cosmological effects in expressions for the burst rate density, and for the observed peak flux from a cosmological source. We address these tasks in turn.

### A.1. The Volume Element

Our starting point is the Robertson-Walker metric, which specifies the interval of proper time,  $d\tau$ , between events separated by an infinitesimal cosmic time interval  $dt$  and by infinitesimal comoving spherical coordinate intervals  $dr$ ,  $d\theta$ , and  $d\phi$ :

$$d\tau^2 = dt^2 - \frac{a^2(t)}{c^2} \left[ \frac{dr^2}{1 - kr^2} + r^2(d\theta^2 + \sin^2\theta d\phi^2) \right]. \quad (\text{A1})$$

The time dependence of the scale factor,  $a(t)$ , will be determined by the Einstein equations. We assign units of length to  $a(t)$ , so that the comoving coordinate  $r$  is a dimensionless coordinate label. The dimensionless constant  $k$  is the curvature constant whose sign determines the sign

of the spatial curvature of three-dimensional spaces of constant  $t$ . We take the origin of the coordinate system ( $r = 0$ ) to be at Earth.

Equation (1) requires the volume element for three-dimensional spaces of constant  $t$ . The metric for such spaces can easily be read off of equation (A1); the square root of its determinant gives

$$dV(r, \theta, \phi) = \frac{a^3(t)}{\sqrt{1 - kr^2}} r^2 dr d\mathbf{n}, \quad (\text{A2})$$

where  $d\mathbf{n} = \sin\theta d\theta d\phi$  is the familiar solid angle element in spherical coordinates. Besides the three spatial coordinates, the cosmic time,  $t$ , appears in  $dV$  in the scale factor. It must be set equal to the coordinate time of the observed event. Since we are interested only in events observed with light, there is a one-to-one correspondence between  $t$  and  $r$  determined by the condition that events be connected to the origin by radial null rays. In addition, it proves most convenient to parameterize such rays by the redshift,  $z$ , rather than by  $t$  or  $r$ , where  $z$  is given by

$$1 + z = \frac{a_0}{a(t)}, \quad (\text{A3})$$

where  $a_0 = a(0)$ . For null rays, equation (A2) thus can be written as

$$dV(z, \theta, \phi) = ca_0^2 \frac{r^2(z)}{(1+z)^3 H(z)} dz d\mathbf{n}, \quad (\text{A4})$$

where  $r(z)$  is the radial coordinate of a source at redshift  $z$ , and  $H(z)$  is the Hubble factor defined by  $H(z) = \dot{a}(z)/a(z)$ .

To calculate  $H(z)$  and  $r(z)$  we need to solve the Einstein equations for the evolution of the scale factor. The energy-momentum tensor in a Robertson-Walker universe necessarily takes the form of that of a perfect fluid, and thus can be characterized by the fluid density  $\rho$  and pressure  $p$ . The Einstein equations based on this metric and energy-momentum tensor reduce to two second order differential equations relating  $\rho(z)$ ,  $p(z)$ , and  $a(t)$ . Since we are concerned with events at epochs when the universe is matter-dominated, we simply set  $p = 0$ . We also set the cosmological constant equal to zero throughout this paper. The Einstein equations can then be easily solved, giving

$$H(z) = H_0(1+z)\sqrt{1+2q_0z}, \quad (\text{A5})$$

where  $H_0 = H(0)$  is the Hubble constant and  $q_0$  is the deceleration constant. The deceleration constant is related to the density at the current epoch,  $\rho_0$ , according to  $\Omega_0 = 2q_0$ , where  $\Omega_0$  is the ratio of  $\rho_0$  to the critical density corresponding to a  $k = 0$  universe,

$$\Omega_0 = \frac{8\pi G\rho_0}{3H_0^2}. \quad (\text{A6})$$

Since  $H(z)$  specifies the redshift dependence of the scale factor, we can use it to evaluate  $r(z)$  (Weinberg 1972, eqn. 15.3.23). The result is

$$r(z) = \frac{c}{H_0 a_0 q_0^2 (1+z)} \left[ q_0 z + (1 - q_0) \left( 1 - \sqrt{2q_0 z + 1} \right) \right]. \quad (\text{A7})$$

With  $H(z)$  and  $r(z)$  now available, the volume element finally takes the form,

$$dV(z, \theta, \phi) = \frac{ca_0^2}{H_0} \frac{r^2(z)}{(1+z)^4 \sqrt{1+2q_0z}} dz d\mathbf{n}. \quad (\text{A8})$$

## A.2. The Burst Rate

The differential rate integrand includes the burst rate density, denoted  $\dot{n}(\mathbf{r}, \Lambda)$  in equation (1). In a cosmological setting, where there is a difference between proper volume and comoving volume, and between local time intervals and time intervals observed at large redshift, care must be taken in defining the burst rate.

The observed time interval,  $dt$ , between events at redshift  $z$  separated by a time interval  $dt'$  is given by  $dt = (1+z)dt'$ . Let  $\dot{n}_p(z, \Lambda)$  denote the proper burst rate density, so that the burst rate measured by observers at redshift  $z$  due to sources in a volume  $dV$  and luminosity interval  $d\Lambda$  at that redshift is  $\dot{n}_p(z, \Lambda)dVd\Lambda$ . Then the *apparent* burst rate from that volume and luminosity interval, as measured by observers at  $z = 0$ , will be  $\dot{n}_p(z, \Lambda)dVd\Lambda/(1+z)$ . Thus a factor of  $1/(1+z)$  must be inserted into the integrand of equation (1) when cosmological sources are considered. This factor was neglected by Wickramasinghe et al. (1993) and by Horack, Emslie, and Meegan (1994), who used results appropriate for number densities rather than rate densities.

In addition, it is more natural to specify the burst rate per unit *comoving* volume element (i.e., per unit volume element expanding with the separations between galaxies) than per unit *proper* volume element. The comoving burst rate density,  $\dot{n}_c$ , is related to the proper burst rate density according to  $\dot{n}_c = \dot{n}_p a^3 = \dot{n}_p a_0^3 / (1+z)^3$ . Note that since the comoving radial coordinate  $r$  is dimensionless,  $\dot{n}_c$  has units of the product of inverse time and inverse luminosity, with no inverse volume dimensions.

These considerations, combined with the volume element calculated above, lead to a cosmological counterpart to equation (1) that we can trivially integrate over  $\mathbf{n}$  (presuming an isotropic burst rate density) to obtain the counterpart to equation (11),

$$\frac{dR}{d\Phi} = \frac{4\pi c}{H_0 a_0} \int dz \int d\Lambda \frac{r^2(z)}{(1+z)^2 \sqrt{1+2q_0z}} \dot{n}_c(z, \Lambda) \delta[\Phi - \Phi_{\text{obs}}(\Lambda, \mathcal{S}, z)]. \quad (\text{A9})$$

Here  $\Phi_{\text{obs}}(\Lambda, \mathcal{S}, z)$  is a function specifying the peak flux one would observe from a source with peak photon luminosity  $\Lambda$  at redshift  $z$ , with a spectrum described by spectral parameters  $\mathcal{S}$ . The  $4\pi$  factor out front came from performing the integration over  $d\mathbf{n}$  (ignoring any apparent and, presumably, slight anisotropy induced by motion with respect to the cosmic rest frame).

### A.3. The Peak Flux

To evaluate equation (A9), we must specify  $\dot{n}_c(z, \Lambda)$  and  $\Phi_{\text{obs}}(\Lambda, \mathcal{S}, z)$ . The former depends on the burst source model, but the latter depends primarily on the cosmology and burst spectrum (it will also depend on the light curve, as noted in the text and in Appendix B). We evaluate  $\Phi_{\text{obs}}(\Lambda, \mathcal{S}, z)$  for bursts with power-law spectra here.

We will calculate  $\Phi_{\text{obs}}$  simply by requiring that the number of photons that pass through spherical surfaces centered at a burst site be conserved. Let  $A$  denote the area of a spherical wavefront just reaching Earth from a source at redshift  $z$ . We define the distance  $d(z)$  traveled by the wavefront by writing  $A = 4\pi d^2(z)$ ; as shown by Weinberg (1972), this implies that  $d(z) = R_0 r(z)$ .

Let  $\Lambda dt'$  denote the number of photons emitted by the source in a pulse of duration  $dt'$  in its rest frame. Focus attention on a small group of the photons with rest-frame energies  $\epsilon'$  in the interval  $[\epsilon', \epsilon' + d\epsilon']$ , and let the fraction of all photons with energies in this range be given by  $\phi(\epsilon')d\epsilon'$ . The  $\phi(\epsilon')$  function describes the shape of the burst spectrum, and must be normalized so that  $\int d\epsilon' \phi(\epsilon') = 1$ .

Now consider this pulse of photons as it reaches a sphere of radius  $A$  at a redshift  $z$  from the source. Let  $\xi(\epsilon)A d\epsilon dt$  denote the number of photons that pass through the sphere in a time  $dt$  and with energies in  $[\epsilon, \epsilon + d\epsilon]$ , with all quantities measured on the sphere. The function  $\xi(\epsilon)$  is thus the photon number flux per unit energy through the spherical surface. Now focus attention on the group of photons just described above. Any such photon that started with rest-frame energy  $\epsilon'$  will be detected with energy  $\epsilon = \epsilon'/(1+z)$ ; and the energy interval spanned by the photons will be  $d\epsilon = d\epsilon'/(1+z)$ . Also, the time spanned by the pulse will be  $dt = (1+z)dt'$ . Requiring the number of photons in these energy and time intervals to equal the number emitted in the corresponding intervals at the source implies

$$4\pi d^2 \xi(\epsilon) d\epsilon dt = \Lambda \phi(\epsilon') d\epsilon' dt'. \quad (\text{A10})$$

Solving for  $\xi(\epsilon)$ , and casting all quantities in terms of those measured at the sphere gives

$$\xi(\epsilon) = \frac{\Lambda \phi[\epsilon(1+z)]}{4\pi d^2(z)}. \quad (\text{A11})$$

The photon number flux measured by a detector with an energy-dependent detection efficiency  $k(\epsilon)$  is  $\Phi_{\text{obs}} = \int_0^\infty d\epsilon k(\epsilon) \xi(\epsilon)$ . Using equation (A11), and transforming the integral from  $\epsilon$  to  $\epsilon'$ , we can write this as

$$\Phi_{\text{obs}}(\Lambda, \mathcal{S}, z) = \frac{\Lambda}{4\pi(1+z)d^2(z)} K_0(z, \mathcal{S}), \quad (\text{A12})$$

where the  $1/(1+z)$  factor arose from changing the integration variable from  $\epsilon$  to  $\epsilon'$ ; and the spectral correction function  $K_n(z, \mathcal{S})$  is given by

$$K_n(z, \mathcal{S}) = \frac{1}{(1+z)^n} \int_0^\infty d\epsilon' (\epsilon')^n k[\epsilon'/(1+z)] \phi(\epsilon'). \quad (\text{A13})$$

This function specifies the gamma ray burst counterpart to the  $K$ -corrections familiar from analyses of optical observations of cosmological sources. Note that it depends not only on redshift, but also on the shape of the burst spectrum and the efficiency function of the detector. We have defined it with a general index,  $n$ , for the sake of generality. Had we been concerned with observations of a burst’s *energy* flux  $F$ , rather than its photon number flux, then the observed energy flux would be  $F_{\text{obs}} = \int d\epsilon k(\epsilon)\epsilon\xi(\epsilon)$ . The energy flux counterpart of equation (A12) is then

$$F_{\text{obs}}(\Lambda, \mathcal{S}, z) = \frac{\Lambda}{4\pi(1+z)d^2(z)} K_1(z, \mathcal{S}). \quad (\text{A14})$$

The energy flux thus has a different dependence on both  $z$  and  $\mathcal{S}$  than does the photon number flux. Other measures of burst intensity (such as the total (time-integrated) photon number per unit area, or the fluence) have yet different dependences (e.g., time integrals introduce further  $(1+z)$  factors when one transforms from the detector frame to the source frame).

In this work, we calculate  $K_0$  using a detection efficiency that is constant (equal to unity) from  $\epsilon_1$  to  $\epsilon_2$  and that vanishes outside this range. We set  $\epsilon_1 = 60$  keV and  $\epsilon_2 = 300$  keV, the nominal energy boundaries of the BATSE detectors during the observations comprising the 3B catalog. This “top hat” efficiency function results in the integral over  $\epsilon'$  in equation (A13) having a  $z$ -dependent range, extending from  $\epsilon_1(1+z)$  to  $\epsilon_2(1+z)$ . We also use a power-law photon spectrum, with  $\phi(\epsilon') \propto (\epsilon')^{-\alpha}$ , with the spectrum extending from  $\epsilon'_l$  to  $\epsilon'_u$ . The spectral parameters are thus  $\mathcal{S} = \{\alpha, \epsilon'_l, \epsilon'_u\}$ . The resulting spectral correction function is

$$K_0(z, \mathcal{S}) = \begin{cases} \frac{\log(\epsilon_2/\epsilon_1)}{\log(\epsilon'_u/\epsilon'_l)}, & \text{for } \alpha = 1, \\ \left(\frac{\epsilon_2}{\epsilon'_u}\right)^{1-\alpha} (1+z)^{1-\alpha} \frac{(\epsilon_2/\epsilon_1)^{\alpha-1}-1}{(\epsilon'_u/\epsilon'_l)^{\alpha-1}-1}, & \text{for } \alpha \neq 1. \end{cases} \quad (\text{A15})$$

This form applies only for redshifts close enough that  $\epsilon'_u$  is not redshifted to within the detector passband; this assumption is justified in that no bursts exhibit sharp spectral breaks within the passband. Note that, for  $\alpha = 1$ , the spectral correction function is independent of  $z$ , and that it depends only weakly on the spectral parameters  $\epsilon'_u$  and  $\epsilon'_l$ . We set  $\epsilon'_l = 60$  keV, and  $\epsilon'_u = X$  keV.

We now have all the ingredients needed to calculate the burst rate according to equation (A9). We can facilitate the differential rate calculation by rewriting the  $\delta$ -function in equation (A9) so that its argument is an expression for one of the integration variables, rather than for  $\Phi$ . For standard candle models, the burst rate density includes a  $\delta$ -function in  $\Lambda$ , so the appropriate transformation is from  $\Phi$  to  $z$  (so as to avoid a product of  $\delta$ -functions with the same argument). Let  $z'(\Phi, \Lambda, \mathcal{S})$  be the redshift value that solves equation (A12) when the value of the left hand side is given as  $\Phi$ . This function must be calculated by numerically solving equation (A12). In terms of  $z'(\Phi, \Lambda, \mathcal{S})$ ,

$$\delta[\Phi - \Phi_{\text{obs}}(\Lambda, \mathcal{S}, z)] = \delta[z - z'(\Phi, \Lambda, \mathcal{S})] \left| \frac{d\Phi_{\text{obs}}}{dz} \right|^{-1}. \quad (\text{A16})$$

We can calculate the derivative from equation (A12), giving

$$\frac{d\Phi_{\text{obs}}}{dz} = \Phi_{\text{obs}}(\Lambda, \mathcal{S}, z) \left( \frac{K'_0(z, \mathcal{S})}{K_0(z, \mathcal{S})} - 2 \frac{r'(z)}{r(z)} - \frac{1}{1+z} \right), \quad (\text{A17})$$

where  $r'(z)$  and  $K'_0(z, \mathcal{S})$  denote the derivatives of  $r(z)$  and  $K_0(z, \mathcal{S})$  with respect to  $z$ , which we can easily calculate from their defining expressions above. With these results, and a standard candle luminosity of  $\Lambda_c$ , the differential rate integral of equation (A9) becomes

$$\frac{dR}{d\Phi} = \frac{4\pi c}{H_0 a_0} \frac{r^2(z')}{(1+z')^2 \sqrt{1+2q_0 z'}} \dot{n}_c(z') \frac{1}{\Phi_{\text{obs}}(\Lambda_c, \mathcal{S}, z') \left( \frac{K'_0(z', \mathcal{S})}{K_0(z', \mathcal{S})} - 2 \frac{r'(z')}{r(z')} - \frac{1}{1+z'} \right)}, \quad (\text{A18})$$

where  $z'$  is everywhere equal to  $z'(\Phi, \Lambda_c, \mathcal{S})$ , and  $\dot{n}_c(z)$  is the burst rate density without the  $\delta$ -function luminosity factor.

For models with nondegenerate luminosity functions, calculations may be facilitated by instead transforming from  $\Phi$  to  $\Lambda$ , in which case

$$\delta[\Phi - \Phi_{\text{obs}}(\Lambda, \mathcal{S}, z)] = \frac{4\pi(1+z)d^2(z)}{K_0(z, \mathcal{S})} \delta \left[ \Lambda - \frac{4\pi d^2(1+z)\Phi}{K_0(z, \mathcal{S})} \right]. \quad (\text{A19})$$

Using this in equation (A9) gives this version of the differential rate equation,

$$\frac{dR}{d\Phi} = \frac{16\pi^2 c a_0}{H_0} \int dz \frac{r^4(z)}{K_0(z, \mathcal{S})(1+z)\sqrt{1+2q_0 z}} \dot{n}_c(z, \Lambda'), \quad (\text{A20})$$

where  $\Lambda'$  is given by

$$\Lambda'(\Phi, z, \mathcal{S}) = \frac{4\pi d^2(1+z)\Phi}{K_0(z, \mathcal{S})}. \quad (\text{A21})$$

#### A.4. Redshift and Luminosity Distributions of Observable Sources

From the results already derived, it is straightforward to calculate the redshift distribution of sources visible from Earth. We first note that the differential rate per unit  $\Phi$  per unit  $z$  is available from inspection of equation (A9); we need only omit the integration over  $dz$  on the right hand side. Integrating the resulting expression over  $\Phi$  is trivial due to the  $\delta$ -function; the result is

$$\frac{dR}{dz} = \frac{c}{H_0 a_0} \frac{4\pi r^2(z)}{(1+z)^2 \sqrt{1+2q_0 z}} \int d\Lambda \dot{n}_c(z, \Lambda). \quad (\text{A22})$$

If we write  $\dot{n}_c(z, \Lambda)$  as the product of the burst rate per comoving volume,  $\dot{n}_c(z)$ , and a normalized conditional luminosity function,  $f(\Lambda | z)$ , we can also easily perform the integral over luminosity, giving

$$\frac{dR}{dz} = \frac{c}{H_0 a_0} \frac{4\pi r^2(z)}{(1+z)^2 \sqrt{1+2q_0 z}} \dot{n}_c(z). \quad (\text{A23})$$

This gives the redshift distribution visible to a *perfect* detector. The *effective* differential rate—that visible to a detector with limited detection efficiency—is simply  $\bar{\eta}'(\Phi)dR/d\Phi$ . Repeating the above calculations, we find that the redshift distribution of bursts visible to a real detector is given by equation (A22), but with a factor of  $\bar{\eta}'[\Phi_{\text{obs}}(\Lambda, z, \mathcal{S})]$  inserted on the right hand side. The luminosity integral no longer gives a simple, general result. But for standard candle models with luminosity  $\Lambda_c$ , the integral can be performed, giving a result like equation (A23), but with a factor of  $\bar{\eta}'[\Phi_{\text{obs}}(\Lambda_c, z, \mathcal{S})]$  appearing on the right hand side. The efficiency function has the effect of truncating the distribution at large  $z$ .

We can similarly find the effective luminosity function. Multiplying equation (A22) by  $\bar{\eta}'[\Phi_{\text{obs}}(\Lambda, z, \mathcal{S})]$ , interchanging the roles of  $\Phi$  and  $\Lambda$ , and performing the integral over  $\Phi$  (made trivial by the  $\delta$ -function) gives

$$\frac{dR_{\text{eff}}}{d\Lambda} = \frac{c}{H_0 a_0} \int dz \frac{4\pi r^2(z)}{(1+z)^2 \sqrt{1+2q_0 z}} \dot{n}_c(z, \Lambda) \bar{\eta}'[\Phi_{\text{obs}}(\Lambda, z, \mathcal{S})]. \quad (\text{A24})$$

We discuss the properties of this function at the end of § 5.3.

### A.5. Limiting Behavior of the Rate

To understand some of the inferences found in the text, it is useful to know the behavior of the logarithmic slope of the differential rate as a function of  $\Phi$  for various choices of  $\dot{n}_c(z, \Lambda)$ . We collect some such results here.

First, if  $\dot{n}_c(z, \Lambda)$  concentrates observable bursts to redshifts significantly less than unity, it is clear that cosmological effects are negligible, so that  $dR/d\Phi$  shares the properties of rates derived from Euclidean models. This will be the case if the burst rate per unit volume is concentrated at low  $z$ , or if it is spread out but sources have luminosities that are visible only from low redshifts.

It follows that the brightest bursts (presumably from nearby sources at  $z < 1$ ) should have a differential distribution proportional to  $\Phi^{-5/2}$ . Of course, the flux corresponding to sources at  $z < 1$  could be beyond the range of the BATSE data, so that the  $\Phi^{-5/2}$  regime is not yet evident in the BATSE data (although it appears to have been detected by PVO; see Fenimore et al. 1993, and Fenimore and Bloom 1996a).

The dimmest bursts could possibly be due to sources at large redshifts, so it is interesting to know the behavior of the differential rate when it is dominated by sources with  $z \gg 1$ . Following along the lines of the discussion at the start of § 4, we first find the  $z$  dependence of  $dR/dz$  at large  $z$ , then find the  $z$  dependence of  $\Phi_{\text{obs}}(\Lambda, z, \mathcal{S})$ , and finally change variables from  $z$  to  $\Phi$  to calculate  $dR/d\Phi$ .

Begin by noting that, from equation (A7), we find that  $r(z) \rightarrow c/H_0 R_0 q_0$ , a constant, at large  $z$ . Now examine equation (A22), and take  $\dot{n}_c(z) \propto (1+z)^{-\beta}$ , as we did in the inhomogeneous

standard candle model considered in § 5. For  $z \gg 1$ , we find that

$$\frac{dR}{dz} \propto z^{-\beta-\frac{5}{2}}. \quad (\text{A25})$$

To find the large  $z$  behavior of the flux, as given by equation (A12), we need to know the large  $z$  behavior of  $K_0(z, \mathcal{S})$ . From equation (A15) we find  $K_0 \propto z^{1-\alpha}$ . Since  $d(z) \propto r(z)$ , we thus find from equation (A12) that  $\Phi \propto z^{-\alpha}$ . This allows us to change variables in equation (A25), giving

$$\frac{dR}{d\Phi} \propto \Phi^{\frac{\beta}{\alpha} + \frac{3}{2\alpha} - 1}. \quad (\text{A26})$$

For  $\alpha = 3/2$ , we find  $dR/d\Phi \propto \Phi^{2\beta/3}$ , the power law behavior noted in the main text.

## B. Sources With Relativistic Beaming

In this Appendix we derive two important properties of a population of standard candle, standard clock beamed sources used in § 7: the power-law distribution of apparent luminosities, and the relationship between apparent luminosity and peak duration.

Consider a source emitting photons isotropically in its rest frame with a photon number luminosity  $\Lambda_0$ , and moving with velocity  $\mathbf{v}$  with respect to a cosmologically local observer at rest with respect to the cosmic background radiation (hereafter the “local observer”). We describe events in the source’s rest frame (the “source frame”) and the local observer’s frame using coordinate systems whose origins are coincident at the moment of the events under consideration. We will identify rest-frame quantities with a “0” subscript, with corresponding quantities in the local observer’s frame denoted with a prime. Quantities measured at Earth are denoted without a subscript or prime. We use the standard symbols  $\beta = v/c$  and  $\gamma = 1/\sqrt{1-\beta^2}$  where convenient.

Consider a pulse of photons emitted by the source in a time  $dt_0$  and in a narrow cone of solid angle  $d\mathbf{n}_0$  along the line of sight to Earth at an angle  $\theta_0$  from the direction of motion with direction cosine  $\mu_0 = \cos\theta_0$ . Denote the fraction of photons emitted with rest-frame energies in  $[\epsilon_0, \epsilon_0 + d\epsilon_0]$  by  $\phi(\epsilon_0)d\epsilon_0$ . Then the number of photons in the pulse with energies in  $d\epsilon_0$  is

$$dn = \frac{\Lambda}{4\pi} \phi(\epsilon_0) dt_0 d\epsilon_0 d\mathbf{n}_0. \quad (\text{B1})$$

The local observer sees this pulse over a time interval given by the Doppler formula as  $dt' = dt_0/\mathcal{D}(\beta, \mu)$ , where  $\beta = v/c$  and  $\mathcal{D}(\beta, \mu)$  is the Doppler factor,

$$\mathcal{D}(\beta, \mu) = \frac{1}{\gamma(1 - \beta\mu)}. \quad (\text{B2})$$

In addition, the cone will appear at an angle  $\theta'$  with respect to the direction of motion of the source, with  $\mu' = \cos\theta'$  given by

$$\mu' = \frac{\mu_0 + \beta}{1 + \beta\mu_0}. \quad (\text{B3})$$

It will subtend a solid angle  $d\mathbf{n}' = d\mathbf{n}_0/\mathcal{D}^2(\beta, \mu)$ . Finally, the photons will be observed at an energy  $\epsilon' = \mathcal{D}(\beta, \mu')\epsilon_0$ , over an energy interval  $d\epsilon' = \mathcal{D}(\beta, \mu')d\epsilon_0$ . These relationships between source and local observer quantities lets us rewrite equation (B1) as

$$dn = \mathcal{D}^2 \frac{\Lambda}{4\pi} \phi(\epsilon'/\mathcal{D}) dt' d\epsilon' d\mathbf{n}', \quad (\text{B4})$$

where we have temporarily suppressed the arguments of  $\mathcal{D}(\beta, \mu')$ .

At Earth, the pulse will have duration  $dt = (1+z)dt'$ . The photons will have energy  $\epsilon = \epsilon'/(1+z)$  and will span an energy interval of size  $d\epsilon = d\epsilon'/(1+z)$ . If the pulse is observed with a detector of area  $A$  normal to the line of sight, then the solid angle subtended by the detector in the local observer frame is  $d\mathbf{n}' = A/d^2(z)$ . Thus we can rewrite equation (B4) as

$$dn = \mathcal{D}^2 \frac{\Lambda}{4\pi d^2(z)} \phi[\epsilon'(1+z)/\mathcal{D}] A dt d\epsilon. \quad (\text{B5})$$

The flux per unit energy is just  $\xi(\epsilon) = dn/(A dt d\epsilon)$ . As in Appendix A, the photon number flux measured by a detector with efficiency  $k(\epsilon)$  is  $\Phi_{\text{obs}} = \int d\epsilon k(\epsilon) \xi(\epsilon)$ . Using equation (B5), and transforming the integration variable from  $\epsilon$  to  $\epsilon'$ , this expression becomes

$$\Phi_{\text{obs}}(z, \Lambda_{\text{app}}, \mathcal{S}) = \mathcal{D}^2 \frac{\Lambda_0}{4\pi(1+z)d^2(z)} \int d\epsilon' k[\epsilon'/(1+z)] \phi(\epsilon'/\mathcal{D}). \quad (\text{B6})$$

Now define the apparent luminosity of the source,  $\Lambda_{\text{app}}$ , by writing, in a manner analogous to equation (25),

$$\Phi_{\text{obs}}(z, \Lambda_{\text{app}}, \mathcal{S}) \equiv \frac{\Lambda_{\text{app}}}{4\pi(1+z)d^2(z)} K_0(z, \mathcal{S}). \quad (\text{B7})$$

Comparing this with equation (B6), and using the definition of  $K_0$  in equation (A13), gives

$$\Lambda_{\text{app}} = \mathcal{D}^2 \Lambda_0 \frac{\int d\epsilon' k[\epsilon'/(1+z)] \phi(\epsilon'/\mathcal{D})}{\int d\epsilon' k[\epsilon'/(1+z)] \phi(\epsilon')}. \quad (\text{B8})$$

Although the ratio of integrals appearing here is not trivial in general, for power-law spectra proportional to  $(\epsilon')^{-\alpha}$  we easily find that

$$\Lambda_{\text{app}} = [\mathcal{D}(\beta, \mu')]^{2+\alpha} \Lambda_0, \quad (\text{B9})$$

provided the lower and upper limits of the spectrum do not enter the detector passband at the redshifts of interest.

Equation (B9) reveals the apparent luminosity of a beamed source to be strongly angle and velocity dependent. Distributions of beaming angles and velocities thus produce an apparent luminosity function. In this work, we presume that all sources have the same velocity. The luminosity function is thus that due to the distribution of beaming angles, which must be isotropic in an isotropic cosmology. If we denote the fraction of sources with apparent luminosity in

$[\Lambda_{\text{app}}, \Lambda_{\text{app}} + d\Lambda_{\text{app}}]$  by  $f(\Lambda_{\text{app}})d\Lambda_{\text{app}}$ , and if the range of beaming angle cosines corresponding to  $d\Lambda_{\text{app}}$  is  $d\mu'$ , then  $f(\Lambda_{\text{app}})d\Lambda_{\text{app}} = d\mu'/2$ , so that

$$f(\Lambda_{\text{app}}) = \frac{1}{2} \left( \frac{d\Lambda_{\text{app}}}{d\mu'} \right)^{-1}. \quad (\text{B10})$$

Calculating the derivative reveals the apparent luminosity function to be a power law;

$$f(\Lambda_{\text{app}}) = \begin{cases} \frac{1}{2\Lambda_0\gamma\beta(2+\alpha)} \left( \frac{\Lambda_{\text{app}}}{\Lambda_0} \right)^{-\frac{3+\alpha}{2+\alpha}} & \text{for } \Lambda_l < \Lambda_{\text{app}} < \Lambda_u, \\ 0 & \text{otherwise.} \end{cases} \quad (\text{B11})$$

The limits of the power law are

$$\Lambda_l = \Lambda_0 \mathcal{D}_b^{-(\alpha+2)}, \quad (\text{B12})$$

$$\Lambda_u = \Lambda_0 \mathcal{D}_b^{\alpha+2}; \quad (\text{B13})$$

where  $\mathcal{D}_b = \mathcal{D}(\beta, 1)$  is the relativistic Doppler factor along the beam direction (i.e., for  $\mu' = 1$ ). For large  $\gamma$  (so that  $\beta \approx 1$ ),  $\mathcal{D}_b \approx 2\gamma$ . If we had considered a distribution of velocities, the resulting  $f(\Lambda_{\text{app}})$  would consist of a superposition of powerlaws of the same index but of differing dynamic range, smoothing the cutoffs at low and high  $\Lambda_{\text{app}}$ .

If the duration of the burst peak becomes smaller than  $\delta t$ , the effective peak flux is reduced from the value given by equation (B7) by the factor  $\tau/\delta t$ , where  $\tau$  is the peak duration at Earth. If the rest-frame duration is  $\tau_0$ , then beaming and redshift effects imply  $\tau = \tau_0(1+z)/\mathcal{D}$ . Using equation (B9), we can rewrite  $\mathcal{D}$  in terms of  $\Lambda_{\text{app}}$  to reveal explicitly how the observed peak duration is correlated with the luminosity (and through it, the peak flux). The result is

$$\tau(\Lambda_{\text{app}}, z) = \tau_0(1+z) \left( \frac{\Lambda_{\text{app}}}{\Lambda_0} \right)^{-\frac{1}{2+\alpha}}, \quad (\text{B14})$$

as quoted in § 7.

## REFERENCES

- Bak, P., Tang, C., & Wiesenfeld, K. 1988, *PhysRev*, A38, 364
- Cohen, E., & Piran, T. 1995, *ApJ*, 444, L25
- Dennis, B. R. 1985, *Solar Phys.*, 100, 465
- Dermer, C. D. 1992, *PRL*, 68, 1799
- Emslie, A. G., & Horack, J. M. 1994, *ApJ*, 435, 16
- Fenimore, E. E. 1996, to appear in *Gamma-Ray Bursts, Third Workshop, Huntsville, AL 1995*, (New York: AIP)
- Fenimore, E. E., Epstein, R., Ho, C., Klebesadel, R. W., & Laros, J. 1992, in *Gamma-Ray Bursts, Huntsville, AL 1991*, ed. W. S. Paciesas & G. J. Fishman (New York: AIP), 108
- Fenimore, E. E., Klebesadel, R. W., Laros, J., Lacey, C., Madras, C., Meier, M., & Schwarz, G. 1993a, in *Compton Gamma-Ray Observatory, St. Louis, MO 1992*, ed. M. Friedlander, N. Gehrels & D. J. Macomb (New York: AIP), 744
- Fenimore, E. E. et al. 1993, *Nature*, 366, 40
- Fenimore, E. E., & Bloom, J. 1996a, submitted to *ApJ*
- Fenimore, E. E., & Bloom, J. 1996b, to appear in *Gamma-Ray Bursts, Third Workshop, Huntsville, AL 1995*, (New York: AIP), in press
- Fishman et al. 1994, *ApJS*, 92, 229
- Fishman et al. 1996, *ApJS*, 106, 65
- Graziani, C. 1995, to appear in *Gamma-Ray Bursts, Third Workshop, Huntsville, AL 1995*, (New York: AIP)
- Gregory, P. C., & Lored, T. J. 1992, *ApJ*, 398, 146
- Hakkila, J., et al. 1996, *ApJ*, 462, 125
- Horack, J. M., Emslie, A. G., & Meegan, C. A. 1994, *ApJ*, 426, L5
- Horack, J. M., Hakkila, J., Emslie, A. G., & Meegan, C. A. 1996, *ApJ*, 462, 131
- Jeffreys, H. 1961, *Theory of Probability* (Oxford: Oxford University Press)
- Krolik, J. H., & Pier, E. A. 1991, *ApJ*, 373, 277
- Lamb, D. Q., Graziani, C., & Smith, I. A. 1993, *ApJ*, 413, L11

- Loredo, T. J., & Wasserman, I. M. 1993, in Compton Gamma-Ray Observatory, St. Louis, MO 1992, ed. M. Friedlander, N. Gehrels & D. J. Macomb (New York: AIP), 749
- Loredo, T. J., & Wasserman, I. M. 1995 (LW95), ApJS, 96, 261
- Loredo, T. J., & Wasserman, I. M. 1996, submitted to ApJ
- Lu, E. T., & Hamilton, R. J. 1991, ApJ, 380, L89
- Mao, S., Narayan, R., & Piran, T. 1993, ApJ, 420, 171
- Matz, S. M. 1996, OSSE gamma-ray burst data base, Northwestern University, URL:  
<http://www.astro.nwu.edu/astro/osse/bursts/index.html>
- Mészáros, P., and Mészáros, A. 1995, ApJ, 449, 9
- Mitrofanov, I. 1996, to appear in Gamma-Ray Bursts, Third Workshop, Huntsville, AL 1995, (New York: AIP)
- Norris, J., & Nermiroff, R. 1996, to appear in Gamma-Ray Bursts, Third Workshop, Huntsville, AL 1995, (New York: AIP)
- Pendleton, G. N., et al. 1992, in Gamma-Ray Bursts, Huntsville, AL 1991, ed. W. S. Paciesas & G. J. Fishman (New York: AIP), 395
- Petrosian, V., Azzam, W. J., & Efron, B. 1994, in Compton Gamma-Ray Observatory, St. Louis, MO 1992, ed. M. Friedlander, N. Gehrels & D. J. Macomb (New York: AIP), 754
- Petrosian, V., Lee, T. T., & Azzam, W. J. 1994, in Gamma-Ray Bursts, Second Workshop, Huntsville, AL 1993, ed. G. J. Fishman, J. J. Brainerd, & K. Hurley (New York: AIP), 93
- Piran, T. 1992, ApJ, 389, L45
- Press, W. H. 1978, Comments Astrophys., 7, 103
- Quashnock, J. 1996, to appear in Gamma-Ray Bursts, Third Workshop, Huntsville, AL 1995, (New York: AIP)
- Ulmer, A., & Wijers, R. A. M. J. 1995, ApJ, 439, 303
- Ulmer, A., Wijers, R. A. M. J., & Fenimore, E. E. 1995, ApJ, 440, L9
- Urry, C. M., & Shafer, R. A. 1984, ApJ, 280, 569
- Urry, C. M., & Padovani, P. 1991, ApJ, 371, 60
- Wasserman, I. 1992, ApJ, 394, 565
- Weinberg, S. 1972, Gravitation and Cosmology (New York: John Wiley & Sons)

- Wickramasinghe, W. A., Nemiroff, R. J., Norris, J. P., Kouvelioutou, C., Fishman, G. J., Meegan, C. A., Wilson, R. B., & Paciasas, W. S. 1993, *ApJ*, 411, L55
- Wijers, R., & Lubin, L. M. 1993, in *Compton Gamma-Ray Observatory, St. Louis, MO 1992*, ed. M. Friedlander, N. Gehrels & D. J. Macomb (New York: AIP), 729
- Woods, E., & Loeb, A. 1995, *ApJ*, 453, 583
- Yi, I. 1993, *Phys. Rev. D*, D48, 4518
- Yi, I. 1994, *ApJ*, 431, 543

Fig. 1.— True (solid) and approximate sky-averaged detection efficiencies for the simulated observations described in the text. Dashed curve was calculated ignoring both counting uncertainties and atmospheric scattering, as was the efficiency reported in the BATSE catalogs. Dotted curve incorporates counting uncertainties. Solid curve additionally incorporates atmospheric scattering.

Fig. 2.— a–c. Determination of cutoff flux for self-consistent analysis of simulated 64 ms data with approximate detection efficiency. Panels show scatterplots of the logarithm of the ratio of maximum likelihood for parameters of a broken power law model to the likelihood for the true parameter values, calculated using the true detection efficiency ( $\Delta L_{\text{true}}$ ) and the approximate one ( $\Delta L_{\text{approx}}$ ), analyzing all bursts (a), and only those with peak fluxes  $> 1.2$  and  $1.5 \text{ cm}^{-2} \text{ s}^{-1}$  (b, c). Results are shown for 10 simulated data sets of 400 bursts.

Fig. 3.— Posterior distributions for the power-law index,  $\gamma$ , for phenomenological power law models, based on 64 ms (solid) and 1024 ms (dashed) data. Intersections with the horizontal dotted lines indicate the 68.3% (top), 95.4% (middle), and 99.7% (bottom) credible regions.

Fig. 4.— Cumulative peak flux distributions predicted by best-fit simple power law models based on 64 ms (a) and 1024 ms (b) data. Histogram shows cumulative distribution of best-fit peak flux values of detected bursts.

Fig. 5.— Joint credible regions for break flux  $\Phi_b$  and low-flux power-law index  $\gamma_1$  in a simple broken power law model with high-flux power-law index  $\gamma_2 \equiv 2.5$ , based on 64 ms (a) and 1024 ms (b) data. Here and throughout this work contours enclose 68.3% (dotted), 95.4% (dashed), and 99.7% (solid) of the posterior probability; crosses indicate best-fit parameter values.

Fig. 6.— Cumulative peak flux distributions predicted by best-fit simple broken power law models with  $\gamma_2 \equiv 2.5$ , based on 64 ms (a) and 1024 ms (b) data. Histogram shows cumulative distribution of best-fit peak flux values of detected bursts.

Fig. 7.— Joint credible regions for break flux  $\Phi_b$  and inclination of the logarithmic differential rate at large flux,  $\theta$ , conditional on the best-fit values of the low-flux index  $\gamma_1$  in the simple broken power law model, based on 64 ms (a,  $\gamma_1 = 2.04$ ) and 1024 ms (b,  $\gamma_1 = 1.83$ ) data.

Fig. 8.— Cumulative peak flux distributions predicted by best-fit simple broken power law models, based on 64 ms (a) and 1024 ms (b) data. Histogram shows cumulative distribution of best-fit peak flux values of detected bursts.

Fig. 9.— Distribution of approximate spectral indices for burst photon number spectra, based on broadband fluence data.

Fig. 10.— Posterior distributions for dimensionless luminosity  $\nu_c$  for simple, homogeneous standard candle cosmological models, based on 64 ms (solid) and 1024 ms (dashed) data. Intersections with the horizontal dotted lines indicate the 68.3% (top), 95.4% (middle), and 99.7% (bottom) credible

regions.

Fig. 11.— Cumulative peak flux distributions predicted by best-fit homogeneous standard candle cosmological models, based on 64 ms (a) and 1024 ms (b) data. Histogram shows cumulative distribution of best-fit peak flux values of detected bursts.

Fig. 12.— Joint credible regions for dimensionless luminosity  $\nu_c$  and comoving burst rate density  $\dot{n}_0$  for simple, homogeneous standard candle cosmological models, based on 64 ms (upper contours) and 1024 ms (lower contours) data.

Fig. 13.— Distribution of redshifts of burst sources predicted by best-fit homogeneous standard candle cosmological models. Solid curves (with left axis) show the redshift distributions of all sources; dashed curves (with right axis) show those of the sources visible to BATSE. The uppermost curves are based on 64 ms data, the lowermost on 1024 ms data.

Fig. 14.— Joint credible regions for dimensionless luminosity  $\nu_c$  and cosmological density parameter  $\Omega_0$  for homogeneous standard candle cosmological models, based on 64 ms (a) and 1024 ms (b) data.

Fig. 15.— Joint credible regions for dimensionless luminosity  $\nu_c$  and density function power law index  $\beta$  for standard candle cosmological models with  $(1+z)^{-\beta}$  density evolution, based on 64 ms (a) and 1024 ms (b) data. Crosses indicate best-fit points, dots indicate representative points used for redshift distributions shown in Fig. 18.

Fig. 16.— Cumulative peak flux distributions predicted by best-fit standard candle cosmological models with density evolution, based on 64 ms (a) and 1024 ms (b) data. Histogram shows cumulative distribution of best-fit peak flux values of detected bursts.

Fig. 17.— Joint credible regions for dimensionless luminosity  $\nu_c$  and comoving burst rate density  $\dot{n}_0$  for standard candle cosmological models with  $(1+z)^{-\beta}$  density evolution, based on 64 ms (upper contours) and 1024 ms (lower contours) data. These are conditional on a power law index of  $\beta = -2.5$ .

Fig. 18.— Distribution of redshifts of burst sources as predicted by representative standard candle cosmological models with density evolution in the 95.4% credible regions. Solid curves (with left axis) show the redshift distributions of all sources; dashed curves (with right axis) show those of the sources visible to BATSE. The uppermost curves are based on 64 ms data, the lowermost on 1024 ms data. Models have parameter values indicated by dots in Fig. 15.

Fig. 19.— Profile likelihood functions as a function of power-law luminosity function dynamic range,  $\rho$ , based on 64 ms (solid) and 1024 ms (dashed) data.

Fig. 20.— Joint credible regions for maximum luminosity parameter  $\nu_u$  and power law index  $p$  for cosmological models with bounded power law luminosity functions, based on 64 ms (a) and

1024 ms (b) data. Crosses indicate best-fit points, dots indicate representative points used for redshift distributions shown in Fig. 23.

Fig. 21.— Cumulative peak flux distributions predicted by best-fit cosmological models with power law luminosity functions, based on 64 ms (a) and 1024 ms (b) data. Histogram shows cumulative distribution of best-fit peak flux values of detected bursts.

Fig. 22.— Joint credible regions for dimensionless luminosity  $\nu_c$  and comoving burst rate density  $\dot{n}_0$  for cosmological models with power-law luminosity functions, based on 64 ms (upper contours) and 1024 ms (lower contours) data. These are conditional on a power law index of  $p = 1.9$ .

Fig. 23.— As Fig. 18, but for representative cosmological models with power law luminosity functions indicated by dots in Fig. 20.

Fig. 24.— Profile likelihood functions as a function of dynamic range,  $\rho$ , of a “top hat” luminosity function, based on 64 ms (solid) and 1024 ms (dashed) data.

Fig. 25.— Differential burst rate for best-fit homogeneous standard candle model (short dashed), and “top hat” luminosity function models with a dynamic range of 2 (long dashed) and  $10^4$  (solid); based on 1024 ms data.

Fig. 26.— Effective luminosity functions for best-fit cosmological models with bounded power-law intrinsic luminosity functions. Solid curve (with left axis) shows luminosity function, dashed curve (right axis) shows its logarithmic slope. (a) For 64 ms data; intrinsic luminosity function has power law index  $p = 2.12$ . (b) For 1024 ms data; intrinsic luminosity function has power law index  $p = 1.68$ .

Fig. 27.— Effective luminosity functions for 1024 ms data based on cosmological models with bounded power-law intrinsic luminosity functions. Shown are the effective luminosity functions for the best-fit model (solid curve;  $p = 1.68$ ) and two other models in the 68.3% credible region of Fig. 20b: a low luminosity model with  $p = 1.0$  and  $\nu_u = 1$  (dotted curve) and a high luminosity model with  $p = 2.2$  and  $\nu_u = 300$ . Dots bound the regions containing the 90% most probable luminosities; the 90% region is bounded on the left by the lower cutoff for the solid and dashed curves.

Fig. 28.— Differential burst rates for duration-dependent broken power law model with intrinsic power law index  $\gamma_1 = 1.9$ , duration-flux power law index  $\sigma = 0.6$ , and fiducial duration  $\tau_0 = 2$  s, for 64 ms (solid) and 1024 ms (dashed) measuring timescales, illustrating effect of peak dilution.

Fig. 29.— Cumulative peak flux distributions predicted by best-fit duration-dependent broken power law models, based on 64 ms (a) and 1024 ms (b) data. Histogram shows cumulative distribution of best-fit peak flux values of detected bursts.

Fig. 30.— OSSE light curves for the brightest bursts in the 1024 ms catalog used in these analyses.

Insets detail a 1.5 s duration including the peak.

Fig. 31.— Joint credible regions for  $\tau_0$  and  $\sigma$  conditional on the best-fit values of  $\gamma_1$  in the duration-dependent broken power law model, based on 64 ms (a,  $\gamma_1 = 2.1$ ) and 1024 ms (b,  $\gamma_1 = 1.8$ ) data. Only contours bounding the 95.4% (dashed) and 99.7% (solid) credible regions are shown.

Fig. 32.— Joint credible regions for dimensionless rest-frame luminosity  $\nu_0$  and rest-frame duration  $\tau_0$  of standard candle, standard clock cosmological models with relativistic beaming, conditional on a Doppler factor of  $\mathcal{D}_b = 4$ , based on 64 ms (a,  $\gamma_1 = 2.1$ ) and 1024 ms (b,  $\gamma_1 = 1.8$ ) data.

Fig. 33.— Cumulative peak flux distributions predicted by best-fit standard candle, standard clock cosmological models with relativistic beaming, based on 64 ms (a) and 1024 ms (b) data. Histogram shows cumulative distribution of best-fit peak flux values of detected bursts.

Table 1. Simple Phenomenological Models

Quantity	64 ms Results	1024 ms Results
<i>M</i> <sub>1</sub> : Single Power Law		
$\gamma$	2.11	1.90
$R_{11}$	$\equiv 1.0$	$\equiv 1.0$
$B_{11}$	$\equiv 1.0$	$\equiv 1.0$
<i>M</i> <sub>2</sub> : Broken Power Law, $\gamma_2 \equiv 2.5$		
$\gamma_1$	2.00	1.67
$\Phi_b$ (cm <sup>-2</sup> s <sup>-1</sup> )	$1.6 \times 10^2$	12
$R_{21}$	1.3	48
$p(> R_{21})$	0.48	$5 \times 10^{-3}$
$B_{21}$	0.54	20
<i>M</i> <sub>3</sub> : Broken Power Law		
$\gamma_1$	2.04	1.83
$\Phi_b$ (cm <sup>-2</sup> s <sup>-1</sup> )	$1.2 \times 10^2$	43
$\gamma_2$	4.3	15
$R_{31}$	3.6	$1.7 \times 10^3$
$p(> R_{31})$	0.28	$6 \times 10^{-4}$
$B_{31}$	4.7	19

Table 2. Simple Cosmological Models With  $\Omega_0 = 1$

Quantity	64 ms Results	1024 ms Results
<i>M</i> <sub>4</sub> : Homogeneous Standard Candles		
$\nu_c$	0.37	0.44
$\dot{n}_0$ (yr <sup>-1</sup> Gpc <sup>-3</sup> )	53	24
$R_{41}$	0.22	7.2
$p(> R_{41})$	...	...
$B_{41}$	0.24	5.9
<i>M</i> <sub>5</sub> : Inhomogeneous Standard Candles		
$\nu_c$	$3.3 \times 10^2$	$1.0 \times 10^1$
$\beta$	-3.0	-2.1
$\dot{n}_0$ (yr <sup>-1</sup> Gpc <sup>-3</sup> )	$5.8 \times 10^{-3}$	0.40
$R_{54}$	5.6	3.7
$p(> R_{54})$	$6.4 \times 10^{-2}$	0.11
$B_{54}$	1.3	1.0
<i>M</i> <sub>6</sub> : Power Law Luminosity Function		
$\nu_u$	25.1	4.84
$p$	2.12	1.68
$\rho$	$\equiv 10^4$	$\equiv 10^4$
$\dot{n}_0$ (yr <sup>-1</sup> Gpc <sup>-3</sup> )	$2.0 \times 10^3$	$7.2 \times 10^2$
$R_{64}$	5.5	4.4
$p(> R_{64})$	$6.5 \times 10^{-2}$	$3.0 \times 10^{-3}$
$B_{64}$	1.3	0.92

Table 3. Duration-Dependent Models

Quantity	64 ms Results	1024 ms Results
<i>M</i> <sub>7</sub> : Broken Power Law/Top Hat		
$\gamma_1$	2.1	1.8
$\sigma$	0.36	0.996
$\tau_0$ (s)	0.16	40
$R_{71}$	18	$6.0 \times 10^3$
$p(> R_{71})$	$5.7 \times 10^{-2}$	$1.7 \times 10^{-4}$
$B_{71}$	$\approx 0.3$	$\approx 5$
<i>M</i> <sub>8</sub> : Cosmological Beamed Sources		
$\nu_0$	$8.7 \times 10^{-3}$	0.60
$\tau_0$ (s)	0.73	0.18
$\mathcal{D}_b$	$\equiv 4$	$\equiv 4$
$R_{84}$	1.8	1.2
$p(> R_{84})$	0.27	0.52
$B_{84}$	1.1	1.3

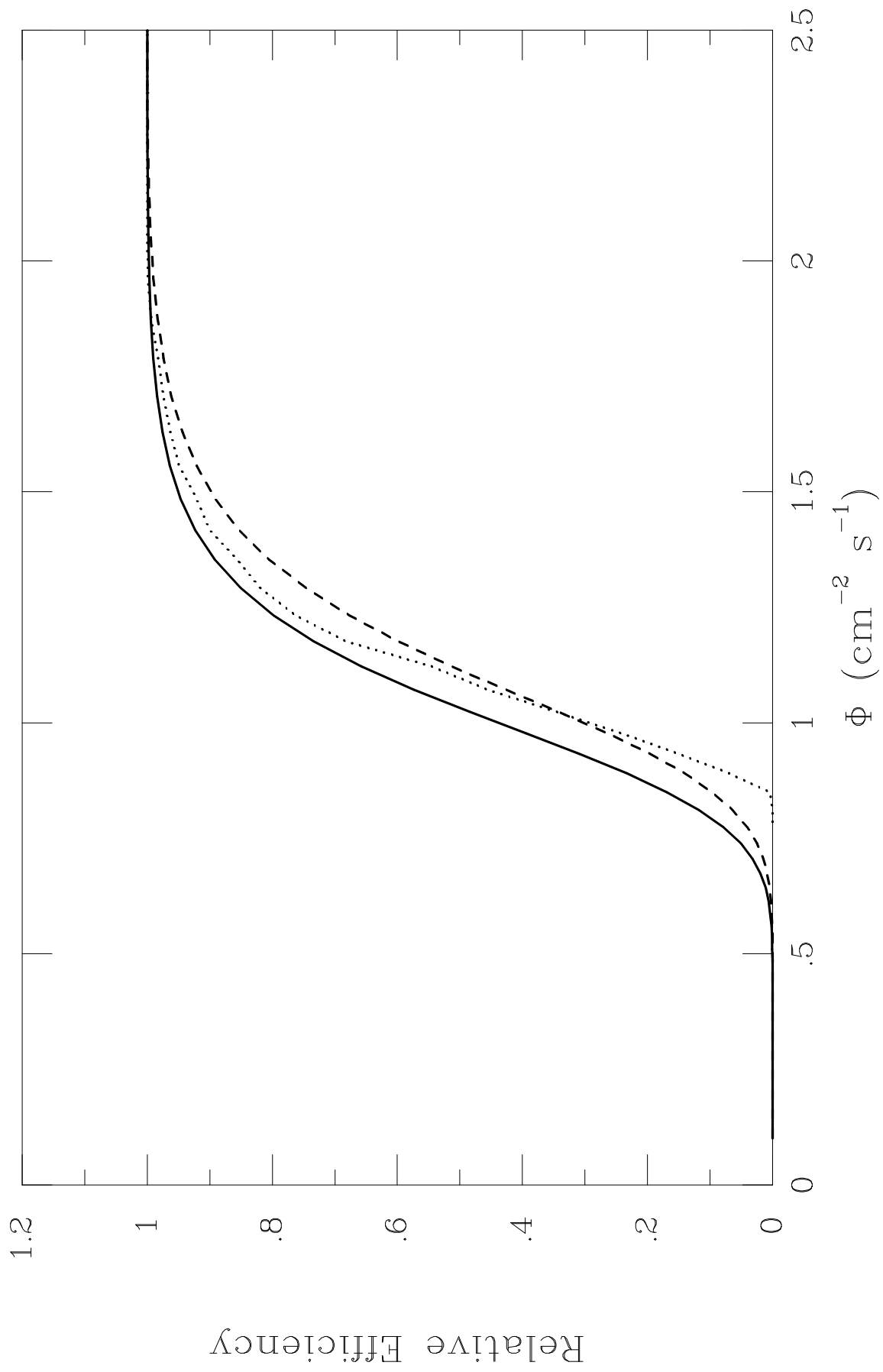


Figure 1

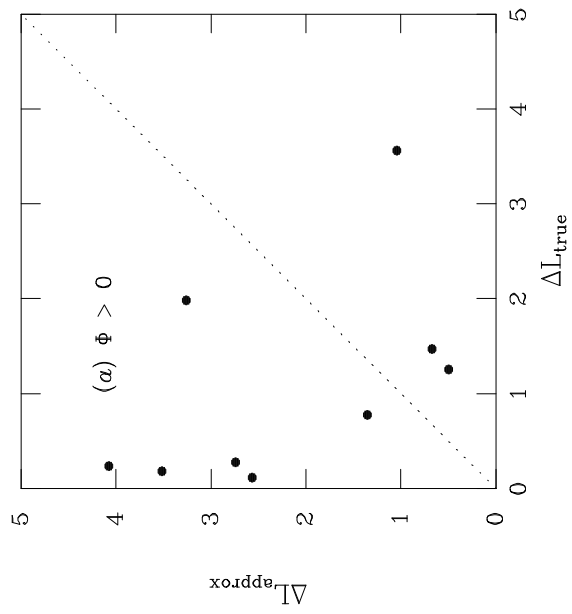
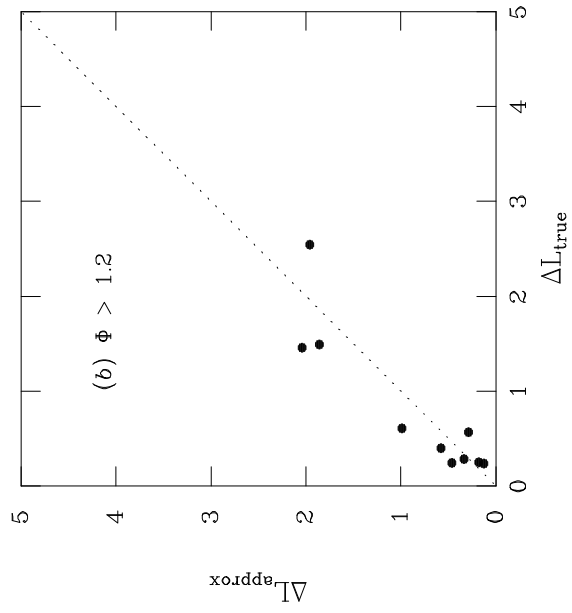
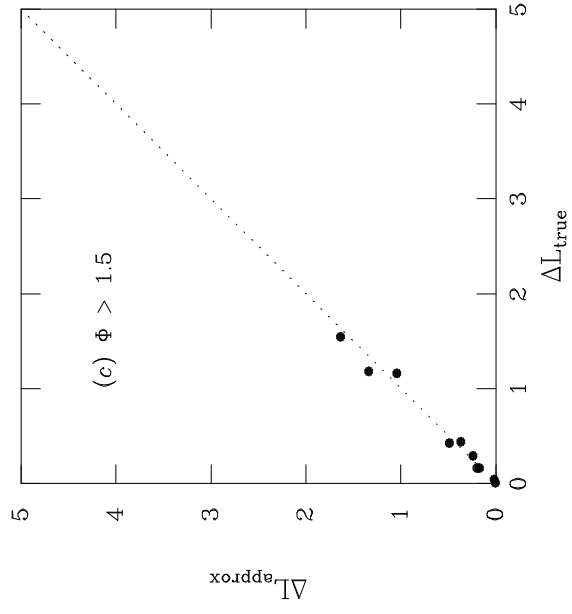


Figure 2

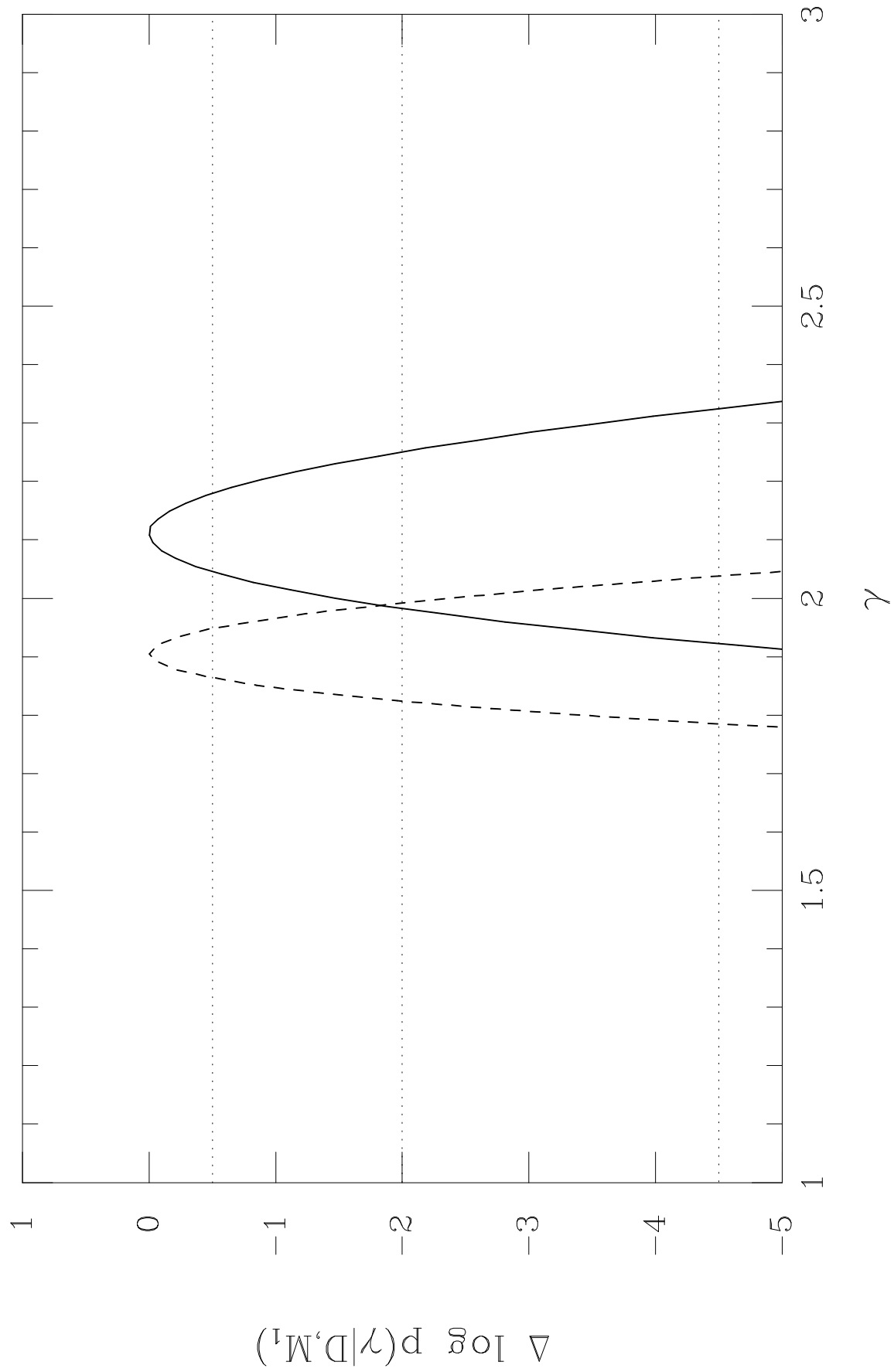


Figure 3

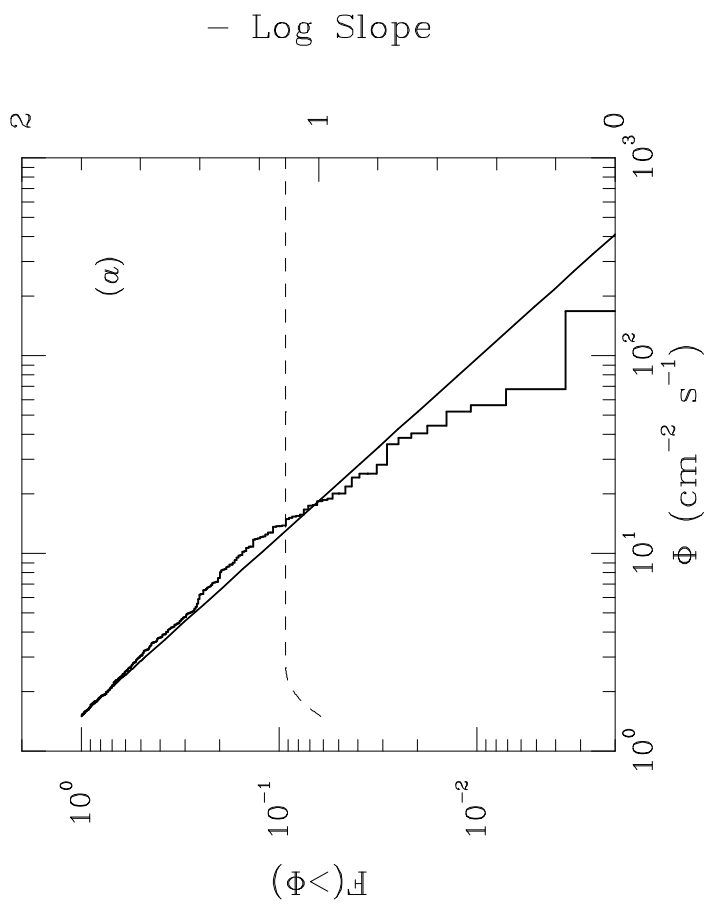
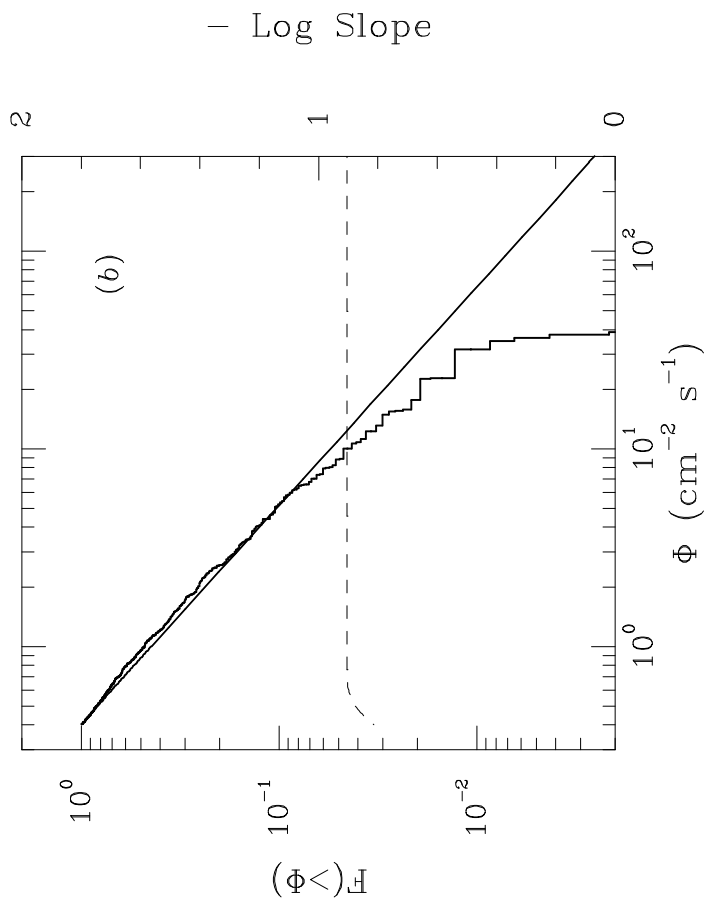


Figure 4

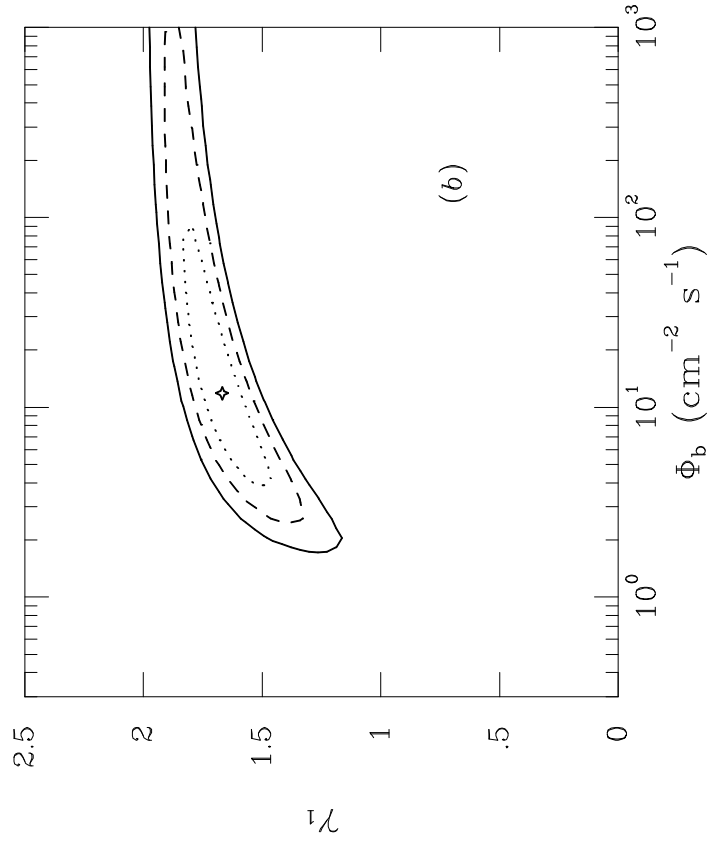
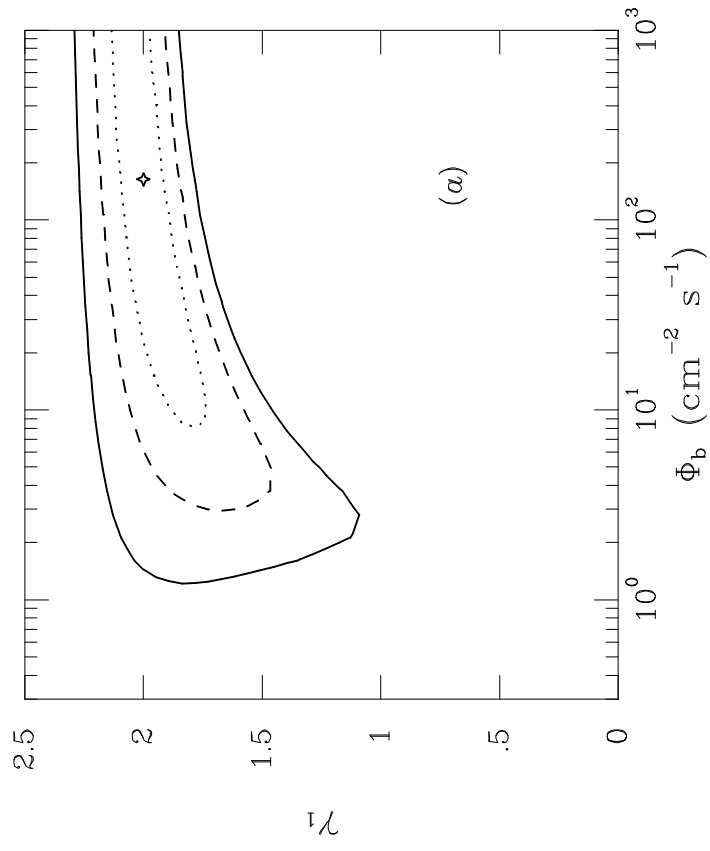


Figure 5

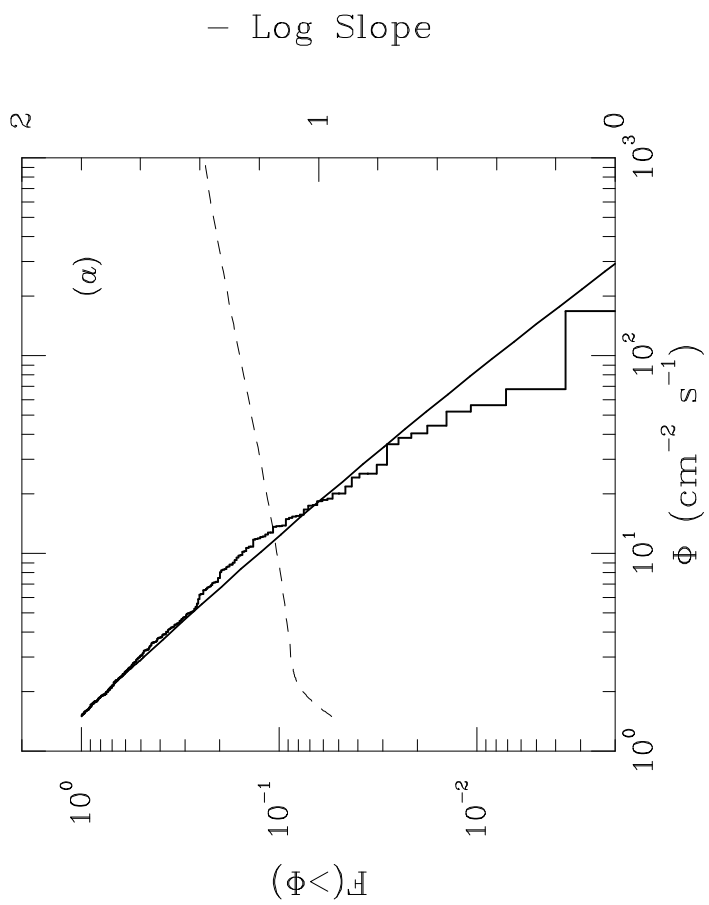
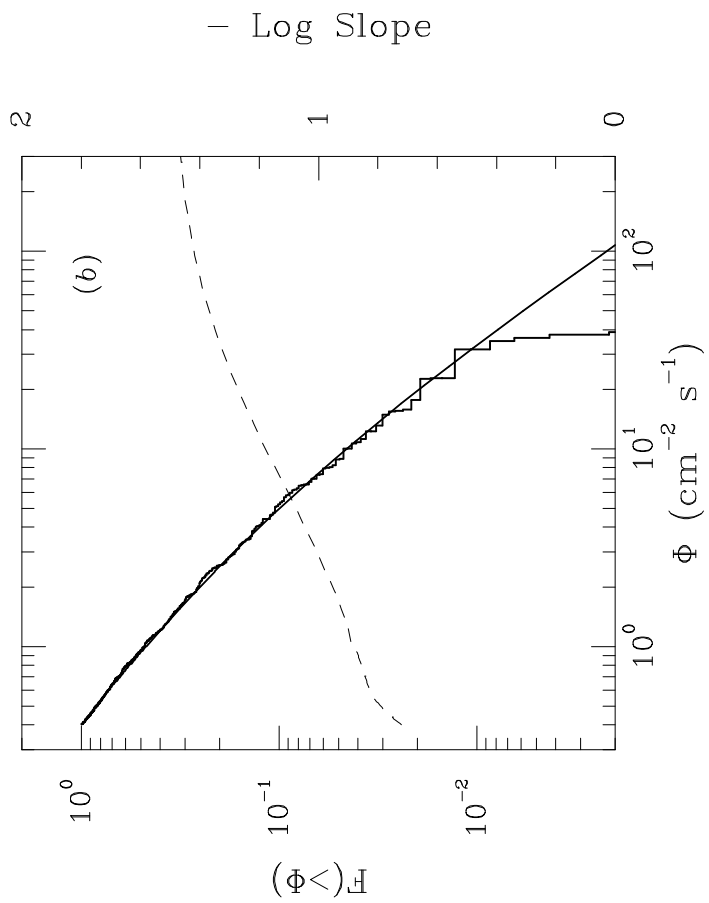


Figure 6

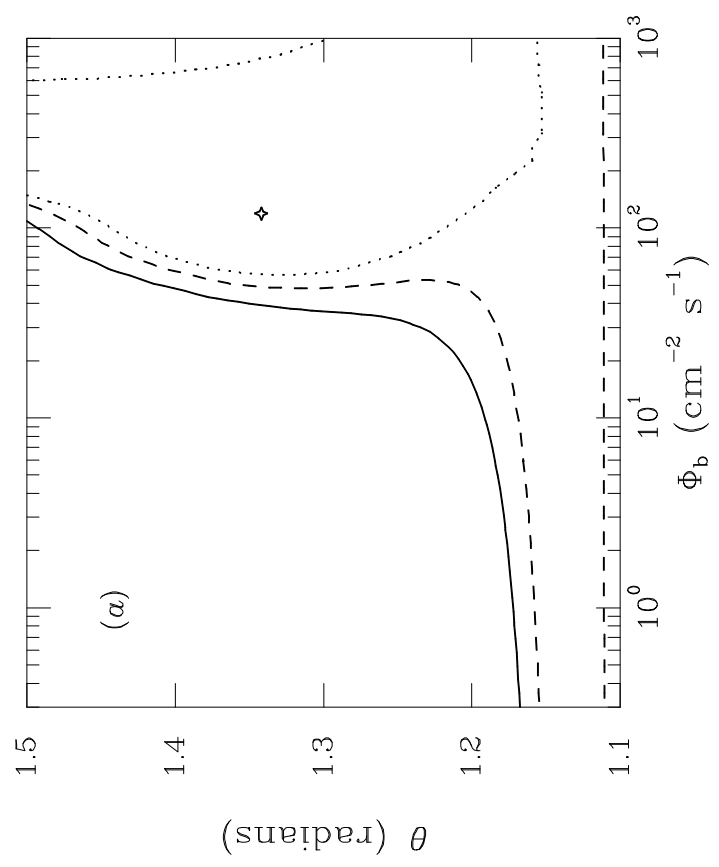
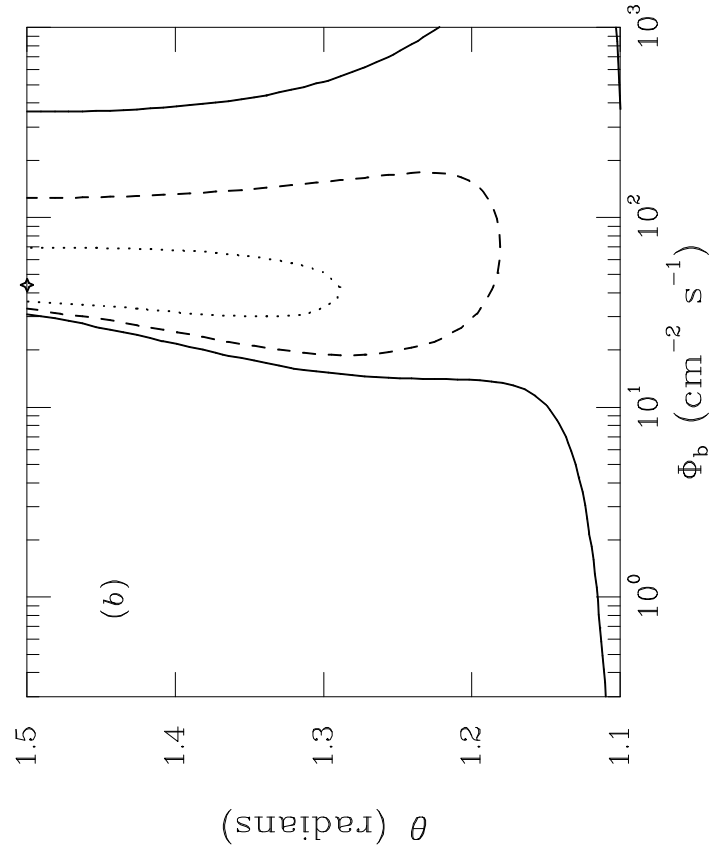


Figure 7

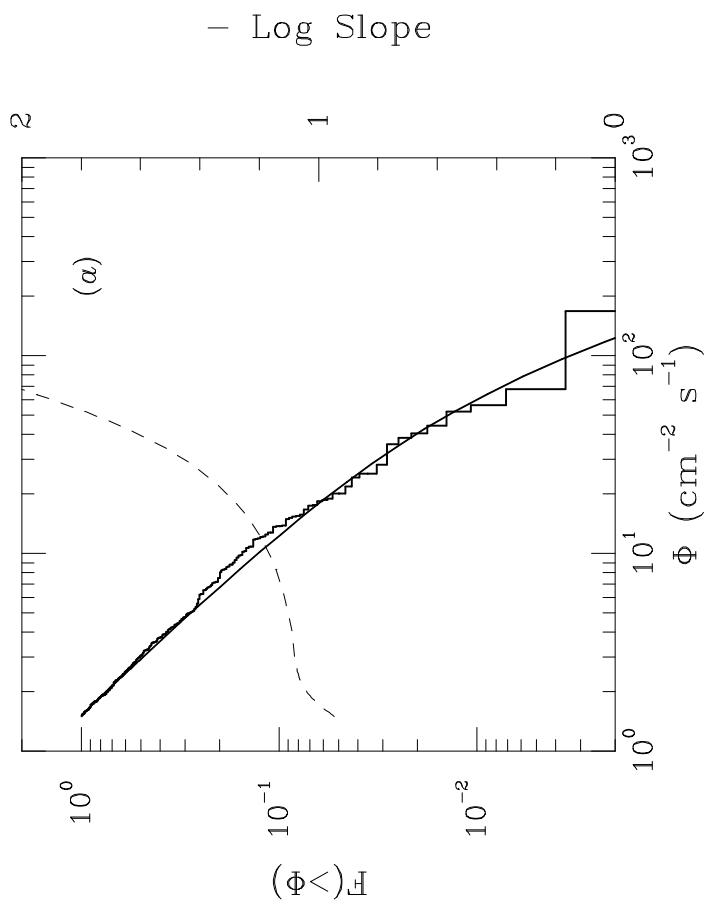
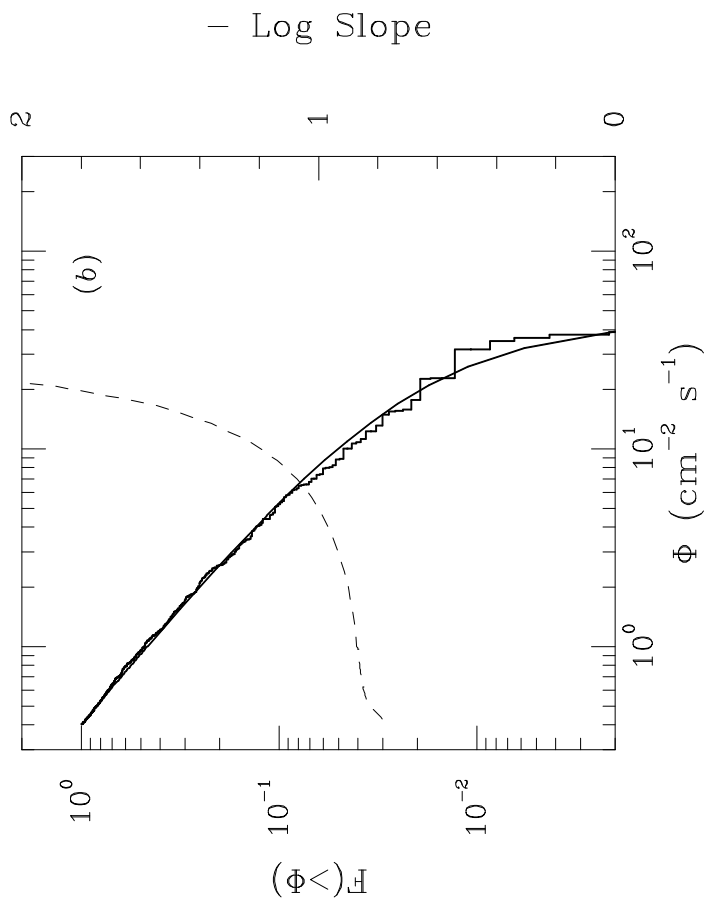


Figure 8

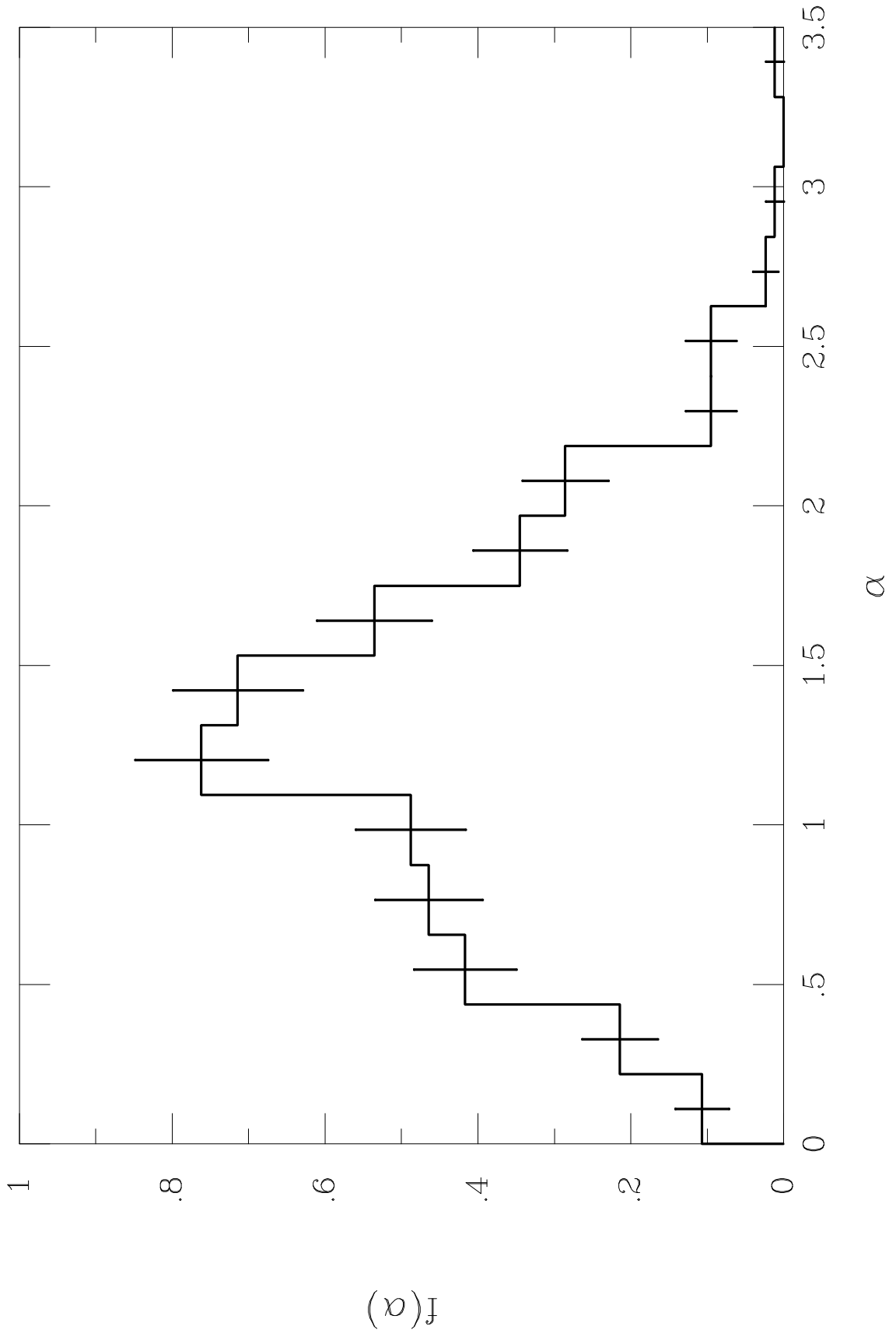


Figure 9

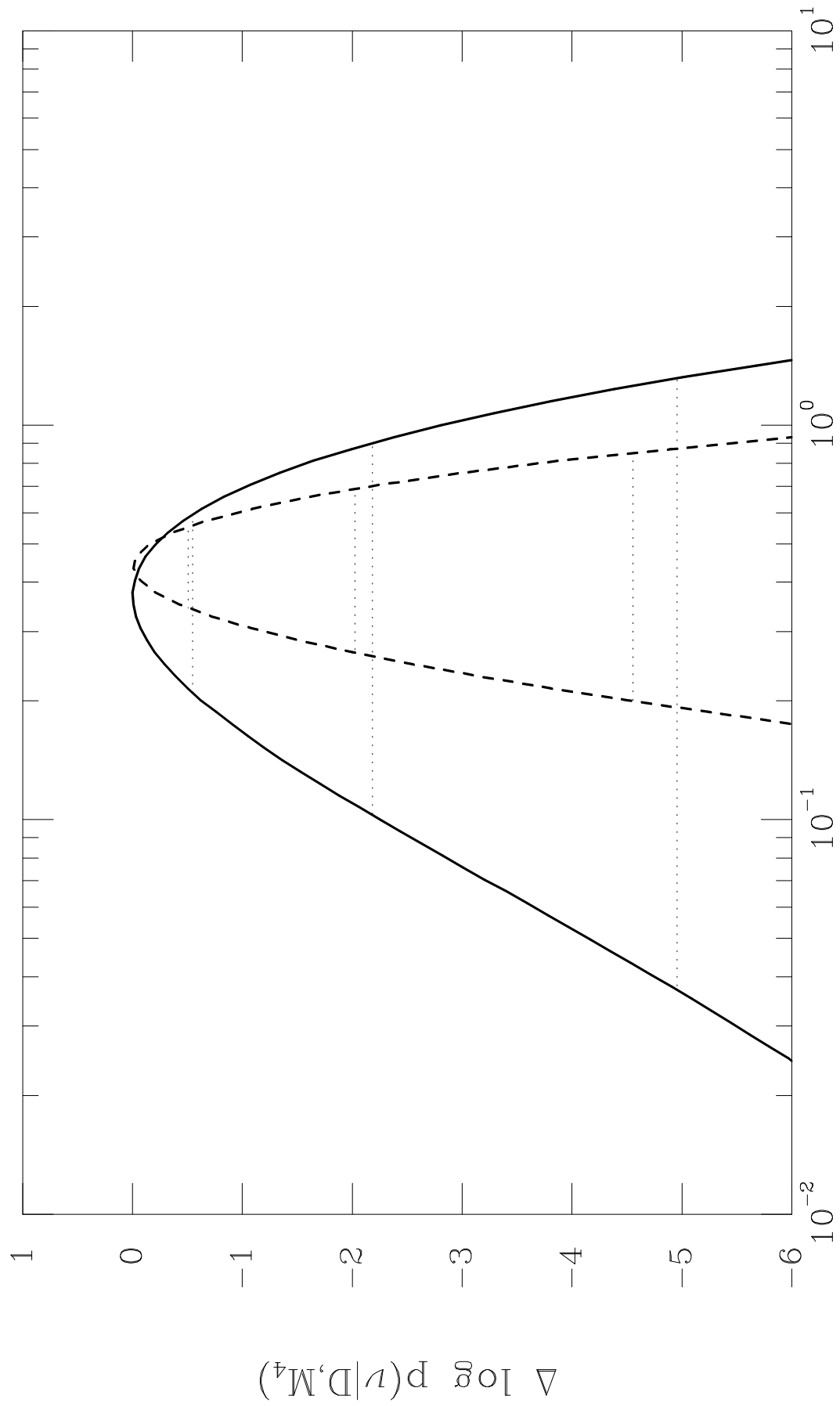


Figure 10

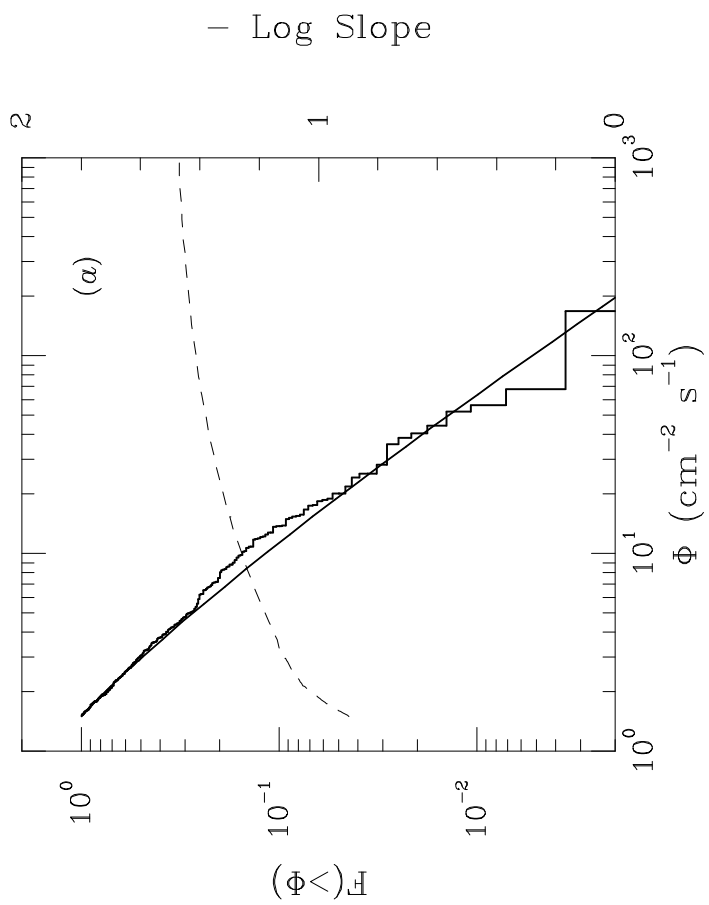
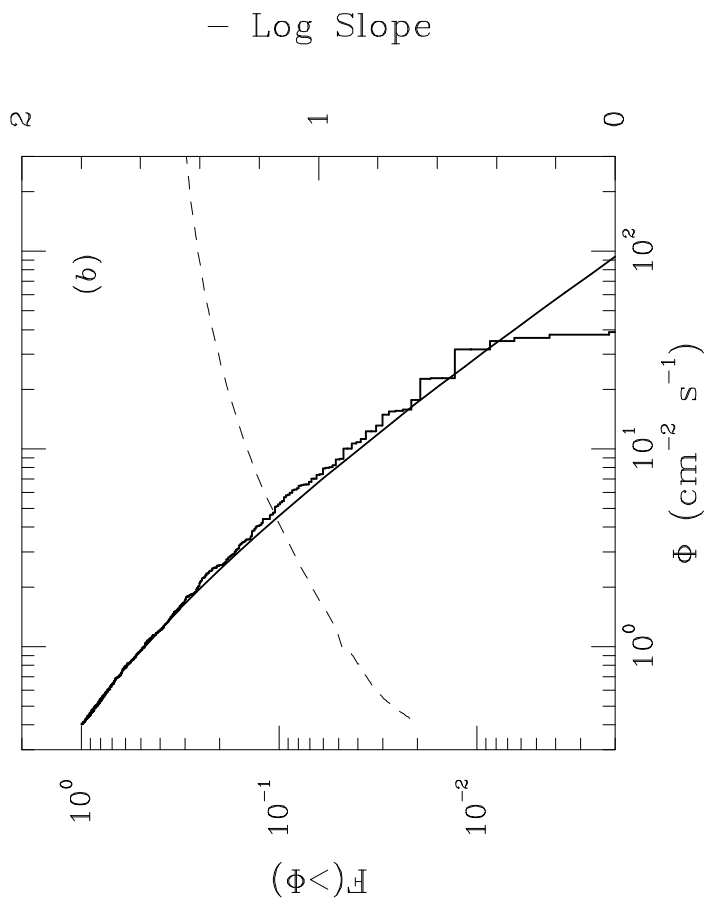


Figure 11

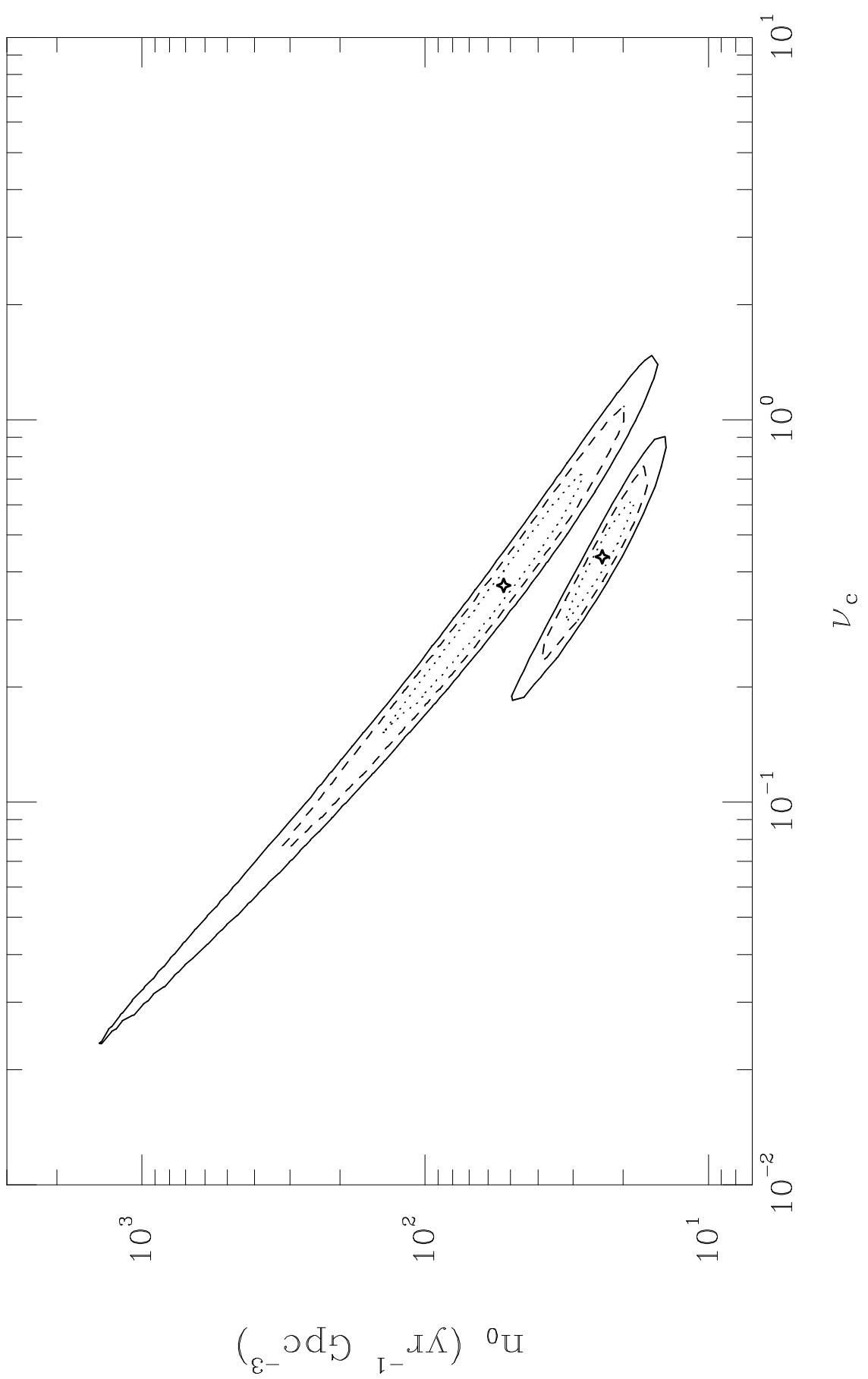


Figure 12

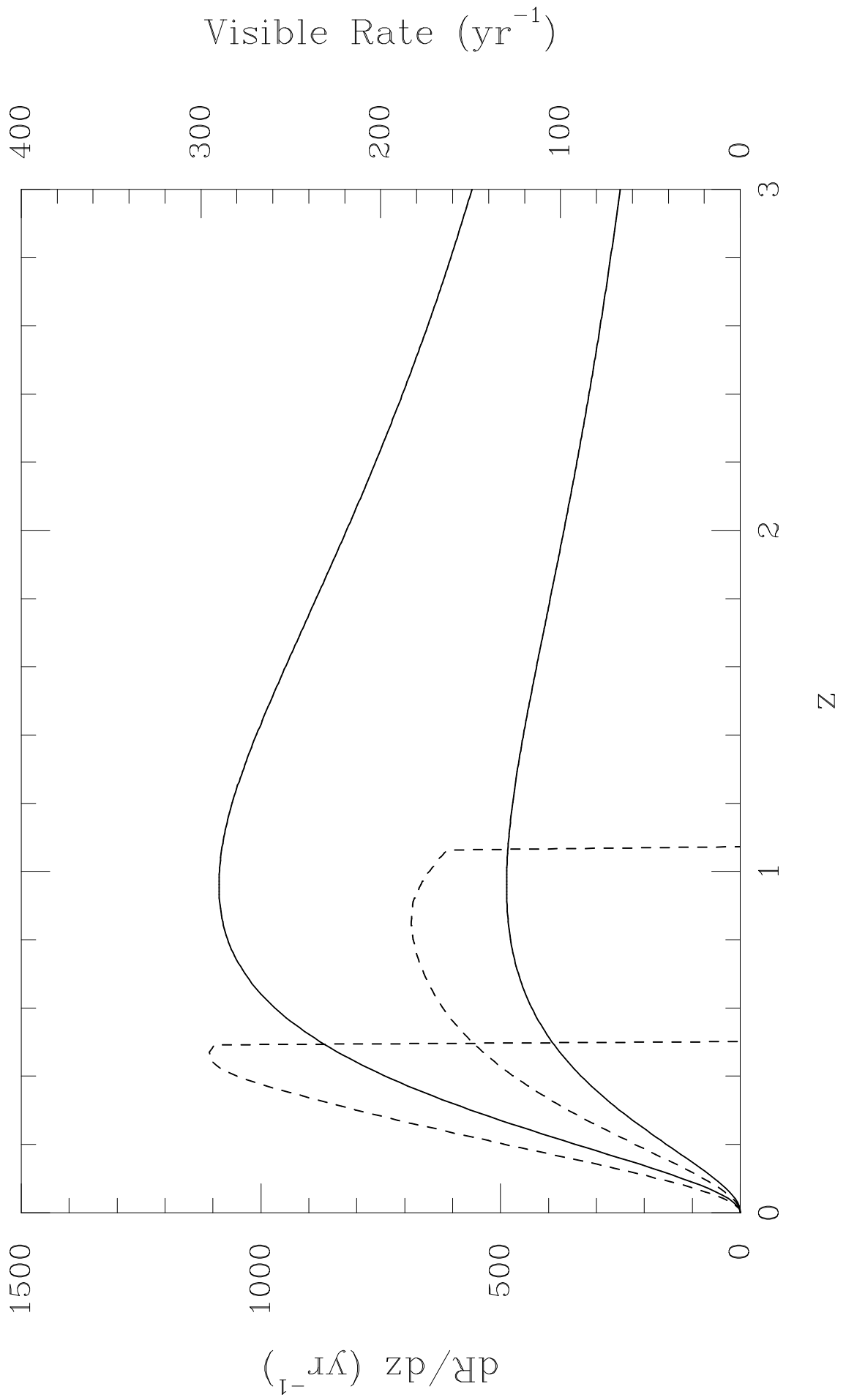


Figure 13

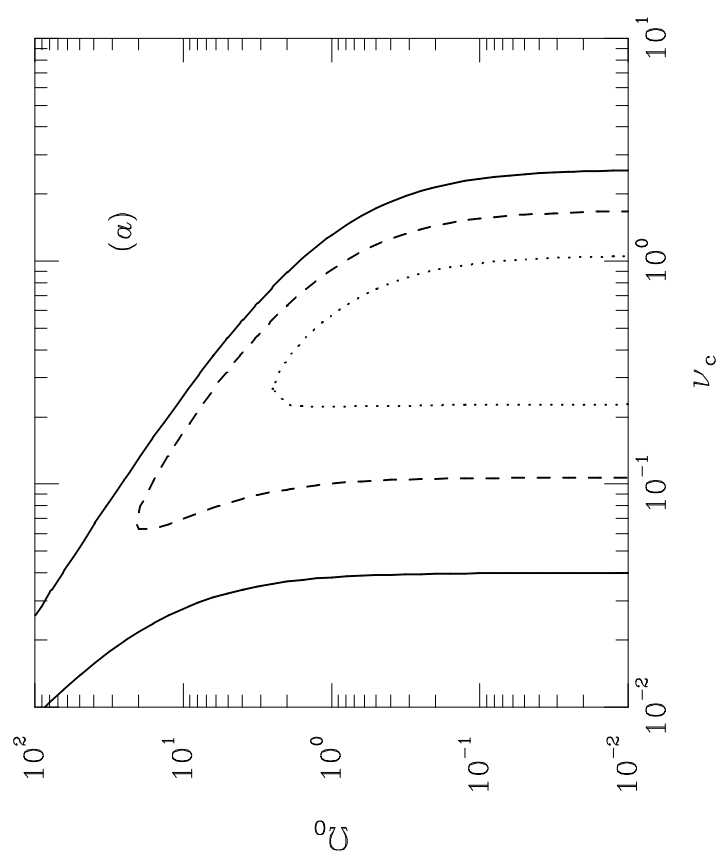
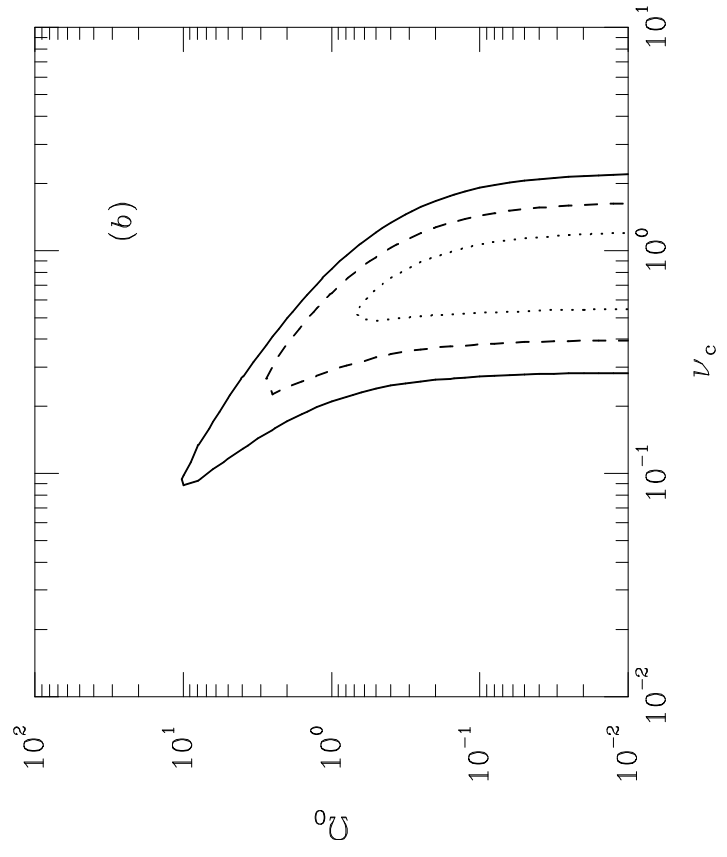


Figure 14

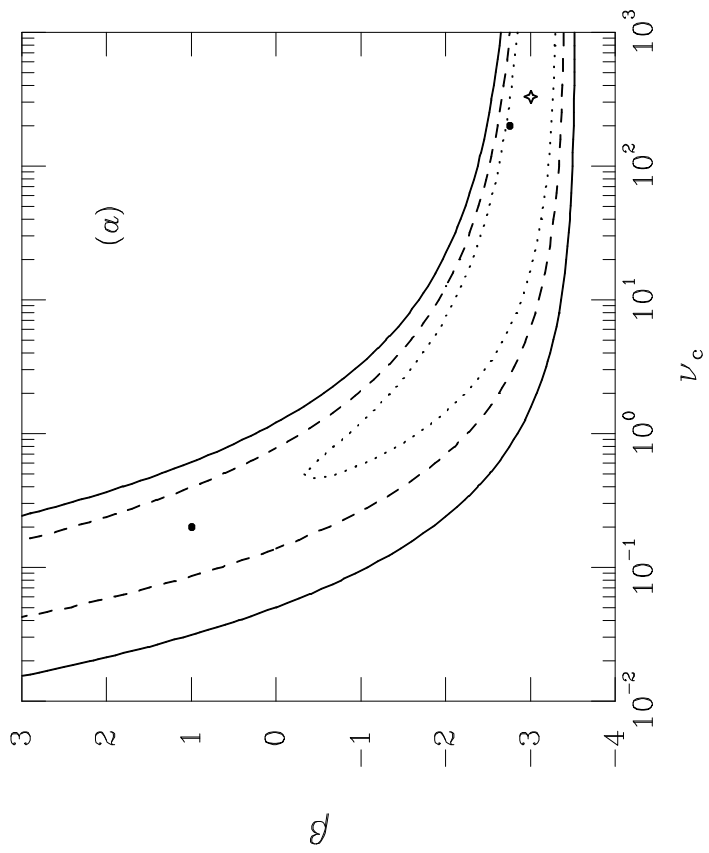
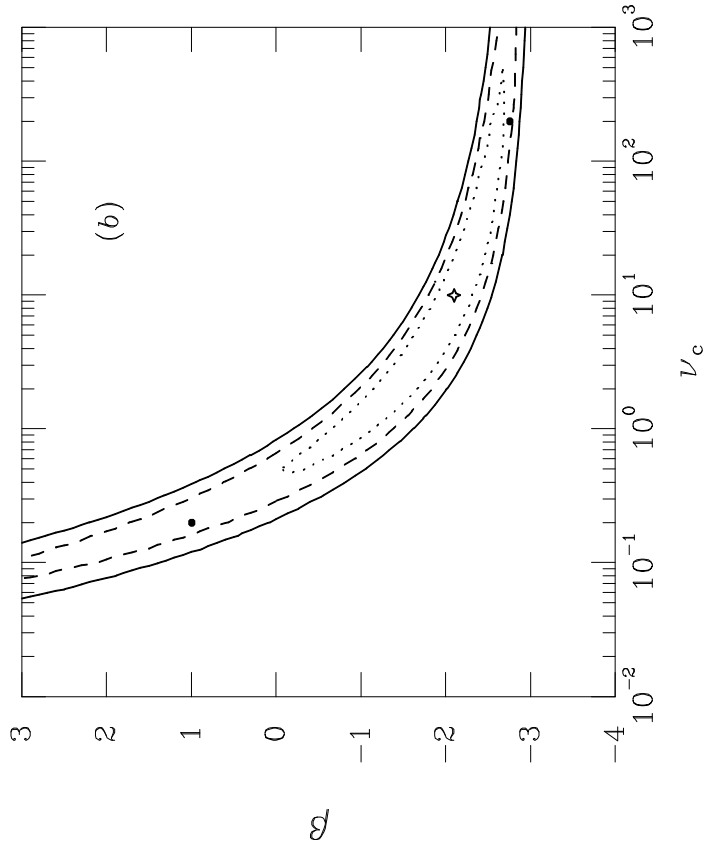


Figure 15

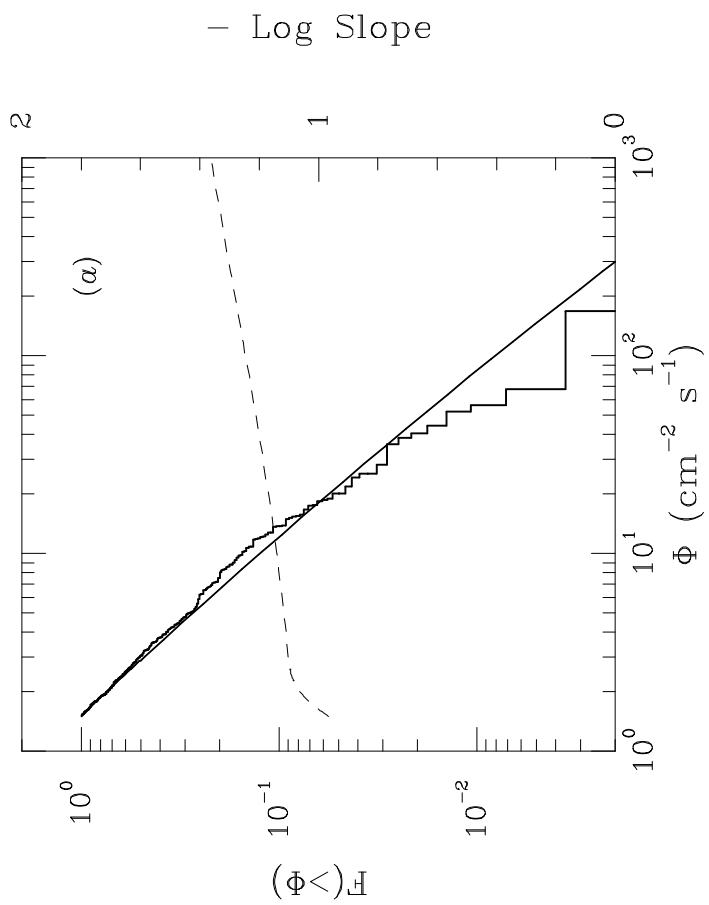
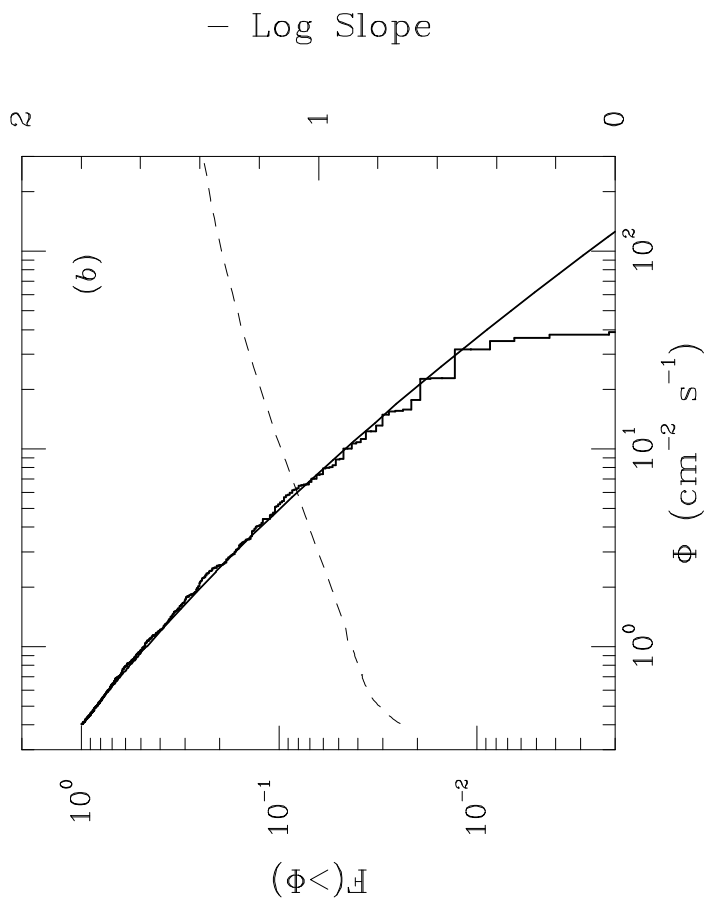


Figure 16

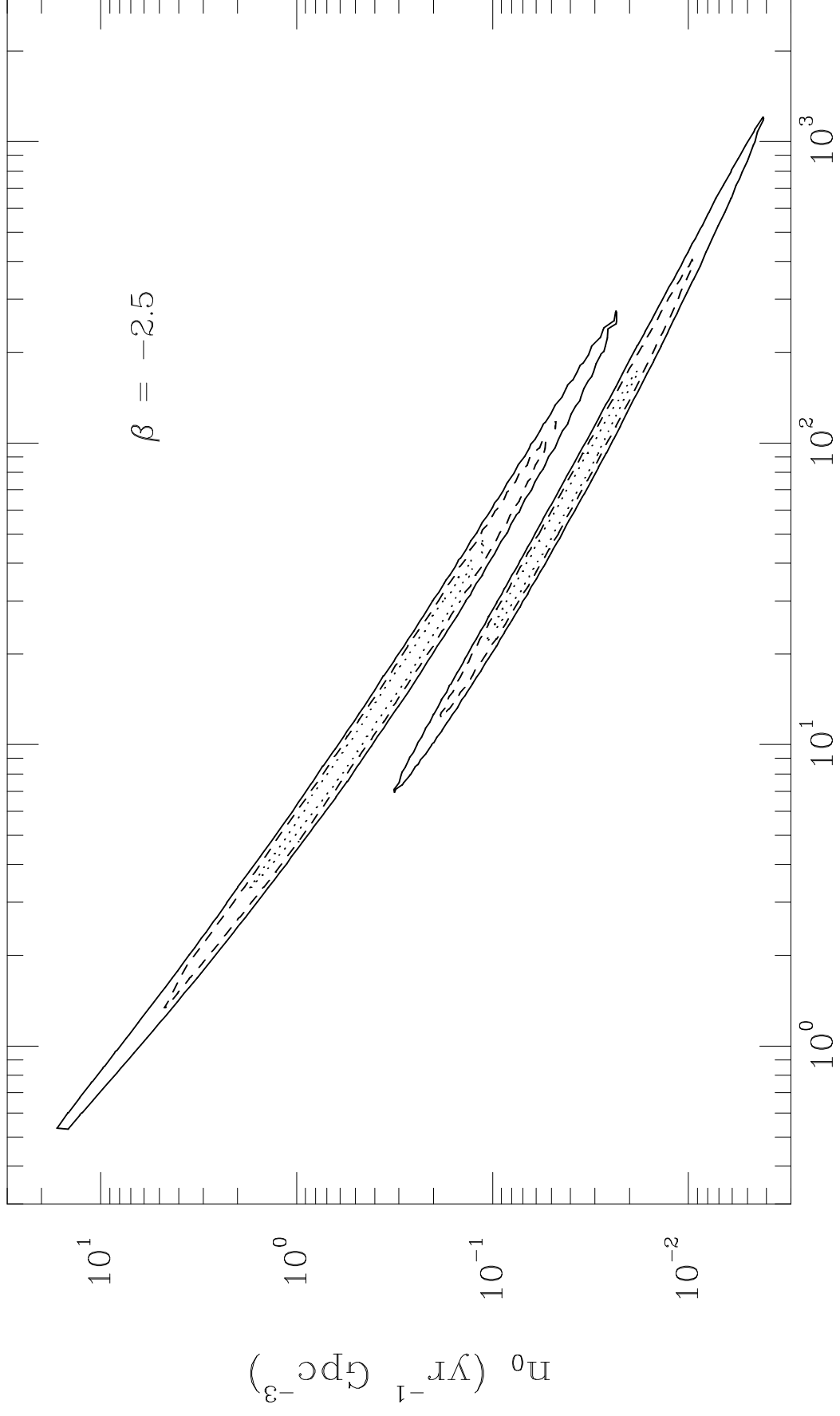


Figure 17

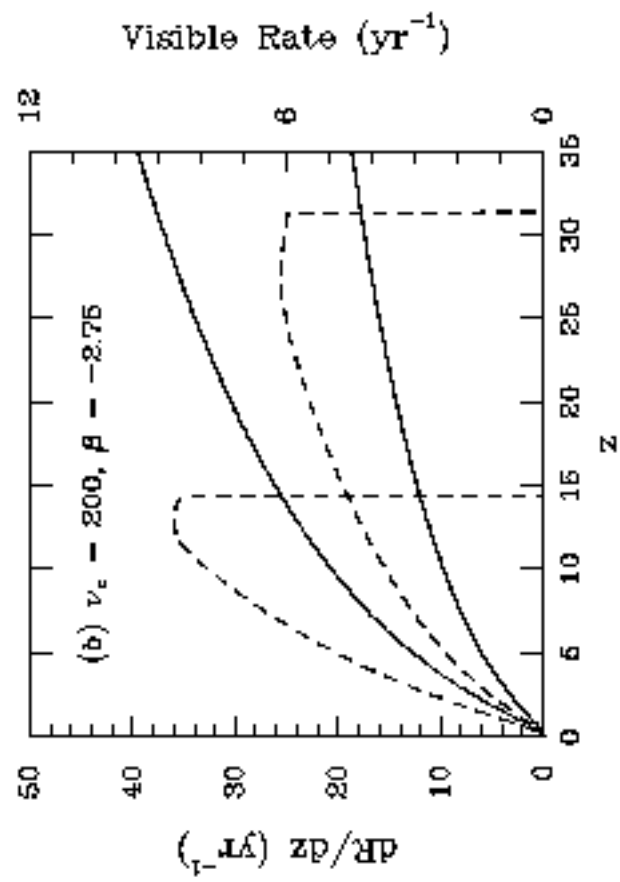
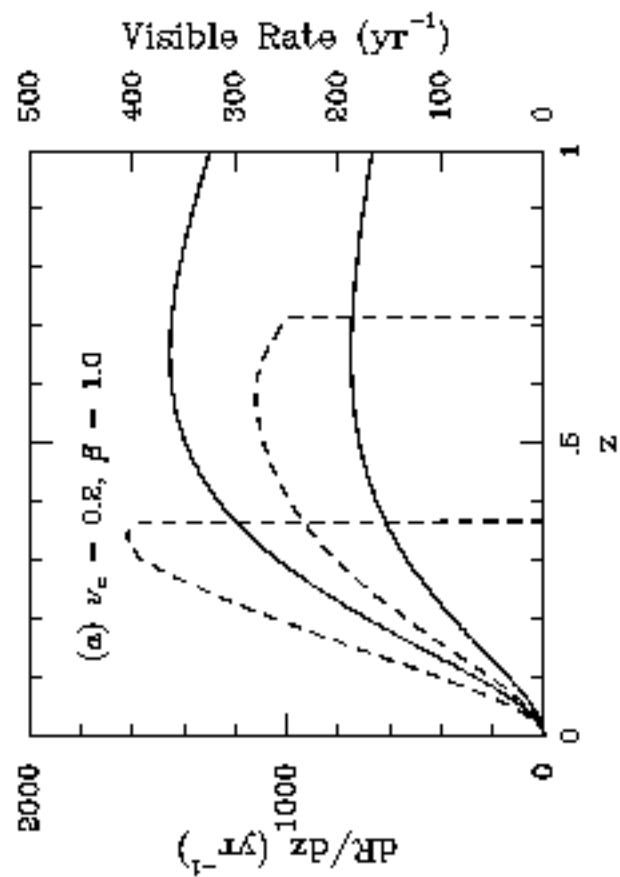


Figure 18

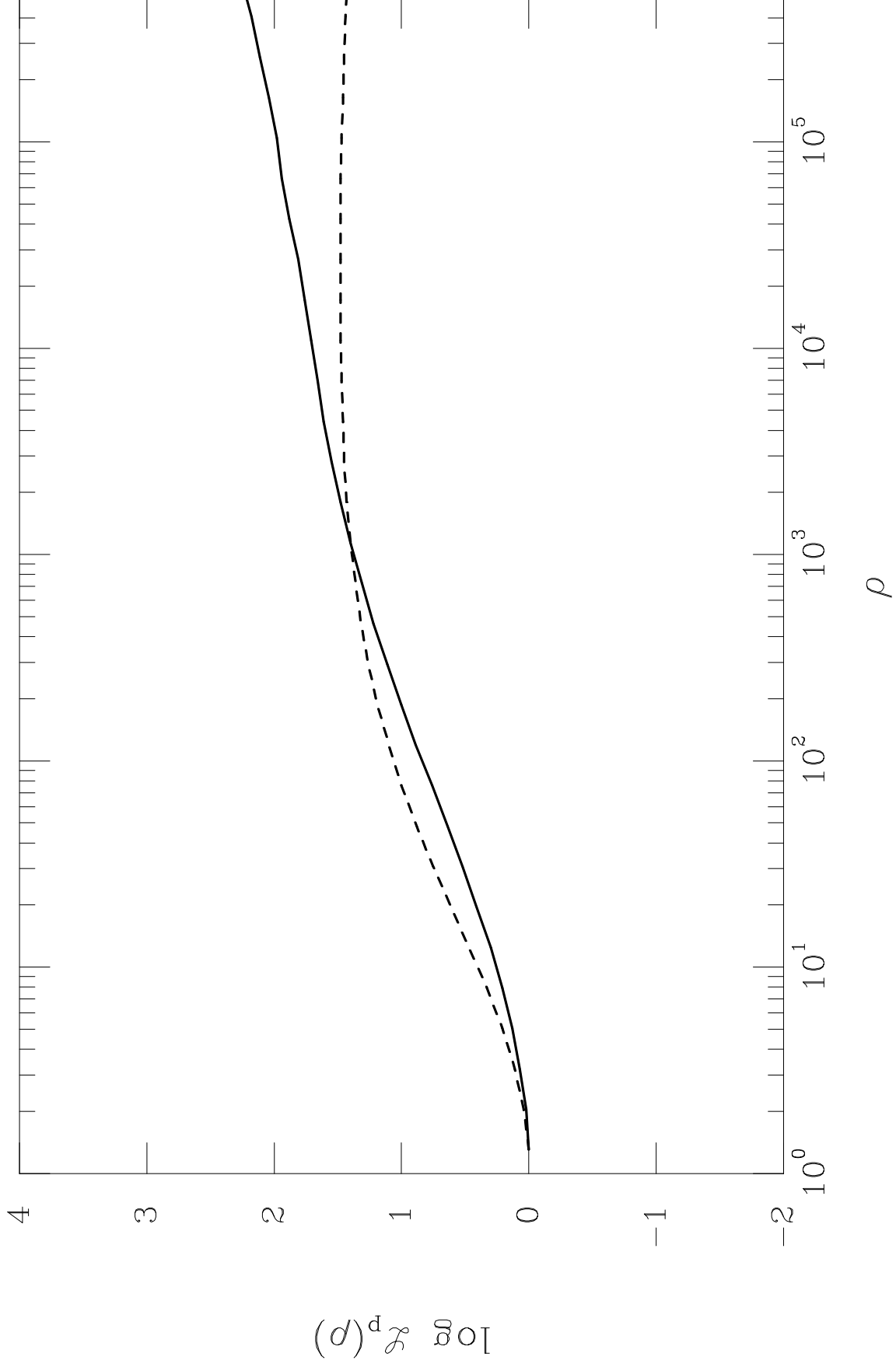


Figure 19

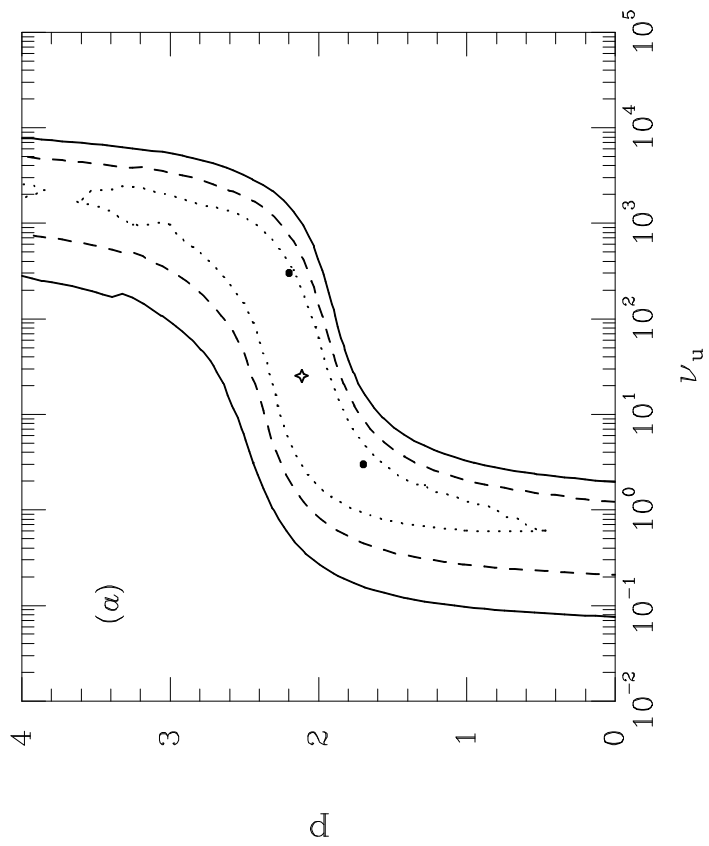
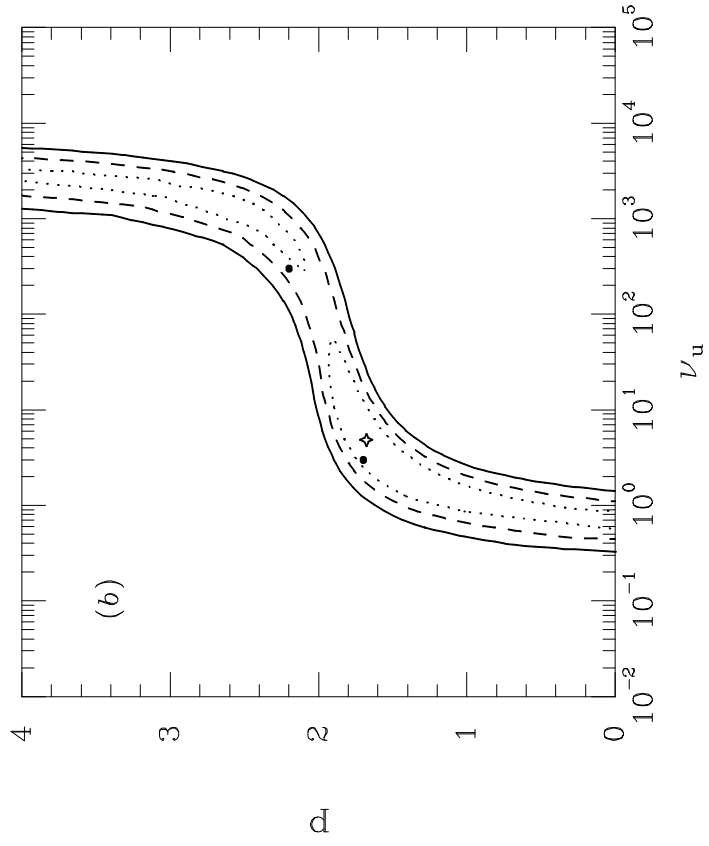


Figure 20

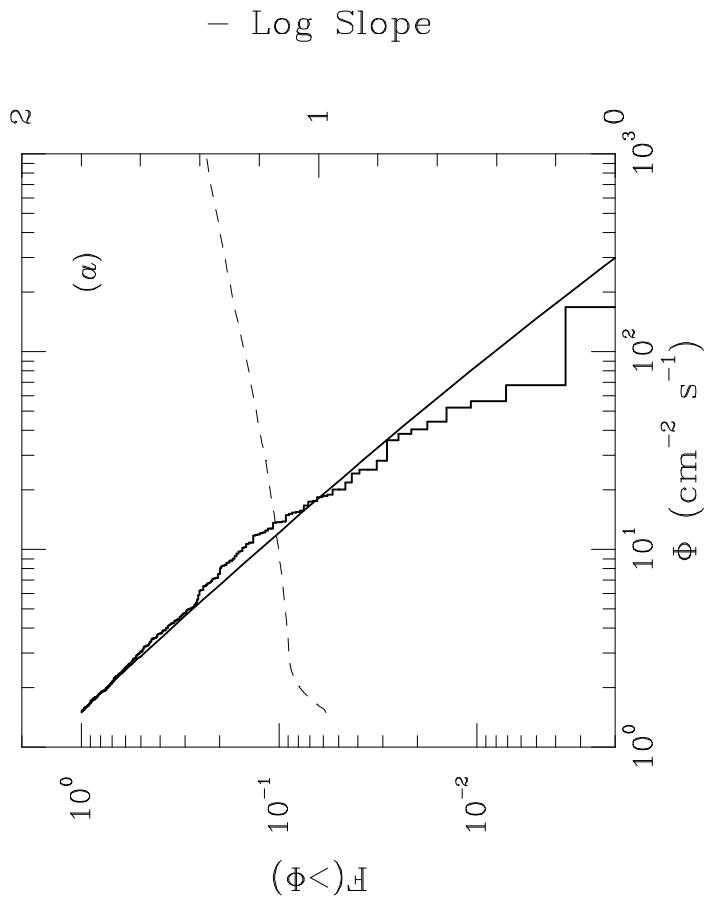
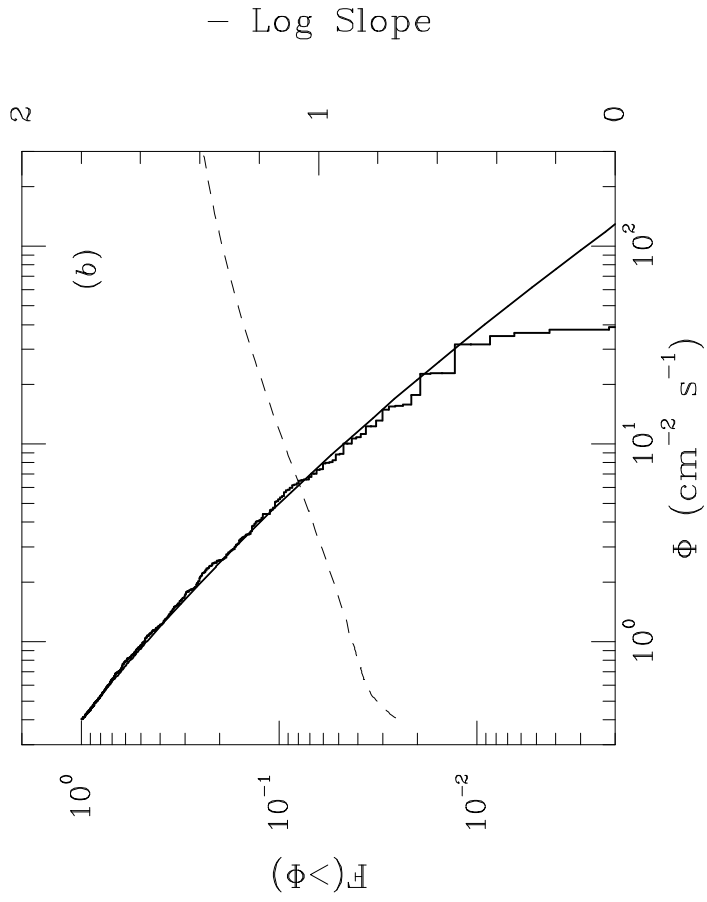


Figure 21

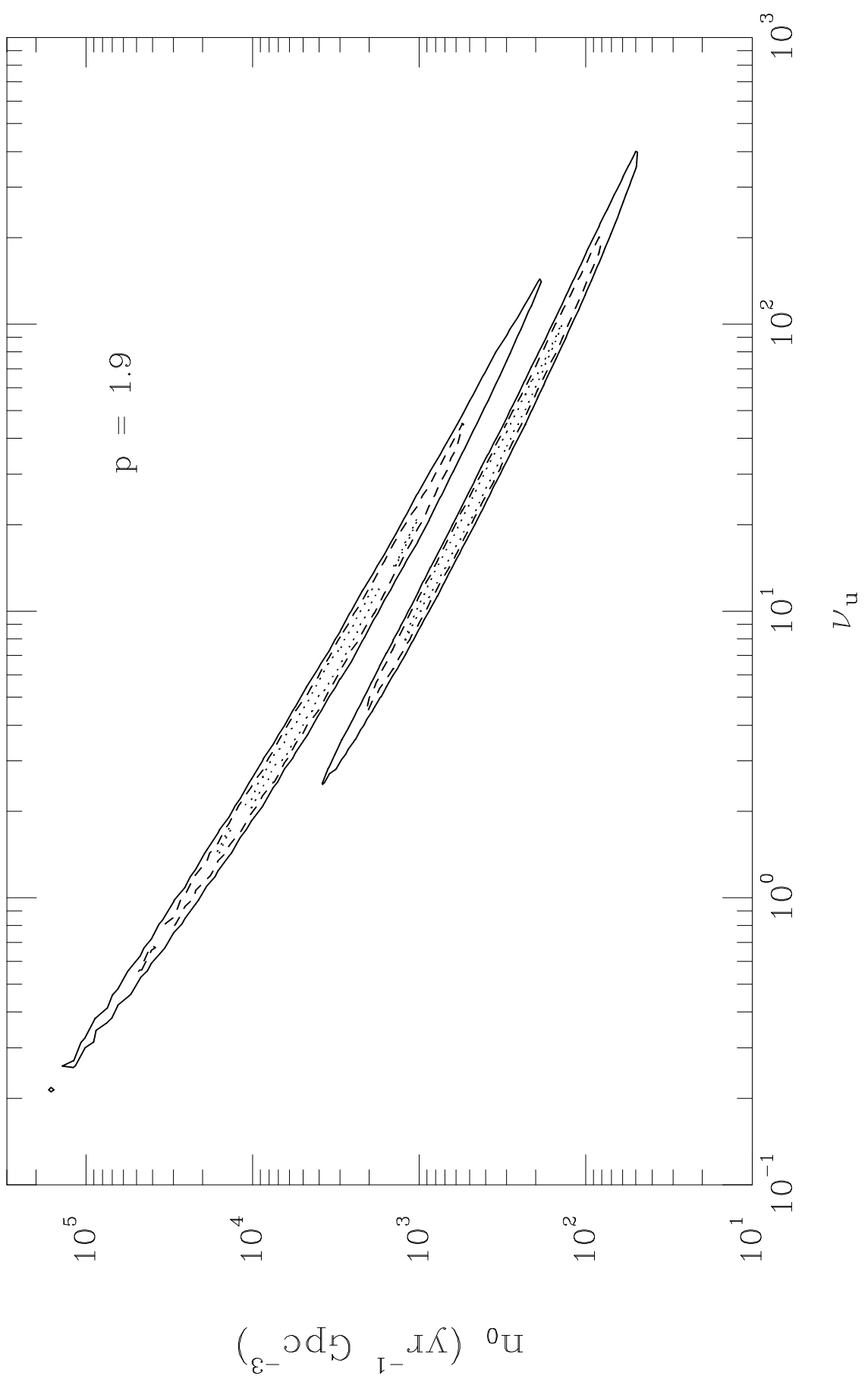
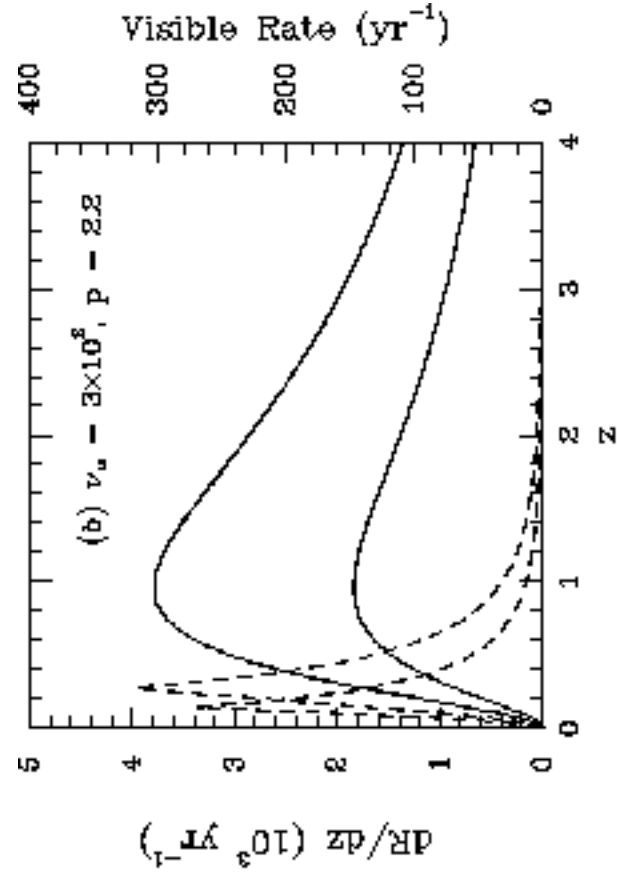


Figure 22



$DR/dz$  ( $10^3 \text{ yr}^{-1}$ )

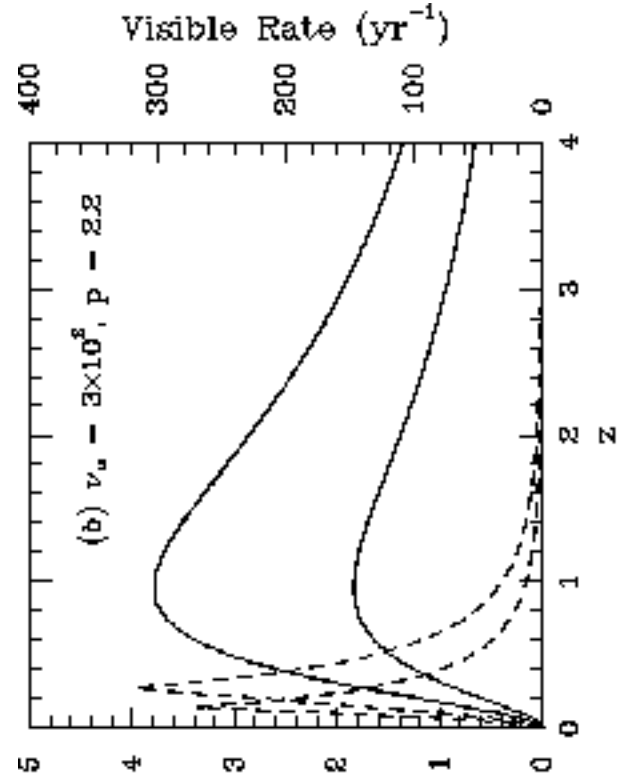


Figure 23

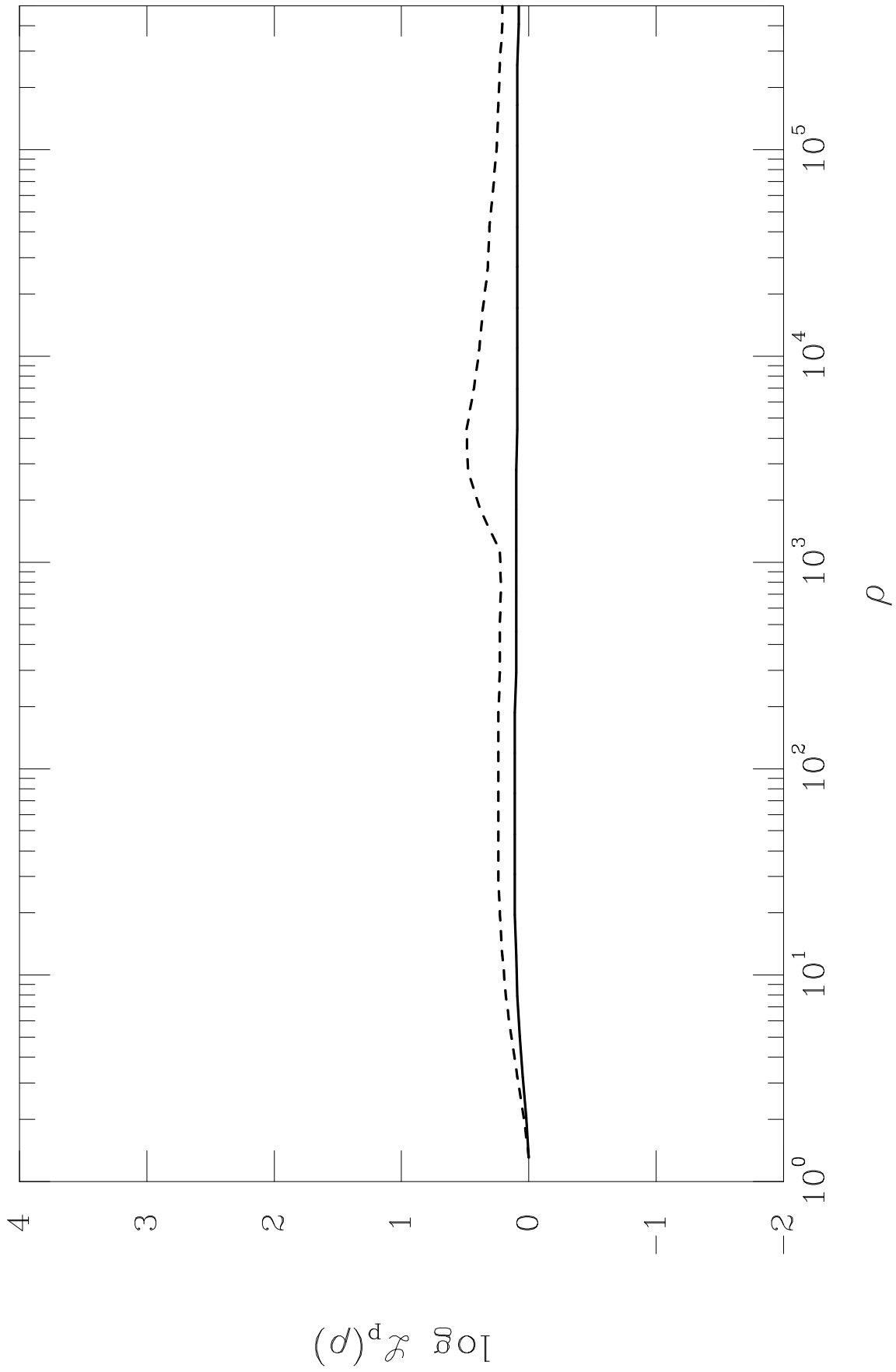


Figure 24

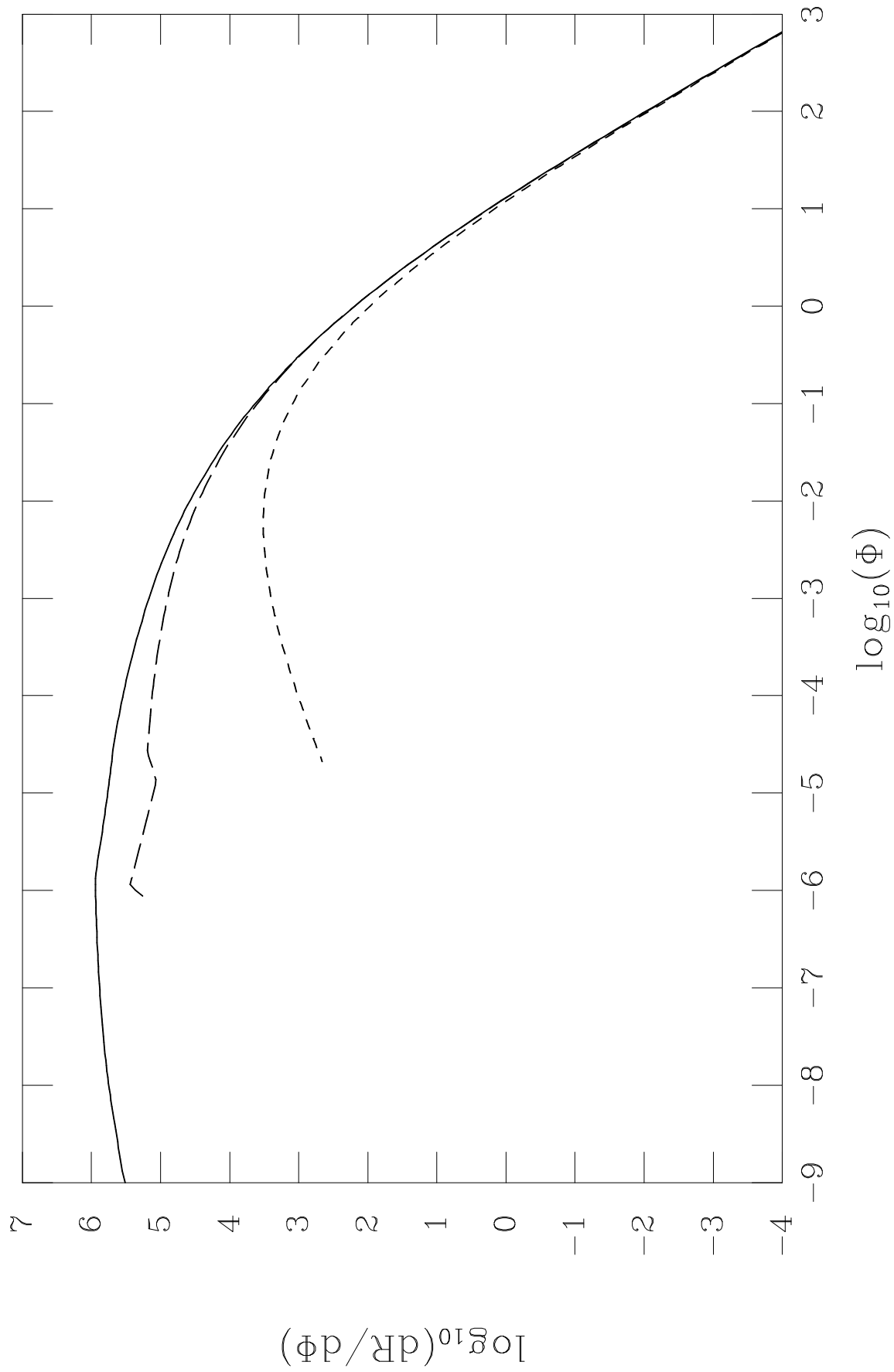


Figure 25

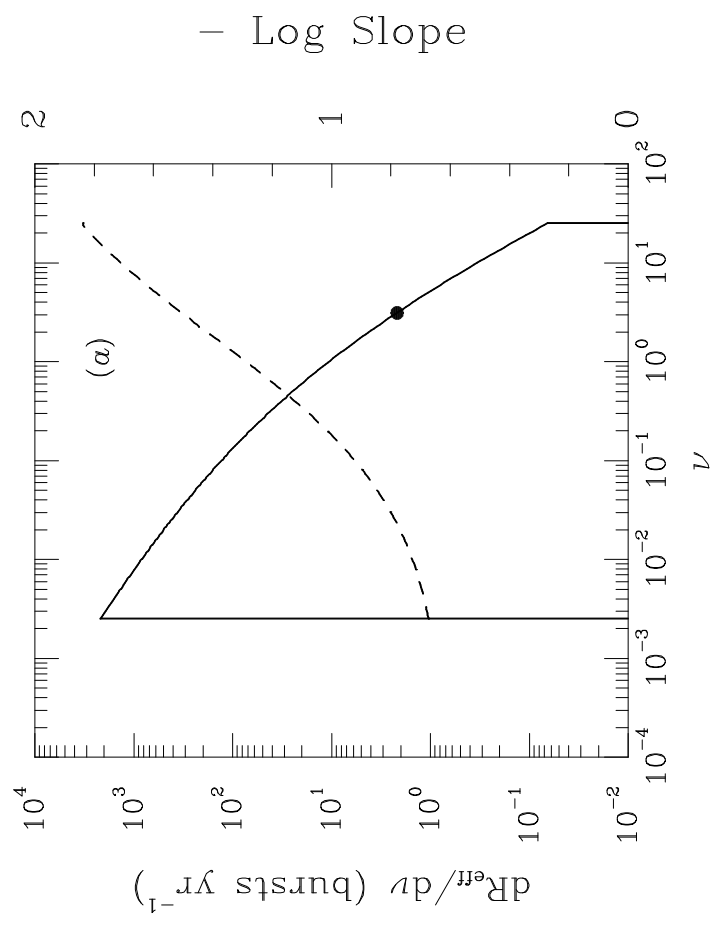
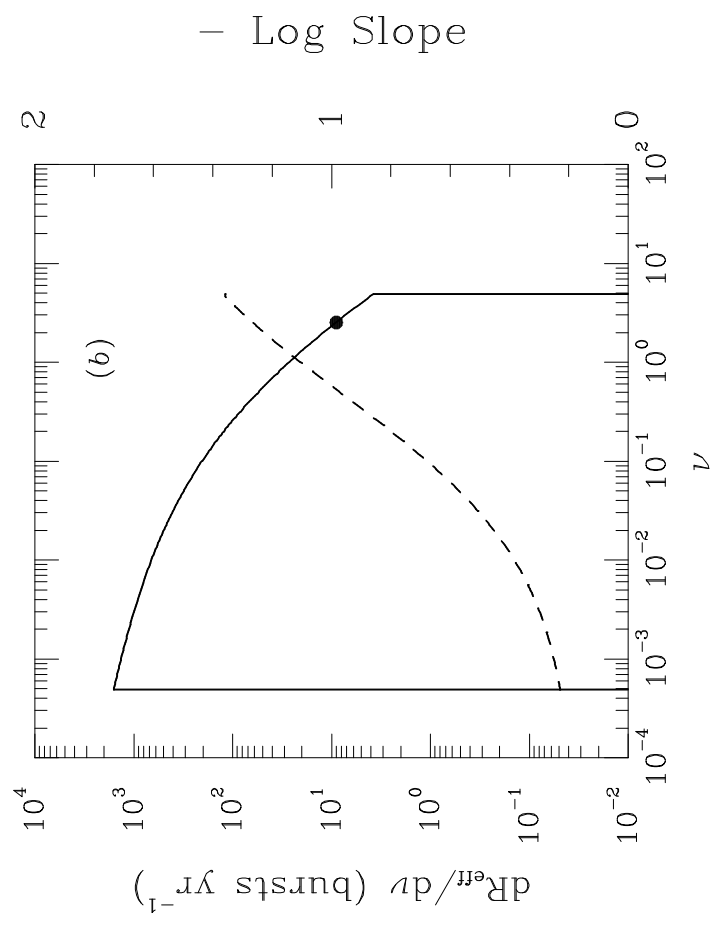


Figure 26

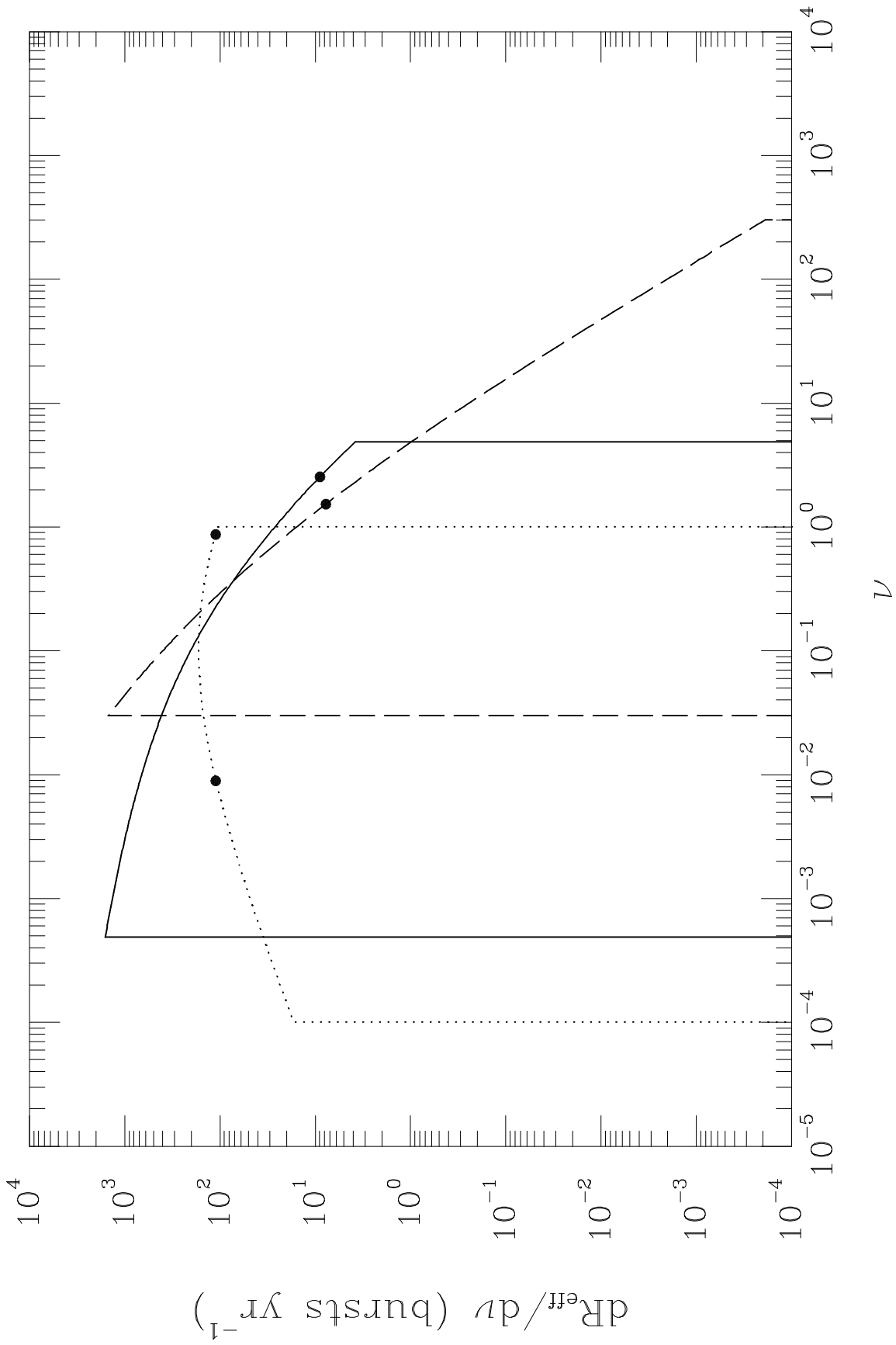


Figure 27

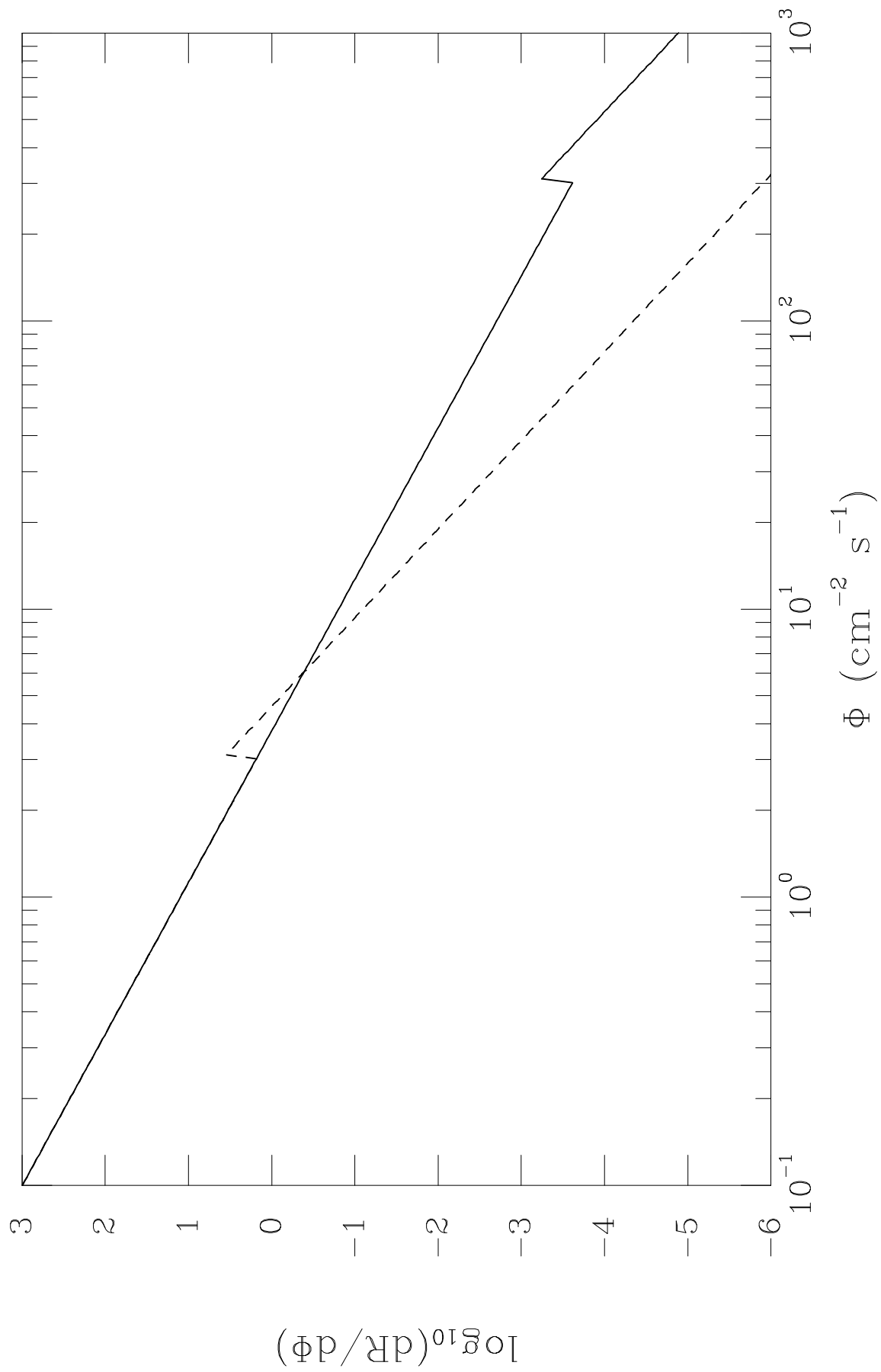


Figure 28

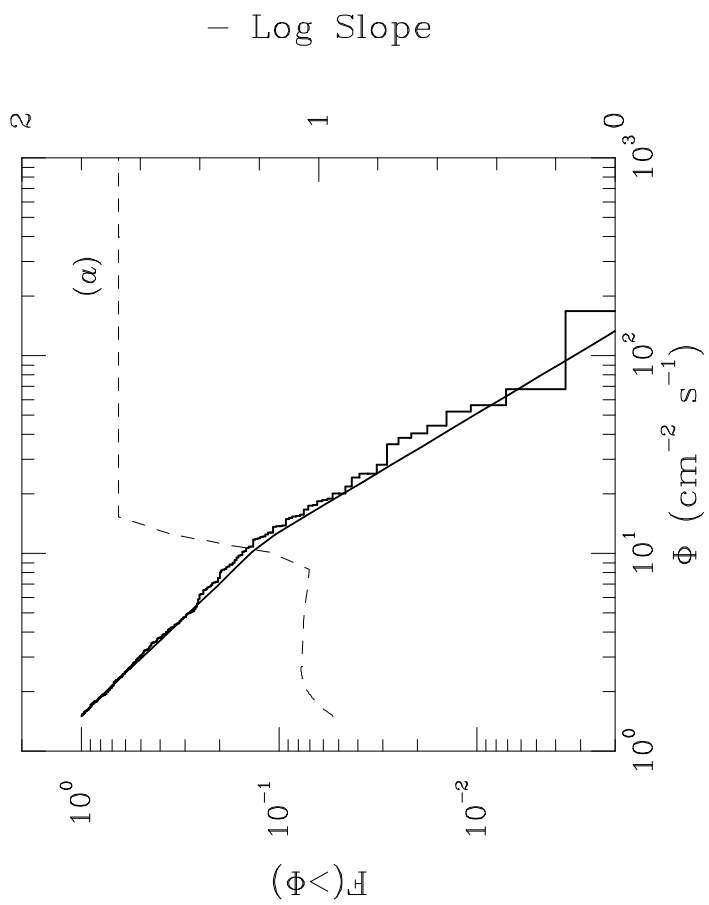
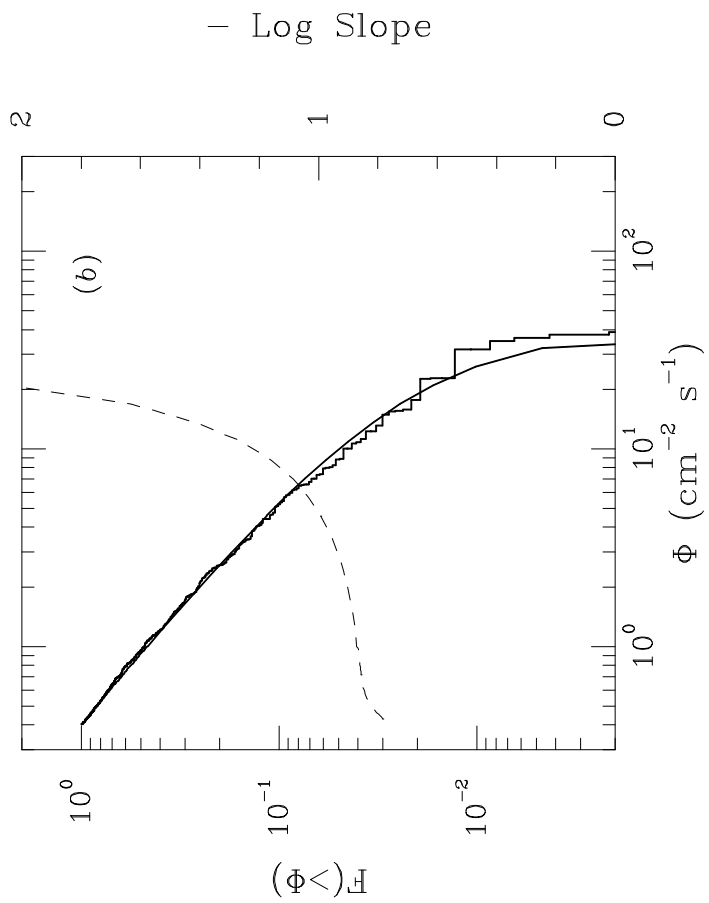


Figure 29

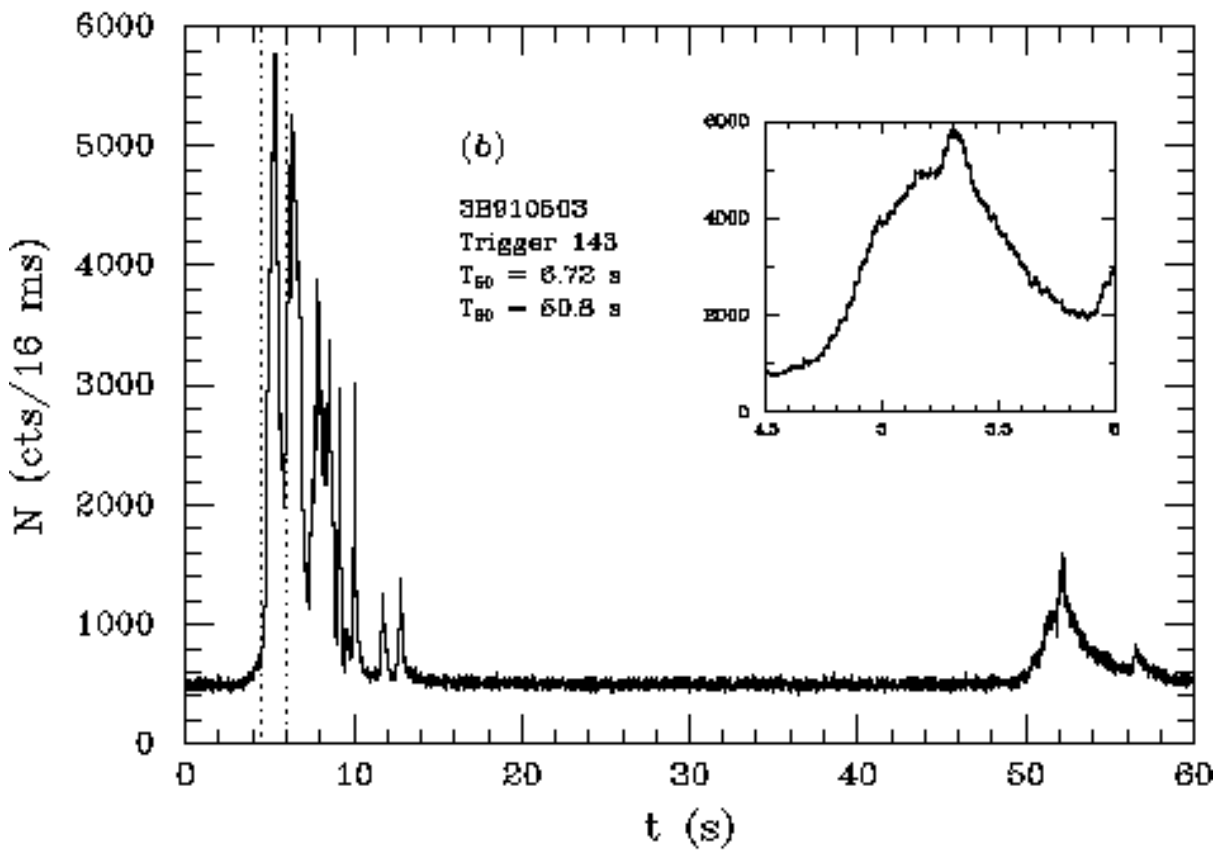
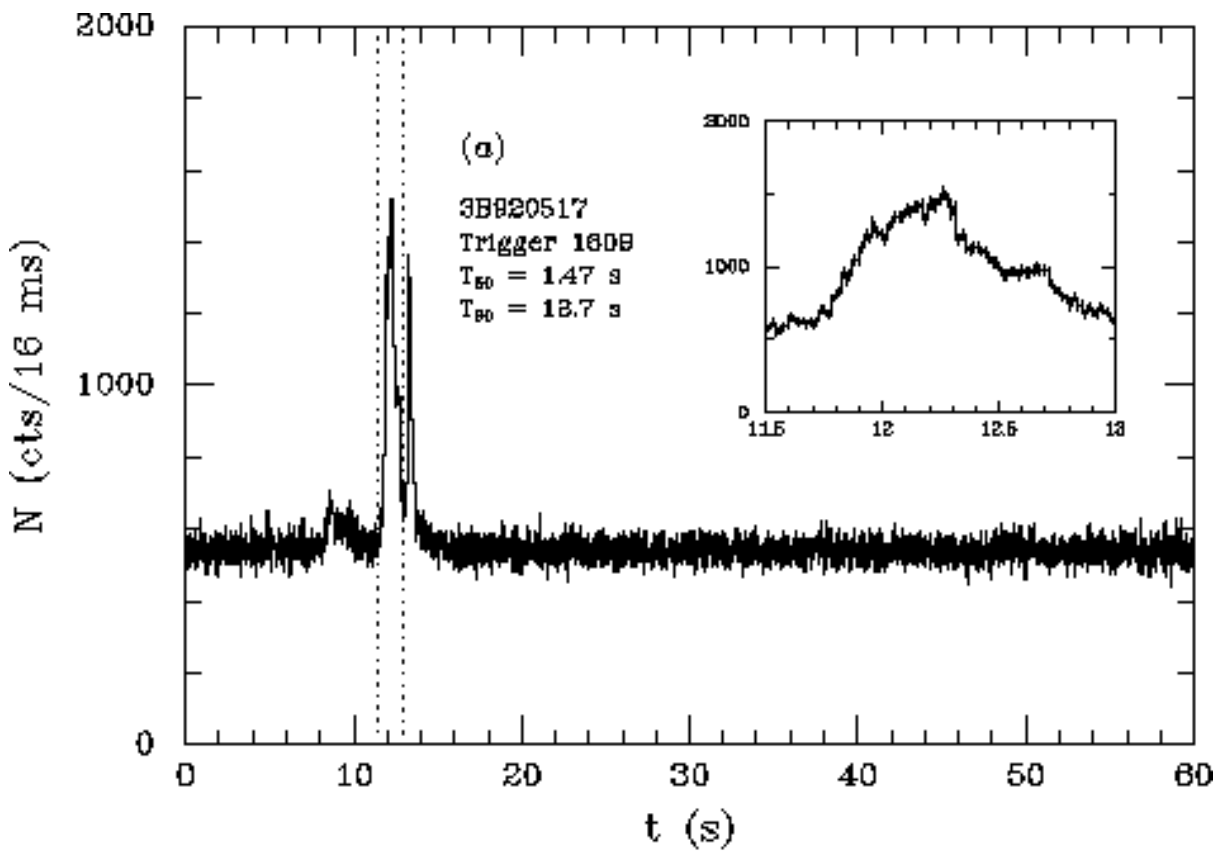


Figure 30 a, b

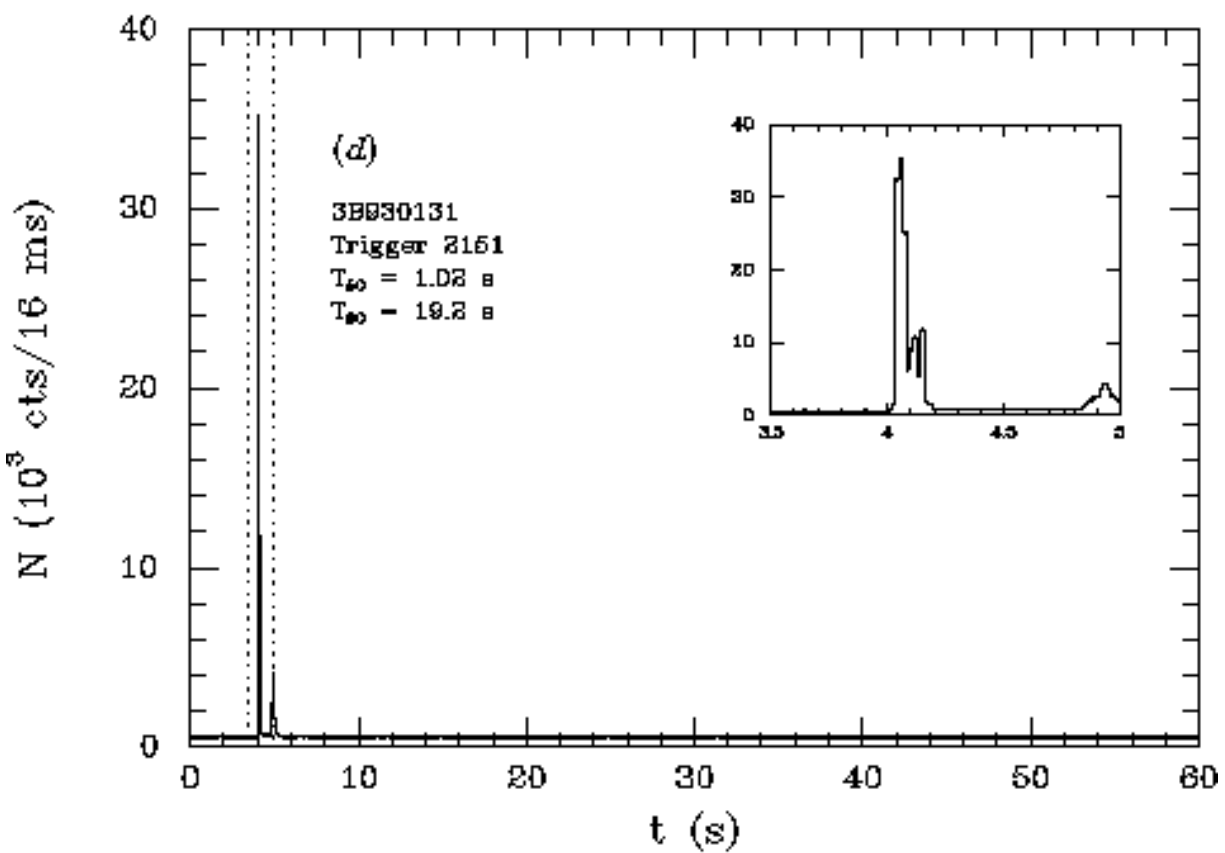
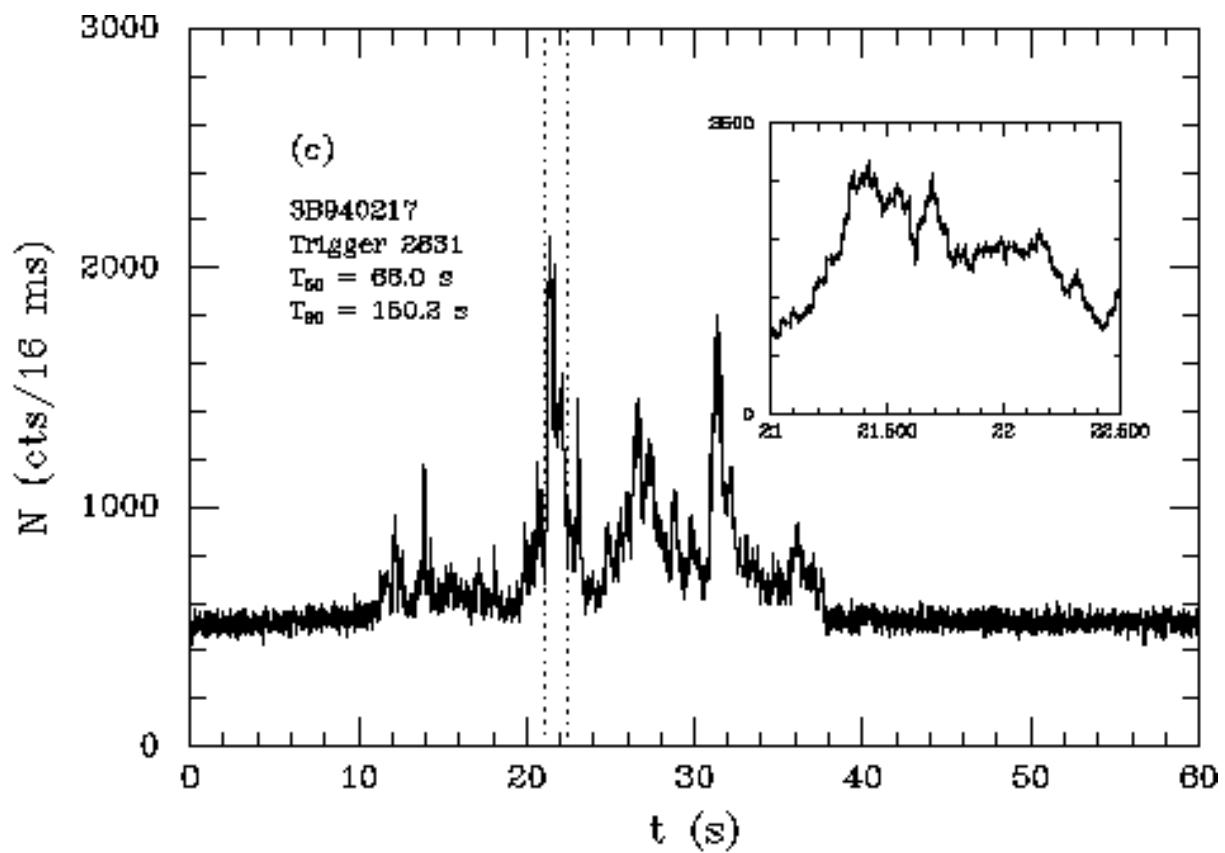


Figure 30 a, d

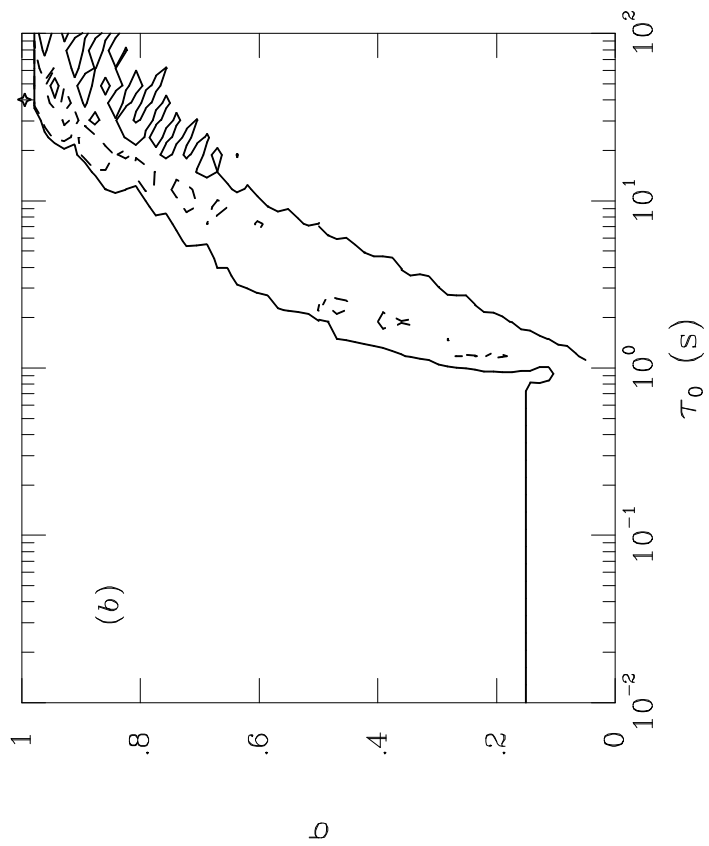
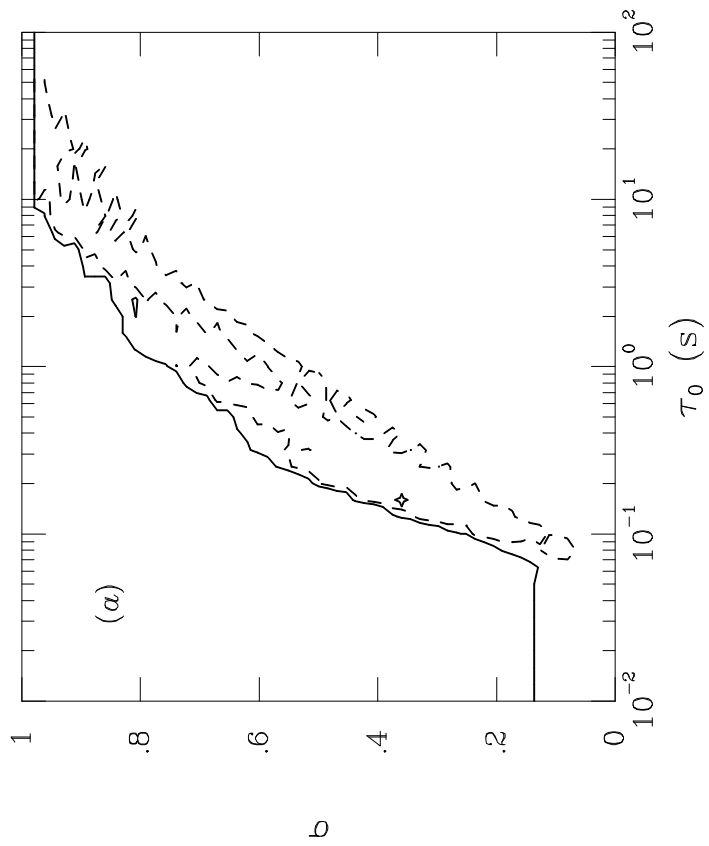


Figure 31

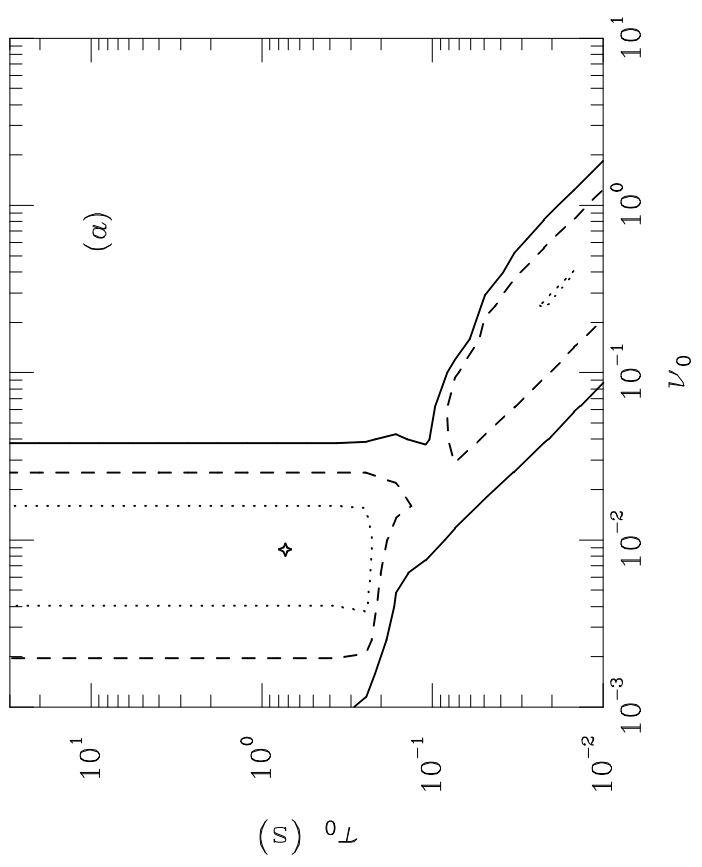
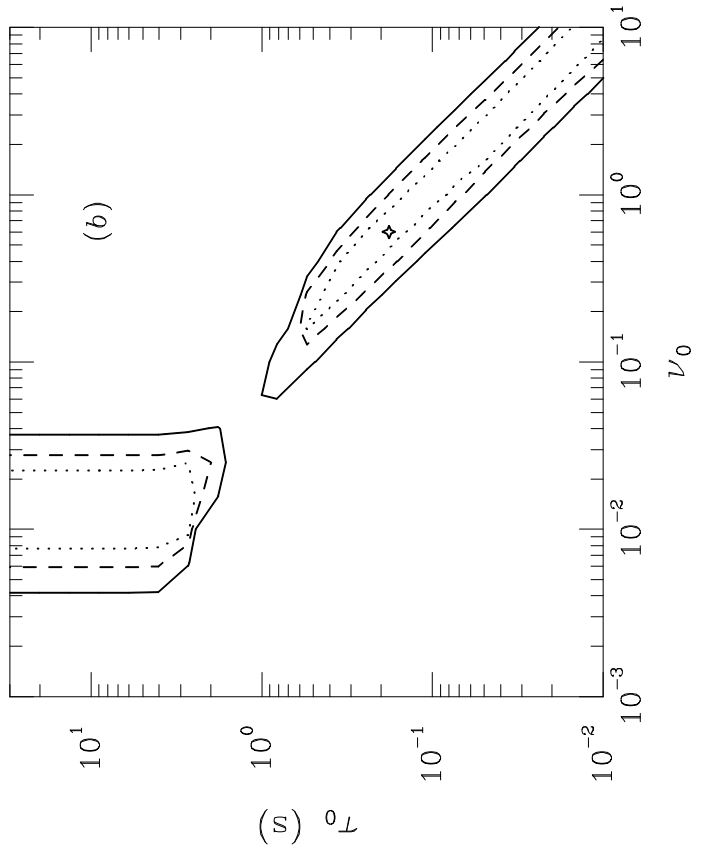


Figure 32

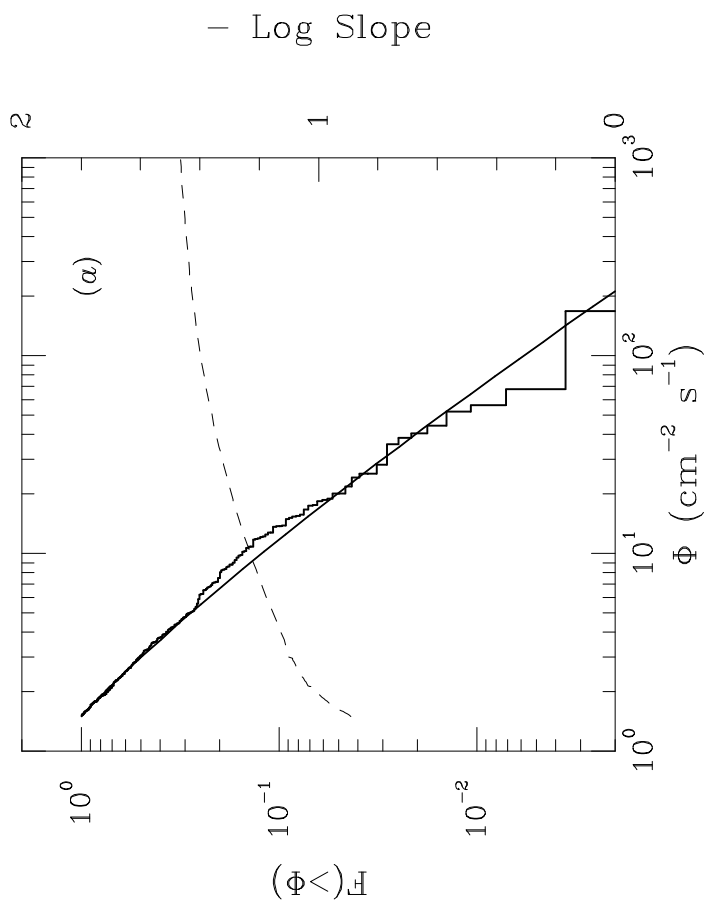
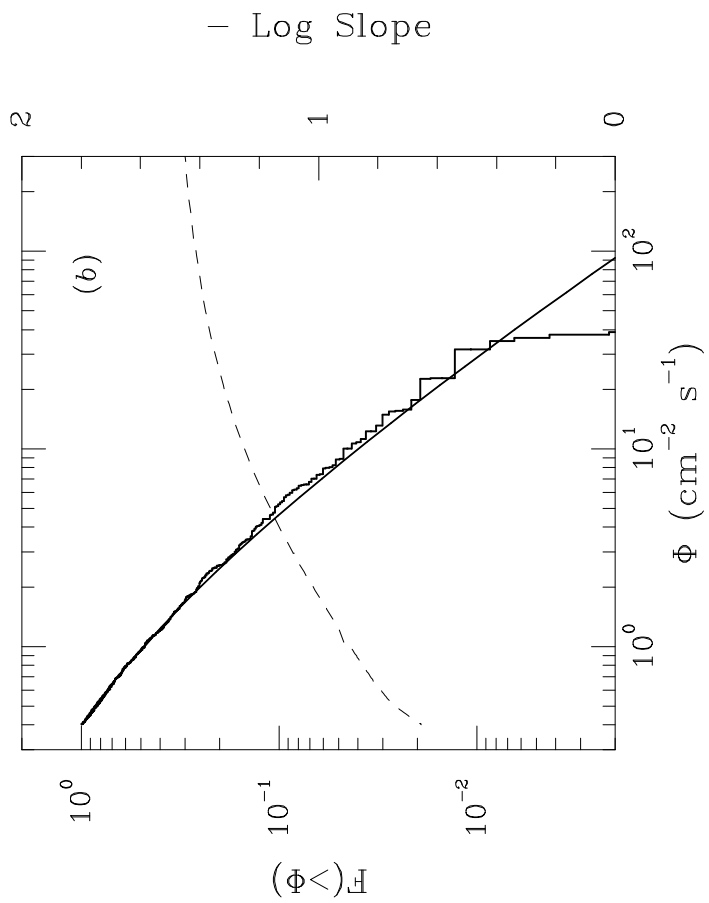


Figure 33